Phonon Hydrodynamics in Fluorides, Alkali Hydrides, and Bilayer Graphene

by

Jamal Abou Haibeh

A thesis submitted in partial fulfillment of the requirements for the master's degree in Applied Sciences in Chemical Engineering

Department of Chemical and Biological Engineering
University of Ottawa

ABSTRACT

Previous experimental studies have reported wave-like transport of heat in a small number of material systems, such as superfluids like helium II [1] and crystal solids like bismuth [2]. This phenomenon was henceforth referred to as ‘second sound’. These rare observations of second sound are partly due to the challenge of obtaining accurate theoretical predictions. In this work, we use an *ab-initio* framework to study phonon hydrodynamics in 3D crystal fluorides and alkali hydrides, including sodium fluoride (NaF), lithium fluoride (LiF), lithium hydride (LiH), and sodium hydride (NaH). Moreover, we predict the existence of phonon hydrodynamics regime in bilayer graphene systems, including AA-bilayer graphene and AB-bilayer graphene.

First, we obtain the second and third-order interatomic force constants using first-principles calculations, which are based on density functional theory (DFT). Secondly, we calculate the lattice thermal conductivity and phonon scattering rates by solving the Boltzmann transport equation (BTE). Thirdly, we apply Guyer’s condition to show the phonon hydrodynamics regime based on the average Normal, Umklapp, and Boundary scattering rates. Finally, we examine the effect of different pseudopotentials on the thermal, electronic, and mechanical properties as well as the phonon hydrodynamics regime. In addition, we report the effect of isotopes on the lattice thermal conductivity and phonon hydrodynamics regime.

Our calculations predict the existence of the second sound in NaF at 15 K and 8.3 mm characteristic length, consistent with previous experimental work [3]. Based on Guyer’s condition, the hydrodynamic window was determined in terms of characteristic lengths ($\sim 10^2 - \sim 10^8$ nm) and temperatures (up to ~80 K) for fluorides and alkali hydrides. On the other hand, second sound in 2D materials has been predicted to exist at much higher temperatures relative to 3D materials. We report the existence of a second sound for AA-bilayer graphene and AB-bilayer graphene above room temperature at a characteristic length of ~100 nm.

SOMMAIRE

Des études expérimentales antérieures ont signalé un transport ondulatoire de la chaleur dans un petit nombre de systèmes matériels, tels que les superfluides comme l'hélium II [1] et les solides cristallins comme le bismuth [2]. Ce phénomène est désormais appelé "second son". Ces rares observations du second son sont en partie dues à la difficulté d'obtenir des prédictions théoriques précises. Dans ce travail, nous utilisons un cadre *ab-initio* pour étudier l'hydrodynamique des phonons dans les fluorures cristallins 3D et les hydrures alcalins, notamment le fluorure de sodium (NaF), le fluorure de lithium (LiF), l'hydrure de lithium (LiH) et l'hydrure de sodium (NaH). De plus, nous prédisons l'existence d'un régime d'hydrodynamique des phonons dans les systèmes de graphène bicouche, y compris le graphène bicouche AA et le graphène bicouche AB.

Tout d'abord, nous obtenons les constantes de force interatomique de deuxième et troisième ordre à l'aide de calculs de premiers principes, basés sur la théorie fonctionnelle de la densité (DFT). Deuxièmement, nous calculons la conductivité thermique du réseau et les taux de diffusion des phonons en résolvant l'équation de transport de Boltzmann (BTE). Troisièmement, nous appliquons la condition de Guyer pour montrer le régime hydrodynamique des phonons basé sur les taux de diffusion normaux, Umklapp et limites moyens. Enfin, nous examinons l'effet de différents pseudopotentiels sur les propriétés thermiques, électroniques et mécaniques ainsi que sur le régime hydrodynamique des phonons. En outre, nous rapportons l'effet des isotopes sur la conductivité thermique du réseau et le régime d'hydrodynamique des phonons.

Nos calculs prédisent l'existence du second son dans le NaF à 15 K et à une longueur caractéristique de 8.3 mm, ce qui est conforme aux travaux expérimentaux précédents [3]. Sur la base de la condition de Guyer, la fenêtre hydrodynamique a été déterminée en termes de longueurs caractéristiques ($\sim10^2 - \sim10^8$ nm) et de températures (jusqu'à ~80 K) pour les fluorures et les hydrures alcalins. D'autre part, on a prédit que le second son dans les matériaux 2D existe à des températures beaucoup plus élevées que dans les matériaux 3D. Nous rapportons l'existence d'un second son pour le graphène bicouche AA et le graphène bicouche AB au-dessus de la température ambiante à une longueur caractéristique de ~100 nm.

STATEMENT OF CONTRIBUTIONS OF COLLABORATORS

I hereby declare that the work presented in this thesis is entirely my own effort, and I am the sole author of this thesis. All chapters and appendices were solely written by me with editorial suggestions and scientific reviews given by Dr. Samuel Huberman. The Python code (see Appendix A-5) was written by me with the guidance of Dr. Samuel Huberman.

TABLE OF CONTENTS

LIST OF FIGURES

LIST OF TABLES

NOMENCLATURE

a	Lattice constant
a_1, a_2, a_3	Spring constants (a_1: harmonic spring constant; a_2 and a_3: anharmonic spring constants)
A	Wave amplitude
B	Bulk modulus
c_v	Specific heat at constant volume
c_p	Specific heat at constant pressure
C	Heat capacity
C	Elastic constant
e	Strain component
E	Energy
E_f	Fermi energy
E_g	Bandgap
E_k	Kinetic energy
g(ω)	Phonon density of states function
G	Reciprocal lattice vector
G	Shear modulus
$\hbar$	Modified Planck's constant, 1.05457×10^{-34} J.s
H	Hamiltonian
i	Imaginary number
k	Thermal conductivity
k_B	Boltzmann's constant, 1.38065×10^{-23} J/K

k_L	Lattice thermal conductivity
K	Spring constant (Hooke’s law)
L	Characteristic length
m	Mass
n	Number of atoms in a unit cell
N	Total number of unit cells
p	Momentum
P	Pressure
q	Heat flux
r	Position
t	Time
T	Temperature
u	Displacement position
v_g	Phonon group velocity
V	Interatomic potential energy
V	Volume
V^*	Unit cell volume
x	Position
W	Rate transition
Z^*	Born effective charge
$\langle\ \rangle$	Average

Greek Symbols

α, β	Nonlinear force coefficients
α	Thermal expansion coefficient
δ	Dirac-function
Δ	Difference
ε	Strain
$\bar{\gamma}$	Average Grüneisen parameter
Θ	Debye temperature
κ	Phonon wavevector
Λ	Mean free path
π	Pi constant, 3.14159
ρ	Density
$\rho(r)$	Electron density
σ	Stress
τ	Lifetime
Φ	Interatomic force constant
ψ	Wave function
Ψ	Quantum state
ω	Phonon frequency

Abbreviations

BPSR	Boundary Phonon Scattering Rate
BTE	Boltzmann Transport Equation
DFT	Density Functional Theory
IPSR	Isotope Phonon Scattering Rate
LDA	Local Density Approximation
NPSR	Normal Phonon Scattering Rate
PBE	Perdew-Burke-Ernzerhof
PBESOL	Perdew-Burke-Ernzerhof for Solids
PDOS	Phonon Density of States
RTA	Relaxation Time Approximation
UPSR	Umklapp Phonon Scattering Rate

ACKNOWLEDGEMENTS

I would like to thank my supervisors, Dr. Samuel Huberman and Dr. Andrew Sowinski, for all their assistance, support, and dedicated involvement in each step over these past two years. I consider myself fortunate to have you as my supervisors. Also, I would like to thank my family for their endless support and encouragement.

DEDICATION

I dedicate this thesis to my parents. Without you, I might not be the person I am today.

CHAPTER 1

INTRODUCTION

1.1 Overview

It is known that heat transfer is the movement of thermal energy resulting from a temperature difference (gradient). Heat can transfer through three mechanisms: conduction, convection, and radiation [4]. Conduction is caused by interactions between particles, which results in the transfer of energy from higher energetic particles to less energetic particles. Convection happens because of the molecular movement of fluids. Radiation is the thermal energy transmitted by electromagnetic waves. In solids, heat conduction is the dominant of these mechanisms. Joseph Fourier (1768-1830) proposed a mathematical relationship between the heat flux and temperature gradient, known as Fourier's law of conduction [5]. This relationship originates back to Newton's law of cooling in 1701 [6].

From a microscopic point of view, however, heat conduction occurs when particles in a system move randomly, transferring thermal energy from one place to another. The simplest example of microscopic heat conduction is the random collision among gaseous molecules, where the average distance traveled between the molecular collisions is referred to as the mean free path ‘Λ’ [7]. In fact, there must be a heat carrier for heat transfer to occur. Various heat carriers contribute to heat transfer processes, including molecules, electrons, photons, and phonons [8].

Besides real particles, quasiparticles can also be viewed as carriers of heat. Phonons are quanta of lattice vibrational energy that can behave like waves and particles [9]. From the perspective of quantum mechanics, phonons are wave packets [10]. While molecules, electrons, and photons can propagate in a vacuum or media (e.g., solids), phonons can propagate in media only. Phonons, like photons have an energy of $\hbar\omega$, but their positions are not localized. Instead, a wave packet can be constructed of phonon modes with varied frequencies and wavelengths to effectively represent a particle. Statistically, phonons, photons, and molecules can be treated using Bose-Einstein statistics and so-called bosons (includes integral spins), while electrons follow Fermi-Dirac statics and so-called fermions (includes half-integral spins) [8].

Following the proposal of Fourier's law, the diffusive limit has traditionally been used to describe the transport of phonons. However, heat transfer at micro and nanoscales is expected to deviate from Fourier's law due to the comparable characteristic dimension (scale of a physical system) of the structures with the mean free path of energy carriers in phonons. As shown in Figure 1.1, there are at least three types of phonon transport regimes: ballistic, hydrodynamic, and diffusive.

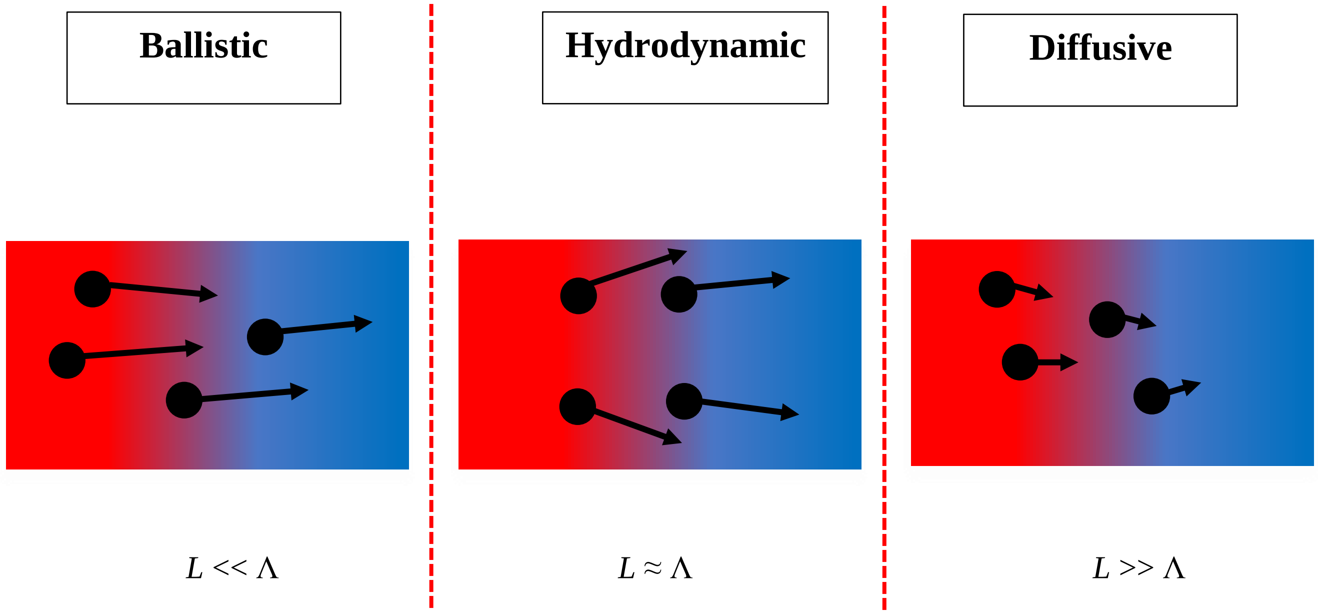

Figure 1.1: Phonon transport regimes.

The diffusive regime is shown when the characteristic length of the sample is longer than the mean free path, whereas the ballistic regime can be observed at low temperatures, where the characteristic length of the sample is shorter than the mean free path. In this thesis, we will focus on the hydrodynamics regime, which occurs between the ballistic and diffusive regimes. The evolution of the flow and population of phonons in this regime is collective. Previous analytical and experimental studies have examined the hydrodynamics phonon transport in different materials [11]–[15]. By solving the BTE, one can effectively determine the regime of phonon transport [16]. This thesis sets out the answer the following questions: How BTE was derived? How BTE can be solved? What computational methods can be employed to examine phonon hydrodynamics in materials?

1.2 Organization of Thesis

This thesis aims to provide accurate predictions of phonon hydrodynamics for various materials using first-principles calculations. The organization of the thesis, as shown in Figure 1.2, is as follows

Chapter 2:

It consists of two main sections:

1) Theory: we present some theoretical foundations on which this work is based. Boltzmann transport equation (BTE) and its solution are discussed.
2) Computational methods: connections between different *ab-initio* computational methods are presented to introduce the calculations of phonon hydrodynamics.

Chapter 3:

This chapter shows phonon hydrodynamics windows and numerous results for the properties of three different material systems (Fluorides, Alkali Hydrides, and Bilayer Graphene). The properties include:

1) Mechanical properties: bulk modulus and elastic constants.
2) Thermal properties: thermal conductivity, heat capacity, and Grüneisen parameter.
3) Electronic properties: band structure, band gap, and dispersion relation.

The second section of this chapter discusses the results.

Chapter 4:

This chapter summarizes the conclusions and future work.

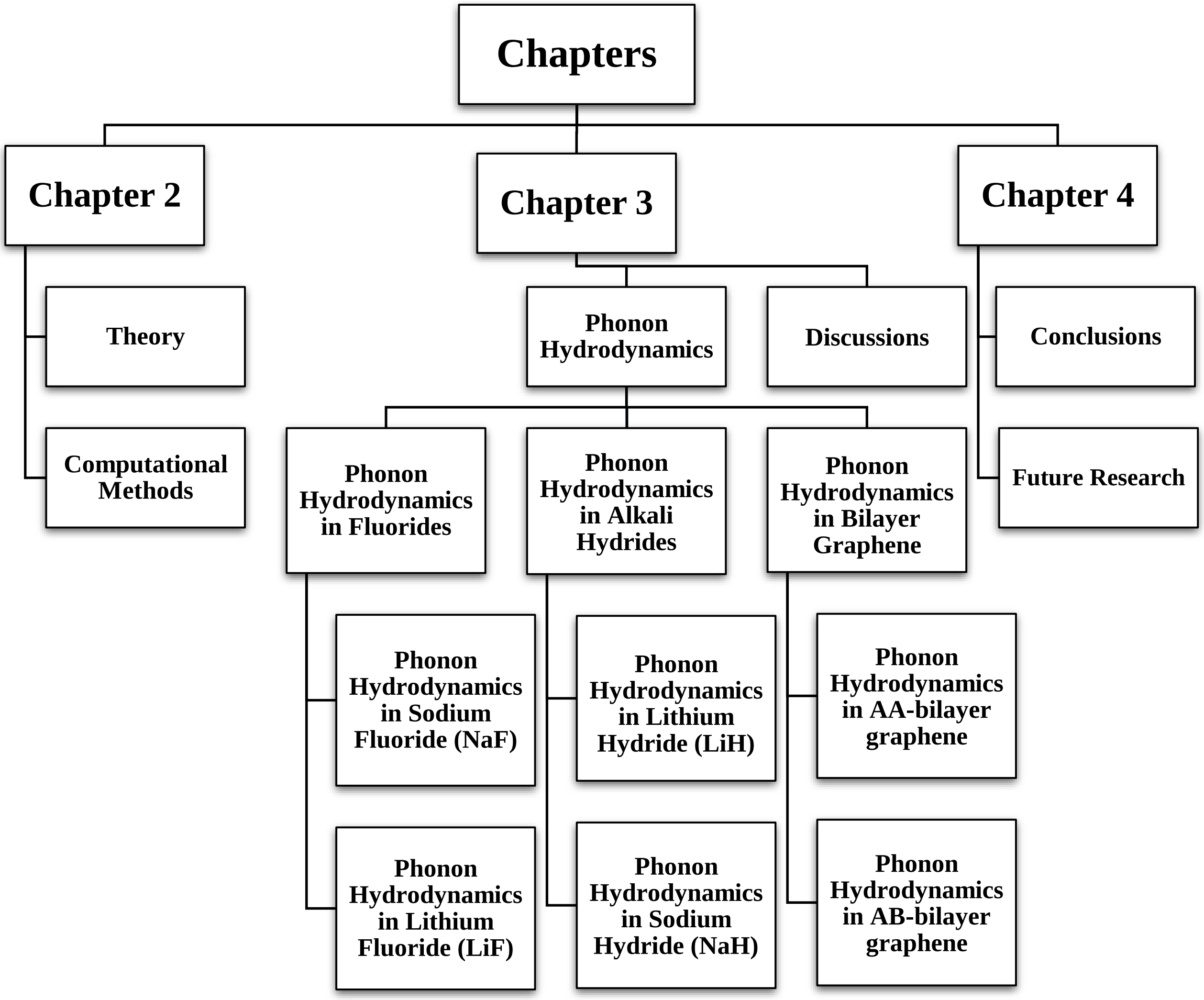

Figure 1.2: Thesis Structure.

CHAPTER 2

THEORETICAL AND COMPUTATIONAL METHODS

2.1 Theory

In this section, the theory of phonons is reviewed. First, two examples of one-dimensional chains are presented to introduce important general concepts that will be used throughout this work. Anharmonic effects are essential for capturing phonon interactions, and the Boltzmann transport equation (BTE) are presented. The connection between the properties of phonons and macroscopic physical properties is established. Finally, the theory of phonon hydrodynamics is discussed.

2.1.1 Harmonic Lattice Vibrations

The history of lattice dynamics started in 1908 when Jean Perrin - a physical chemist- confirmed the existence of real atoms by studying the Brownian motion as described by Einstein [17]. Later in 1912, the model of lattice dynamics was developed by Born and von Kàrmàn, who introduced a model to describe the atomic movements in a crystal lattice [18]. In this model, it was assumed that the equations of motions of the atoms follow Hooke's force law. The first crystal structure examined on the basis of Born-von Kàrmàn model was the diamond [19]. We start with a linear chain of atoms to describe lattice dynamics in the harmonic approximation.

2.1.1.1 One-dimensional Monatomic Chain

Consider an infinite 1D chain of identical atoms (equal masses ‘*m*’) separated by a distance of ‘*a*’, as shown in Figure 2.1, and assume the interaction force between atoms follows Hooke’s law with a spring constant ‘*K*’. Also, for simplicity, only the nearest neighbor’s interaction is considered in this case. The displacement of atom ‘*n*’ is

$$u_n = x_f - x^o \tag{2.1}$$

where x_f is the displaced position and x^o is the equilibrium position

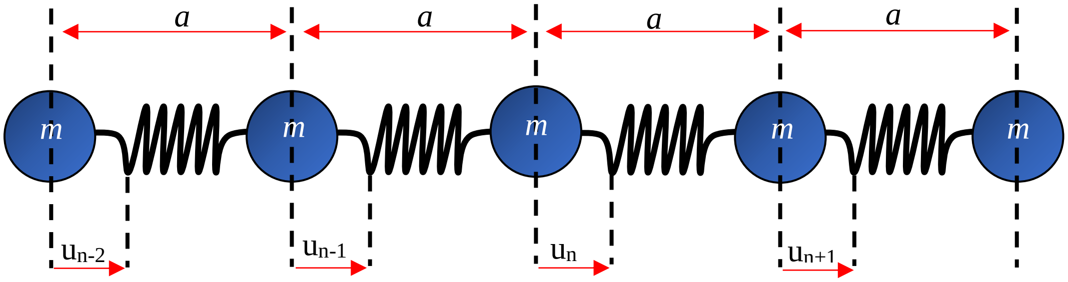

Figure 2.1: 1D linear monoatomic chain.

Applying Newton’s second law of motion on the n^{th} atom

$$m\frac{\partial^2 u_n}{\partial t^2} = K(u_{n+1} - u_n) - K(u_n - u_{n-1}) \tag{2.2}$$

$$m\frac{\partial^2 u_n}{\partial t^2} = K(u_{n+1} - 2u_n + u_{n-1}) \tag{2.3}$$

The displacement of the n^{th} atom follows a plane wave form

$$u_n = \mathrm{A}e^{i(\kappa na - \omega t)} \tag{2.4}$$

where A is the wave amplitude, κ is the wave number (wavevector), *na* is the discrete equilibrium position of atom ‘n’, and ω is the vibrational frequency. Plugging in Eq. (2.4) into Eq. (2.2), Eq. (2.3) becomes

$$-m\omega^2 \mathrm{A}e^{i(\kappa na-\omega t)} = K(\mathrm{A}e^{i(\kappa(n+1)a-\omega t)} - 2\mathrm{A}e^{i(\kappa na-\omega t)} + \mathrm{A}e^{i(\kappa(n-1)a-\omega t)}) \tag{2.5}$$

$$-m\omega^2 = K(\mathrm{A}e^{i\kappa a} - 2 + \mathrm{A}e^{-i\kappa a}) \tag{2.6}$$

Solving for ω

$$\omega = 2\sqrt{\frac{K}{m}}\left|\sin\frac{\kappa a}{2}\right| \tag{2.7}$$

The maximum frequency in the range of (-π/*a* < κ < π/*a*) is

$$\omega_{\max} = 2\sqrt{\frac{K}{m}} \tag{2.8}$$

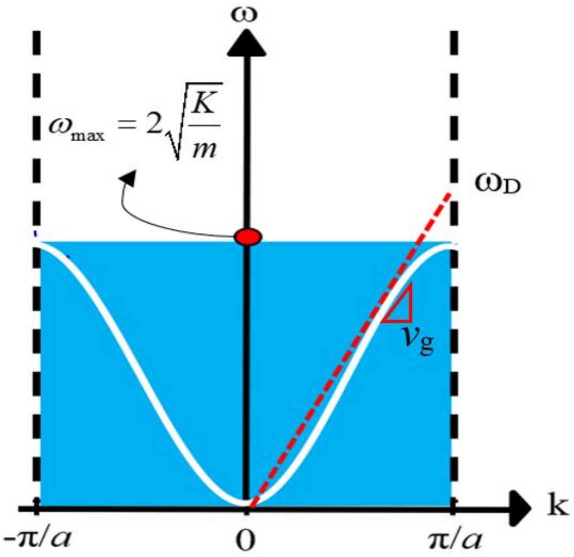

Figure 2.2: Phonon dispersion curve of 1D identical masses chain in the first Brillouin zone. The red dashed line represents a linear relationship between frequency and wavevector.

Figure 2.2 shows a nonlinear relationship between frequency and wavevector, called the ‘dispersion relation’. Each wavevector corresponds to a mode as described by Eq. (2.4). Several quantities can be obtained from the dispersion relation. One such example is the group velocity, which is determined by the slope of the dispersion curve

$$v_g = \frac{\partial \omega}{\partial \kappa} \tag{2.9}$$

2.1.1.2 One-dimensional Diatomic Chain

Novel properties are exhibited when two different atom types are present, as in an ionic crystal like NaCl. As shown in Figure 2.3, two various types of atom masses ‘m_1’ and ‘m_2’ are connected by identical springs in a one-dimensional chain with a spring constant of ‘K’ and a constant distance of ‘$a/2$’ between atoms.

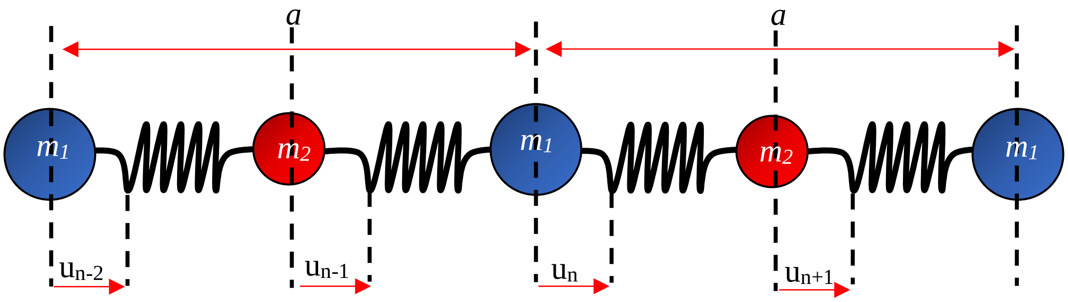

Figure 2.3: 1D linear diatomic chain.

Following the same approach as in Section (2.1.1.1), the application of Newton’s second law of motion on atoms m_1, n^{th} and m_2, $(n\text{-}1)^{th}$ yields

$$m_1 \frac{\partial^2 u_n}{\partial t^2} = K(u_{n+1} - u_n) - K(u_n - u_{n-1}) = K(u_{n+1} - 2u_n + u_{n-1}) \tag{2.10}$$

$$m_2 \frac{\partial^2 u_{n-1}}{\partial t^2} = K(u_n - u_{n-1}) - K(u_{n-1} - u_{n-2}) = K(u_n - 2u_{n-1} + u_{n-2}) \tag{2.11}$$

Eq. (2.10) and Eq. (2.11) can be converted to the determinantal equation as

$$\begin{vmatrix} 2K - m_1\omega^2 & -K(1+e^{-i\kappa a}) \\ -K(1+e^{i\kappa a}) & 2K - m_2\omega^2 \end{vmatrix} = 0 \tag{2.12}$$

The solution of Eq. (2.12) contains two roots

$$\omega_{\pm}^2 = K\left(\frac{1}{m_1}+\frac{1}{m_2}\right) \pm K\sqrt{\left[\left(\frac{1}{m_1}+\frac{1}{m_2}\right)^2 - \frac{4\sin^2(na/2)}{m_1 m_2}\right]} \tag{2.13}$$

Eq. (2.13) can be reduced if $n = \pm \pi/a$

$$\omega_{\pm}^2 = K\left(\frac{1}{m_1}+\frac{1}{m_2}\right) \pm K\left(\frac{1}{m_2}-\frac{1}{m_1}\right) \tag{2.14}$$

The positive sign is called the *optical mode*

$$\omega_{+} = \sqrt{\frac{2K}{m_2}} \tag{2.15}$$

The negative sign is called the *acoustic mode*

$$\omega_{-} = \sqrt{\frac{2K}{m_1}} \tag{2.16}$$

2.1.1.3 Real Crystals

To connect the previous discussion to real crystals, the introduction of crystallographic terminology is necessary. Any crystal structure consists of a *lattice* (regular points in space) and a *basis* (group of atoms arranged in space) [20]. A vector connecting any two lattice points is known as a *lattice vector*. Crystals are ordered structures, where the repeating atoms arrangement of crystals is referred to as *unit cells*. The simplest unit cell is the primitive cell with one atom per unit, as illustrated in Figure 2.4 (a). There are other unit cell structures, such as face-centered and body-centered unit cells. Figure 2.4 (b) shows the unit cell of crystal silicon, which is visualized as two piercing face-centered cubic lattices (FCC). The structure of FCC is a cube having an atom on the center of each face, as well as on each of its four corners. The lines connecting the silicon atoms represent nearest-neighbor bonds (blue line), where the edge length (black line) is called the *lattice constant*. The calculated lattice constant of silicon is 5.43 Å, as confirmed in the experiment [21].

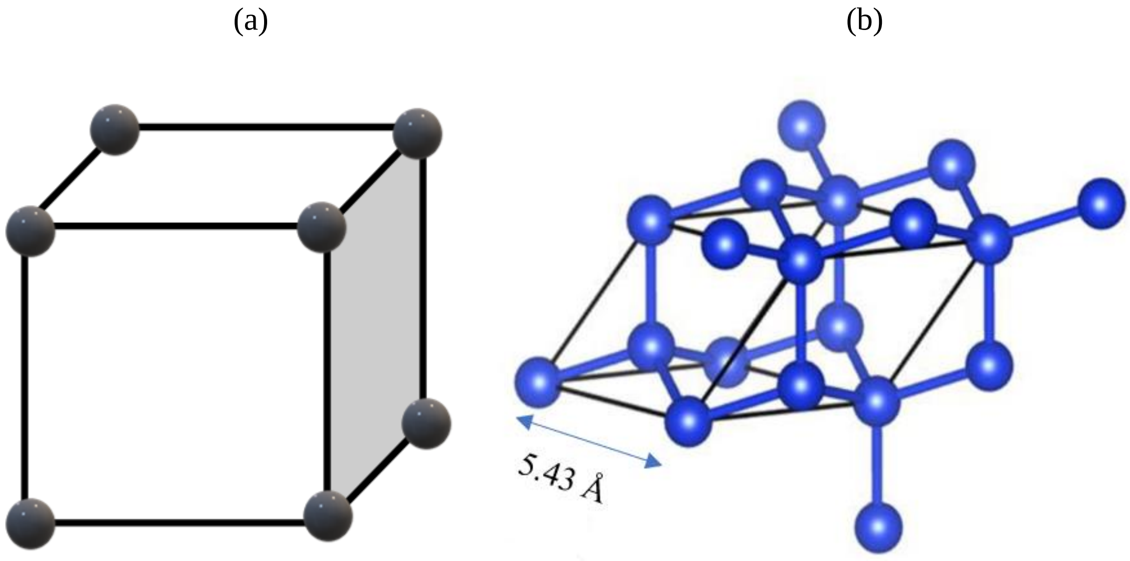

Figure 2.4: (a) Primitive crystal. (b) The unit cell of silicon.

For a real crystal, the dispersion relations can be obtained following a procedure analogous to the previously presented one-dimensional problems. Acoustic modes signify the movement of mechanical waves 'sound waves' through an elastic medium (in-phase), whereas optical modes indicate the movement of atoms that are out-of-phase. Atoms may vibrate longitudinally in the direction of wave propagation and transversely 'perpendicular' to the direction of waves. In the three-dimensional lattice with N atoms per unit cell, there are $3N$ phonon branches: 3 acoustic and $3N$-3 optical modes [20]. Recall for a monoatomic chain, there are 3 branches (acoustical branches only). On the other hand, there are 6 branches for three-dimensional diatomic lattice: 3 acoustical branches (1 longitudinal acoustical 'LA' and 2 transverse acoustical 'TA' modes) and 3 optical branches (1 longitudinal optical 'LO' and 2 transverse optical 'TO' modes). Figure 2.5 (a) illustrates an example of calculated phonon dispersion for crystal silicon (the relation between momentum and energy). As the wavevector approaches zero (i.e., $\kappa \rightarrow 0$), the energy of acoustic modes vanishes (no gaps). The path of the dispersion curve ($\Gamma \rightarrow X \rightarrow K \rightarrow \Gamma \rightarrow L$) is restricted by the *first Brillouin zone*, which is the nearest reciprocal lattice region to the original node (i.e., κ_x, κ_y,

κ_z = 0,0,0) [22]. While real space contains points that can be single atoms or unit cells, reciprocal space contains points that represent a particular set of lattice planes. A similar concept to this region in real space is called the *Wigner-Seitz* cell [22]. Figure 2.5 (b) shows the first Brillouin zone of the FCC lattice, which is followed by silicon as well.

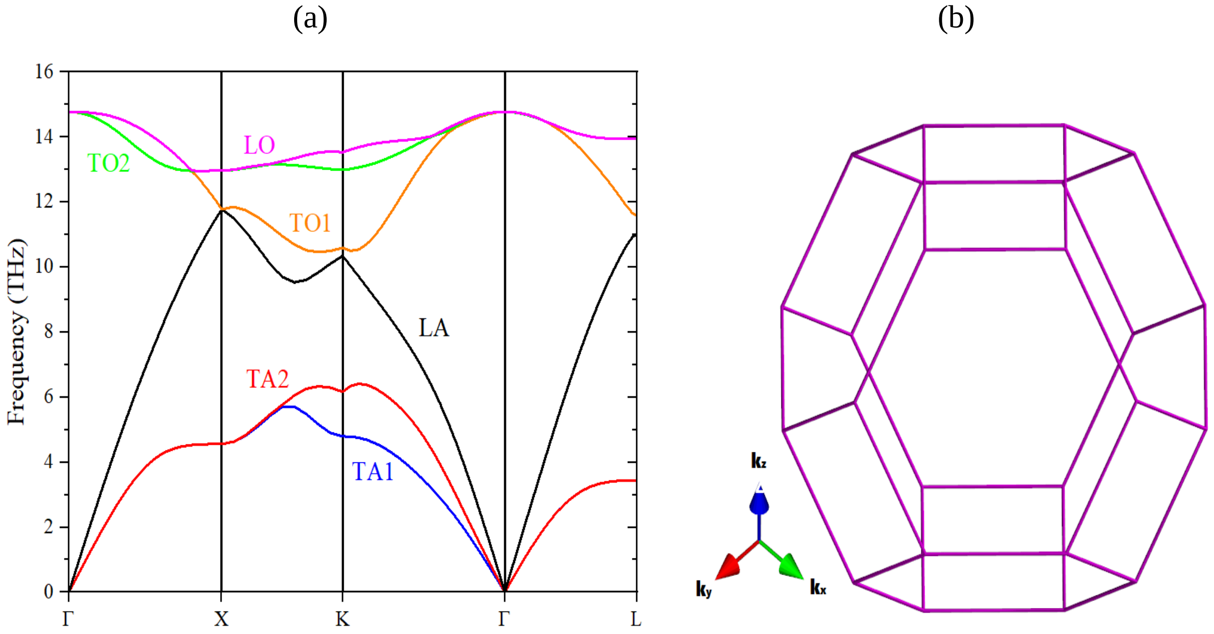

Figure 2.5: (a) Calculated phonon dispersions of silicon. (b) First Brillouin zone of the FCC lattice.

A related concept of the phonon dispersion is the phonon density of states (PDOS) ‘g(ω)’. Density of states is defined as the number of quantum states per unit volume per unit wavevector interval. The quantity g(ω)Δω measures the number of phonon states with frequencies in the range [ω, (ω + Δω)], regardless of which wavevectors ‘κ’ or modes ‘*s*’ these frequencies refer to [23]. In three-dimensional oscillation with *N* atoms, there are 3*N* phonon states in total. It is required for the PDOS to be normalized per atom, or per lattice primitive cell. In contrast, g(ω) does not relate to a specific atom in a material having multiple types of atoms but rather to the average of overall vibration modes, defined as

$$g(\omega)=\frac{V}{(2\pi)^{3}}\frac{1}{N}\sum_{s}\int d^{3}\kappa\,\delta(\omega(\kappa,s)-\omega) \tag{2.17}$$

where V is the volume of crystal and δ is the Dirac-function. In κ-space, one phonon state has a volume of $(2\pi)^3/V$. PDOS for crystal silicon is shown in Figure 2.6.

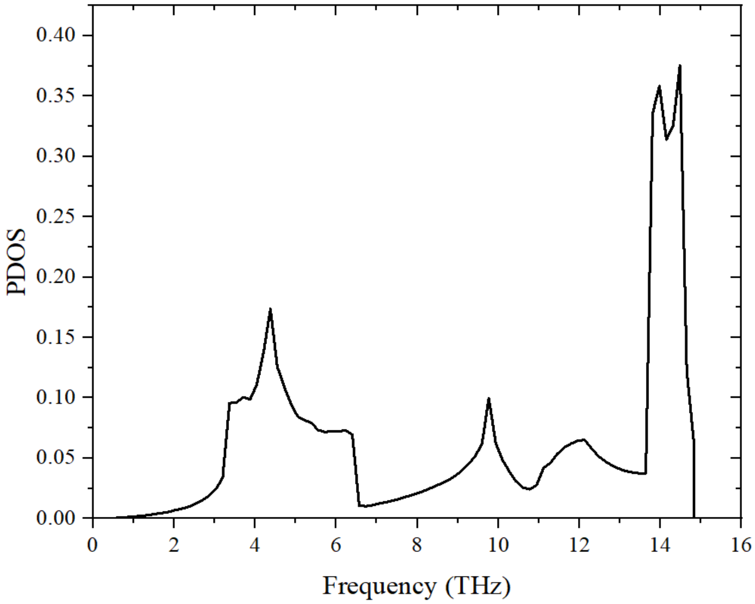

Figure 2.6: Calculated phonon density of states for silicon.

2.1.1.4 Elastic Constants of Crystals

When describing elastic properties, a crystal is seen as a homogenous medium according to the classical continuum mechanics. The study of mechanical properties provides useful information of the impact of temperature, pressure, etc. It is known that elastic strain is related to stress by Hooke's law. The fourth rank of the elastic constant tensor 'C_{ijkl}', consisting of 81 *independent components,* associates the stress and strain tensors as

$$\sigma_{ij} = C_{ijkl}\varepsilon_{kl} \tag{2.18}$$

where *i, j, k,* and *l* are vector components.

Because of the symmetry of stress and strain tensors, the number of independent components may reduce to 21 [24]. Voigt notation, which replaces pairs of indices with single indices, is commonly used for convenience (e.g., 11→1, 31→5). In 1964, Nye [24] tabulated the elastic constant tensor for each crystal symmetry. For a cubic crystal, there are only three independent components (C_{11}, C_{12}, and C_{44}). The elastic constants matrix is given as

$$\mathrm{C}_{ij}=\begin{bmatrix}\mathrm{C}_{11} & \mathrm{C}_{12} & \mathrm{C}_{12} & 0 & 0 & 0\\ \mathrm{C}_{12} & \mathrm{C}_{11} & \mathrm{C}_{12} & 0 & 0 & 0\\ \mathrm{C}_{12} & \mathrm{C}_{12} & \mathrm{C}_{11} & 0 & 0 & 0\\ 0 & 0 & 0 & \mathrm{C}_{44} & 0 & 0\\ 0 & 0 & 0 & 0 & \mathrm{C}_{44} & 0\\ 0 & 0 & 0 & 0 & 0 & \mathrm{C}_{44}\end{bmatrix} \tag{2.19}$$

The equation of motion of an elastic medium in the *x*-direction can be written in terms of elastic constants as

$$\rho\frac{\partial^2 u_x}{\partial t^2}=C_{11}\frac{\partial e_{xx}}{\partial x}+C_{12}\left(\frac{\partial e_{yy}}{\partial x}+\frac{\partial e_{zz}}{\partial x}\right)+C_{44}\left(\frac{\partial e_{xy}}{\partial y}+\frac{\partial e_{xz}}{\partial z}\right) \tag{2.20}$$

where *e* is the strain component

$$e_{xx}=\varepsilon_{xx}, e_{yy}=\varepsilon_{yy}, e_{zz}=\varepsilon_{zz} \tag{2.21}$$

For phonons, there exists a relationship between the elastic constants ‘C_{ij}’ and the interatomic force constants ‘ Φ ’ since the frequencies of all phonon modes are determined by atom masses and interatomic force constants. The mathematical expression that represents this relation is

$$\mathrm{C}_{ij}=\frac{1}{2\mathrm{V}^*}\sum_{ij}\Phi_{\alpha\beta}u_\alpha u_\beta \tag{2.22}$$

where Φ_{ij} is the interatomic force constants of the harmonic approximation, V^* is the volume of the unit cell, and α, β are Cartesian coordinates.

Interatomic force constants can be related to elastic constants based on the structure of the unit cell, where Φ_1 and Φ_2 are the interatomic force constants between nearest and next-nearest neighbors with a constant lattice of ‘*a*’. For FCC structure

$$\frac{\Phi_1}{a}=\mathrm{C}_{44},\quad \frac{4\Phi_2}{a}=\mathrm{C}_{11}-\mathrm{C}_{12}-\mathrm{C}_{44} \tag{2.23}$$

For BCC structure

$$\frac{2\Phi_1}{3} = C_{44}, \quad \frac{2\Phi_2}{a} = C_{11} - C_{12} \tag{2.24}$$

The bulk modulus ‘B’ is defined as

$$B = V\frac{\partial^2 P}{\partial V^2} \tag{2.25}$$

where P is the pressure. Bulk modulus for a cubic crystal can be expressed in terms of elastic constants as

$$B = \frac{1}{3}\left(C_{11} + 2C_{12}\right) \tag{2.26}$$

Elastic constants can be used to determine the stability of the crystal. For instance, the crystal is unstable when one of the transverse modes causes shear [25]. In this scenario, the charge of C_{44} is negative in the case of a cubic crystal. Elastic constants for some crystals are given in Table 2.1.

Table 2.1: Elastic constants C_{ij} for common crystals in unit of 10^{12} dyn/cm^2 at room temperature.

Crystal	Lattice structure	C_{11}	C_{12}	C_{13}	C_{14}	C_{33}	C_{44}	C_{55}	Ref.
Silicon	Cubic	1.6578	0.6394	-	-	-	0.7962	-	[26]
Sodium	Cubic	0.0739	0.0622	-	-	-	0.0419	-	[27]
Cobalt	Hexagonal	3.071	1.650	1.027	-	3.581	-	0.755	[28]
Magnesium	Hexagonal	0.5950	0.2612	0.2180	-	0.6155	-	0.1635	[29]
Bismuth	Trigonal	0.637	0.249	0.247	0.072	0.382	0.112	-	[30]

2.1.2 Anharmonicity

Phonons are independent of one another in the harmonic approximation. However, the vibrations of real crystals are not quite harmonic. For a monoatomic anharmonic linear chain with nearest-neighbor interactions, the equation of motion by using the Taylor series is

$$\begin{aligned} m\frac{\partial^2 u_n}{\partial t^2} &= \mathrm{a}_1[(u_{n+1}-u_n)-(u_n-u_{n-1})] \\ &+\frac{1}{2!}\mathrm{a}_2[(u_{n+1}-u_n)^2-(u_n-u_{n-1})^2] \\ &+\frac{1}{3!}\mathrm{a}_3[(u_{n+1}-u_n)^3-(u_n-u_{n-1})^3]+\ldots \end{aligned} \tag{2.27}$$

For the harmonic oscillator ($a_2 = a_3 = a_{n+3} = 0$), the previously discussed one-dimensional problem is recovered. Higher-order terms are commonly referred to as anharmonic terms. In a nonlinear system, the difficulty in solving Eq. (2.27) arises when anharmonicity effect is strong.

In 1955, a nonlinear dynamical system were studied by Fermi, Pasta, Ulam, and Tsingou, known as FPUT problem [31]. For a monoatomic chain, the equation of motion of FPUT on the n^{th} atom can be written as

$$m\frac{\partial^2 u_n}{\partial t^2} = K(u_{n+1}-2u_n+u_{n-1})+\alpha[(u_{n+1}-u_n)^2-(u_n-u_{n-1})^2] \tag{2.28}$$

$$m\frac{\partial^2 u_n}{\partial t^2} = K(u_{n+1}-2u_n+u_{n-1})+\beta[(u_{n+1}-u_n)^3-(u_n-u_{n-1})^3] \tag{2.29}$$

where α, β represent quadratic and cubic coefficients of the nonlinear force, respectively. Eqs. (2.28) and (2.29) are also known as FPUT α- and β-models, respectively. The theories of Solitons and Chaos place a great deal of emphasis on the FPUT problem [32]. The quadratic FPUT problem was connected to the Korteweg–de Vries equation (KdV equation [33]) by Zabusky and Kruskal in 1965, considering the continuum limit [34]. In this numerical study, Solitons were observed as 'solitary-wave pulses' rather than summing together to form a linear-wave superposition [34]. By modeling a monoatomic chain, FPUT has been used to investigate the dynamics of a crystal as it approaches thermal equilibrium, linked by a quadratic interaction potential [35]. The Hamiltonian of a monoatomic chain is expressed by

$$H = \frac{1}{2}\sum_{n=0}^{N} {p_n}^2 + \frac{1}{2}\sum_{n=0}^{N}(u_{n+1} - u_n)^2 + \frac{\alpha}{3}\sum_{n=0}^{N}(u_{n+1} - u_n)^3 \tag{2.30}$$

where p_n is the momentum of atom n.

For three-dimensional real crystals, the interatomic potential energy *'V'* of the displacement atom can be written by using the Taylor series as

$$\begin{aligned} V &= V_0 + \sum_{ij\alpha} \left.\frac{\partial V}{\partial u_\alpha(ij)}\right|_0 u_\alpha(ij) \\ &\quad + \frac{1}{2!}\sum_{ij,i'j'}\sum_{\alpha\beta} \left.\frac{\partial^2 V}{\partial u_\alpha(ij)\partial u_\beta(i'j')}\right|_0 u_\alpha(ij)u_\beta(i'j') \\ &\quad + \frac{1}{3!}\sum_{ij,i'j',i''j''}\sum_{\alpha\beta\gamma} \left.\frac{\partial^3 V}{\partial u_\alpha(ij)\partial u_\beta(i'j')\partial u_\gamma(i''j'')}\right|_0 u_\alpha(ij)u_\beta(i'j')u_\gamma(i''j'') + \ldots \\ &= V_0 + V_1 + V_2 + V_3 + \ldots \end{aligned} \tag{2.31}$$

where *i* and *j* are vector positions in a unit cell and α, β, and γ are Cartesian coordinates. The first derivative can be set to zero at the equilibrium, thus

$$\begin{aligned} V &= V_0 + \frac{1}{2!}\sum_{ij,i'j'}\sum_{\alpha\beta} \Phi_{\alpha\beta}(ij,i'j')u_\alpha(ij)u_\beta(i'j') \\ &\quad + \frac{1}{3!}\sum_{ij,i'j',i''j''}\sum_{\alpha\beta\gamma} \Phi_{\alpha\beta\gamma}(ij,i'j',i''j'')u_\alpha(ij)u_\beta(i'j')u_\gamma(i''j'') + \ldots \end{aligned} \tag{2.32}$$

where $\Phi_{\alpha\beta}$ and $\Phi_{\alpha\beta\gamma}$ are the second and third-order interatomic forces, respectively

$$\Phi_{\alpha\beta}(ij,i'j') = \left.\frac{\partial^2 V}{\partial u_\alpha(ij)\partial u_\beta(i'j')}\right|_0 \tag{2.33}$$

$$\Phi_{\alpha\beta\gamma}(ij,i'j',i''j'') = \left.\frac{\partial^3 V}{\partial u_\alpha(ij)\partial u_\beta(i'j')\partial u_\gamma(i''j'')}\right|_0 \tag{2.34}$$

Thus, the Hamiltonian *'H'* of a real crystal can be expressed as

$$H = E_k + V \tag{2.35}$$

where E_k is the kinetic energy.

As a result, it is shown that phonons can exchange energy with one another and are not independent. Time-dependent perturbation theory is one approach used to treat non-separable dynamical systems and represents the transition probabilities. Application of time-dependent perturbation theory provides a straightforward approach to describe the transition rates due to a weak perturbation, summarized by Fermi's Golden rule [36].

$$W(1\rightarrow 2)=\frac{2\pi}{\hbar}\left|\int \Psi_2^* H' \Psi_1 d^3r\right|^2 \delta(E_2-E_1) \tag{2.36}$$

where W is the transition rate from a momentum p_1 with a quantum state Ψ_1 to another (p_2, Ψ_2) and $d^3r = dx\, dy\, dz$.

The integral term is called the scattering matrix, can be written using Dirac notations as

$$\int \Psi_2^* H' \Psi_1 d^3r = \left\langle 1\middle|H'\middle|2\right\rangle \tag{2.37}$$

The statement of energy conservation is expressed by the delta-function. If $E_1 = E_2$, delta-function = 1; otherwise, delta-function = 0.

Due to its straightforward mathematical expression, Fermi's golden rule has become standard for calculating phonon scattering rates 'τ^{-1}'. By implementing Fermi's golden rule, scattering rates of emission 'τ_{emi}^{-1}' and absorption 'τ_{abs}^{-1}' processes from the initial state 'i' to final state 'f' can be described as

$$\tau_{emi}^{-1}=\frac{2\pi}{\hbar}\left|\left\langle \mathrm{i}\middle|H'\middle|\mathrm{f}\right\rangle\right|^2 \delta(E_\mathrm{f}-E_\mathrm{i}+\hbar\omega) \tag{2.38}$$

$$\tau_{abs}^{-1}=\frac{2\pi}{\hbar}\left|\left\langle \mathrm{i}\middle|H'\middle|\mathrm{f}\right\rangle\right|^2 \delta(E_\mathrm{f}-E_\mathrm{i}-\hbar\omega) \tag{2.39}$$

Phonon scattering may enable an electron to either absorb energy (phonon absorption) or allow some of its own energy to be lost (phonon emission). The most important questions now are: What are the types of phonon scattering rates? What factors does it depend on? What techniques do we need to compute scattering rates?

2.1.2.1 Phonon Scattering Rates

When it comes to modeling heat transport in materials, understanding scattering mechanisms is crucial. In fact, the source of phonon scattering is the anharmonic force interaction as described in Eq. (2.32). The second-order term, Eq. (2.33), represents the harmonic oscillator model while Eq. (2.34) and higher-orders represent the anharmonic oscillator model. The scattering of gas atoms considers an example of phonon scattering. Figure 2.7 illustrates three-phonon creation-annihilation processes. (a) Combination of two phonons into one (merging or annihilation process), where both momentum and energy must be conserved

$$\hbar\kappa_1 + \hbar\kappa_2 = \hbar\kappa_3 \tag{2.40}$$

$$\hbar\omega_1 + \hbar\omega_2 = \hbar\omega_3 \tag{2.41}$$

Since the total momentum of the phonon is conserved, this type has a minor effect on the heat flux [37]. (b) Breaking up a phonon into two (splitting or creation process). This type of scattering shown in Figures 2.7 (a) and (b) is called the *Normal process* (N-process) or *Normal scattering*.

(c) Another type of phonon scattering is called the *Umklapp process* (U-process) or *Umklapp scattering*. U-process does not conserve the momentum because the momentum that results from the combination of two photons is located outside the first Brillouin zone, causing thermal resistance. Therefore, the reciprocal lattice vector '*G*' must be added to the total momentum equation balance

$$\hbar\kappa_1 + \hbar\kappa_2 = \hbar\kappa_3 + \hbar G \tag{2.42}$$

This type was proposed by Peierls [38]. If the product of merging two phonons or splitting a phonon lies in the first Brillouin zone, $G = 0$ (N-process); otherwise, $G \neq 0$ (U-process).

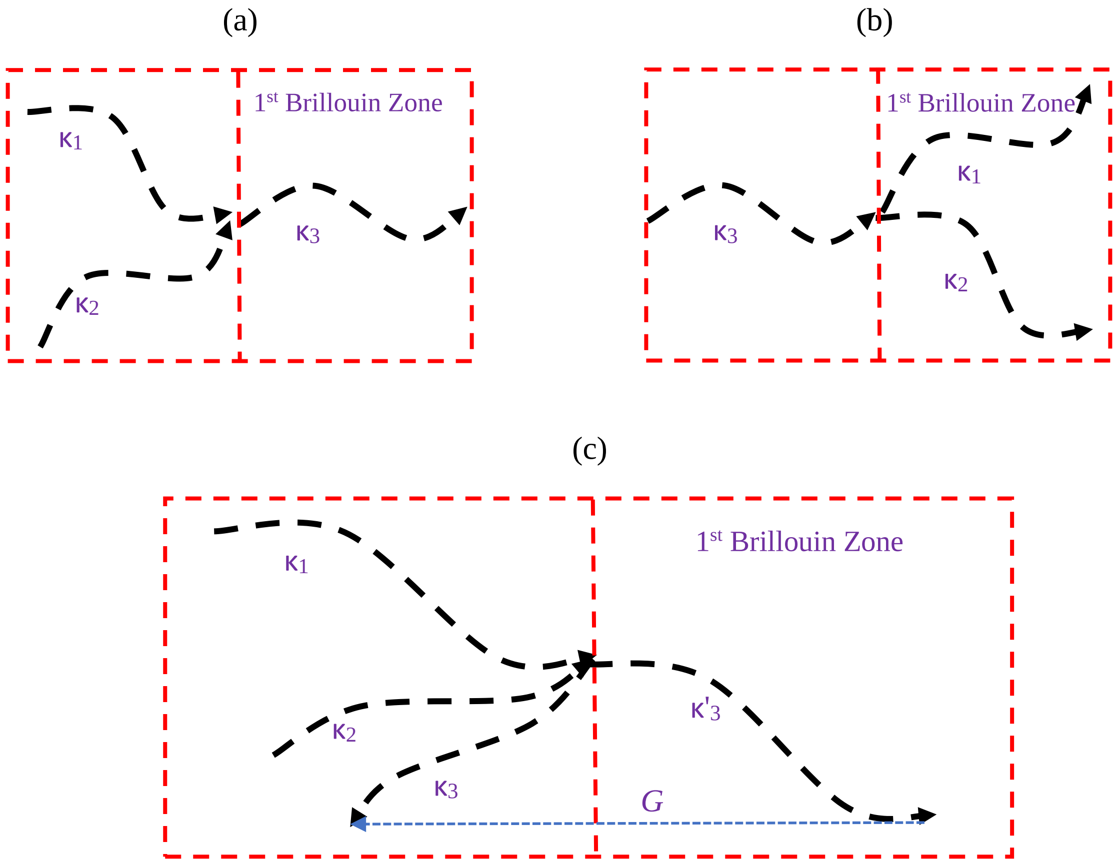

Figure 2.7: Three-phonon scattering processes: (a) Phonon annihilation process (N-process). (b) Phonon creation process (N-process). (c) Phonon annihilation process (U-process).

Callaway [39] derived N- and U-scattering rates relations, as given respectively

$$\tau_{\mathrm{N}}^{-1} = B_1 T^3 \omega^2 \tag{2.43}$$

$$\tau_{\mathrm{U}}^{-1} = B_2 T^3 \omega^2 = e^{\left(\frac{-\Theta}{b_2 T}\right)} T^3 \omega^2 \tag{2.44}$$

where B_1 and b_2 are constants and Θ is the Debye temperature. B_1 is independent of temperature, whereas B_2 does. Eq. (2.43) and Eq. (2.44) are also referred to as *relaxation time* expressions; it will be discussed in the next section. Ward and Broido [40] derived N- and U-scattering rates relations using the first-principles approach

$$\tau_{\mathrm{N}}^{-1} = B_3 \omega^2 T \left[1 - e^{\left(\frac{-3T}{\Theta}\right)} \right] \tag{2.45}$$

$$\tau_{\mathrm{U}}^{-1} = B_4 \omega^4 T \left[1 - e^{\left(\frac{-3T}{\Theta} \right)} \right] \tag{2.46}$$

where B_3 and B_4 are constants.

Phonons may scatter also from electrons, isotopes, and boundaries. Phonon-electron scattering is a significant process in semiconductors. Zou and Balandin [41] showed the relaxation time for acoustic phonon-electron at low doping levels. The conservation of energy for this type of scattering is written as

$$E_{\mathrm{i}} - E_{\mathrm{f}} = \pm \hbar \omega = \frac{\hbar}{2m_e} \left(\kappa_{\mathrm{i}}^2 - \kappa_{\mathrm{f}}^2 \right) \tag{2.47}$$

where m_e is the effective mass of the electron, subscripts κ_{i} and κ_{f} are the wavevectors of initial and final states, respectively. The positive sign (+) represents the emission process while the negative sign (-) represents the absorption process.

One way to include the effects of a physical boundary is to introduce a source of boundary scattering rate which can be done by relating the group velocity 'v_g' and the characteristic length 'L' [39]

$$\tau_B^{-1} = \frac{v_g}{L} \tag{2.48}$$

Another important scattering process is scattering from isotopes. The scattering by point defects, which includes isotopes, impurities, and vacancies, is proportional to the fourth-order of the phonon frequency according to Rayleigh law [39]

$$\tau_I^{-1} = A \omega^4 \tag{2.49}$$

The value of $A = 2.57 \times 10^{-44}$ s^3 for normal germanium was computed numerically [39]. Eq. (2.48) and Eq. (2.49) show that boundary and isotope scattering rates are independent of temperature. One may ask, how can these different scattering rates be calculated and how do they contribute to thermal transport? To answer this question, the machinery of statistical mechanics and the Boltzmann Transport Equation (BTE) will be used.

2.1.2.2 Boltzmann Transport Equation (BTE)

The phonon Boltzmann transport equation (BTE) has emerged as a powerful equation for describing phonon transport in crystals. It was first used to describe the behavior of a dilute gas system and has since been used in a wide range of other applications, including the transport of electrons in semiconductors, quantum fluids, and neutrons transport [42]. Before stating the BTE, it is worth understanding its origin, the Liouville equation

$$\frac{\partial f^{(N)}}{\partial t}+\sum_{i=1}^{n}\dot{r}^{(i)}\frac{\partial f^{(N)}}{\partial r^{(i)}}+\sum_{i=1}^{n}\dot{p}^{(i)}\frac{\partial f^{(N)}}{\partial p^{(i)}}=0 \tag{2.50}$$

Eq. (2.50) is based on distribution function (r, κ, *t*), which is the probability of locating a particle (e.g., atom) at a position ‘r’, wavevector ‘κ’, and occupied at time ‘*t*’. The Liouville equation has a massive number of variables, making it practically impossible to solve analytically or numerically. To demonstrate the intricacy of the Liouville equation, we first consider a collision process for two particles, where the distribution functions for these particles before the collision are f (r, κ_1, t), f (r, κ_2, t), and after the collision are f (r, κ_1^*, t), f (r, κ_2^*, t). The scattering for two particles at state ‘κ’ is

$$\begin{aligned}\left(\frac{\partial f}{\partial t}\right)_c =& -\sum_{\kappa_2,\kappa_1^*,\kappa_2^*} f(r,\kappa_1,t)f(r,\kappa_2,t)W(\kappa_1,\kappa_2\rightarrow\kappa_1^*,\kappa_2^*)\\ &+\sum_{\kappa_2,\kappa_1^*,\kappa_2^*} f(r,\kappa_1^*,t)f(r,\kappa_2^*,t)W(\kappa_1^*,\kappa_2^*\rightarrow\kappa_1,\kappa_2)\end{aligned} \tag{2.51}$$

BTE was derived from the Liouville equation (Eq. 50) by performing an average over the momentum and space coordinates of the other (N-1) particles [8], which can be written as [43]

$$\frac{\partial f}{\partial t}+v_g.\frac{\partial f}{\partial r}=\left[\frac{\partial f}{\partial t}\right]_c \tag{2.52}$$

The phonon dispersion relations and phonon scattering rates are required as inputs to the BTE. While the complexity of the BTE is reduced relative to the Liouville equation, solving the BTE is not trivial due to the integral nature of the collision term and the multi-dimensions of the distribution function (i.e., f (x, y, z, κ_x, κ_y, κ_z, t)). The rate of change the distribution function is a result of two mechanisms, including diffusion and scattering. At steady-state, BTE is expressed by

$$\left.\frac{\partial f}{\partial t}\right|_{diffusion} + \left.\frac{\partial f}{\partial t}\right|_{scattering} = 0 \tag{2.53}$$

where

$$\left.\frac{\partial f}{\partial t}\right|_{diffusion} = -v_g.\nabla T \frac{\partial f}{\partial T} \tag{2.54}$$

Transport occurs due to the presence of the temperature gradient (∇T). To simplify the collision term, one can use relaxation time approximation (RTA)

$$\left(\frac{\partial f}{\partial t}\right)_c = \frac{f - f^0}{\tau} \tag{2.55}$$

where τ is the relaxation time, measures the time taken to return to the equilibrium. f^0 is the equilibrium distribution function (i.e., Bose-Einstein distribution)

$$f^0 = \left\{ \frac{1}{e^{\frac{\hbar\omega}{k_B T}} - 1} \right\} \tag{2.56}$$

where k_B is the Boltzmann's constant and $\hbar$ is the modified Planck's constant. The total relaxation time 'τ_t' can be calculated based on Matthiessen's rule [22]

$$\begin{aligned} \frac{1}{\tau_t} &= \sum \frac{1}{\tau_i} \\ &= \frac{1}{\tau_U} + \frac{1}{\tau_B} + \frac{1}{\tau_I} \end{aligned} \tag{2.57}$$

The relaxation time according to RTA is

$$\frac{1}{\tau} = \frac{1}{\tau_N} + \frac{1}{\tau_U} \tag{2.58}$$

Under the RTA, BTE becomes

$$\frac{\partial f}{\partial t} + v_g.\frac{\partial f}{\partial r} = \frac{f - f^0}{\tau} \tag{2.59}$$

There are many approaches to solving the BTE under the RTA, but for brevity, a few are mentioned here. Monte-Carlo methods are the most common numerical methods to solve BTE. It may be used in other applications, such as charge transport [44] and gas dynamics [45]. Klistner *et al.* [46] applied Monte-Carlo to study heat transport in the ballistic limit. The first detailed algorithm to solve BTE via the Monte-Carlo approach to study phonon transport in solid thin films was proposed by Mazumder and Majumdar [47]. This approach accounts for the frequency-dependent phonon lifetimes as well as phonon transitions between polarisation branches [47]. It is beneficial to implement the Monte-Carlo technique to solve BTE because it can consider the phonon dispersion relation and treat each phonon scattering event separately.

In contrast, the relaxation time approximation (RTA) method is the simplest analytical approach to solve BTE, where the transport is spatially and temporally independent [48]. The variational method is an effective method to solve the linearized Boltzmann equation [49]. According to the fundamentals of the variational method, the trial function takes the place of the exact solution. Chiloyan *et al.* [50] developed the variational approach to solve BTE in transient thermal grating (TTG) for thin films.

2.1.3 Thermal Properties

To determine the temperature distribution on the macroscopic scale, one typically studies thermal transport within a continuum framework. The macroscopic expression gives the heat energy flow per unit area q (heat flux) to the temperature gradient ∇T as

$$q = -k\nabla T \tag{2.60}$$

where k is the thermal conductivity. On an atomic scale, however, thermal transport within a quantum framework must be considered in order to obtain an expression for thermal conductivity [51]. Thermal conductivity is infinite in harmonic approximation due to the absence of phonon interactions. In an anharmonic system, phonons collide with each other and lead to a limitation of thermal conductivity. The process that eventually limits the thermal conductivity in a perfect crystal is resistive scattering. This is because of the ability of the reciprocal wavevector ‘G’ to change the net direction propagation, and hence it will resist the heat flow [38]. Several analytical models based on BTE have been presented to determine thermal conductivity. Callaway [39] proposed a model to calculate the lattice thermal conductivity ‘k_L’, which is valid in the range of (2.0 K to 100 K) for germanium. However, it was assumed that there is no difference between longitudinal and transverse phonons and that the branches of phonons are non-dispersive [39]. Holland [52] improved Callaway's model by considering phonon dispersion effects. According to statistical mechanics, heat carriers produced by thermal sources randomly walk in all directions. Therefore, some sort of averaging is required for macroscopic descriptions of the motion of the heat carrier (i.e., Fourier's law for heat transfer and Fick’s law for mass diffusion) [8]. To derive the thermal conductivity from Fourier’s law based on kinetic theory, we consider a 1D model, as shown in Figure 2.8. The net heat flux in x-direction ‘q_x’ that crosses the vertical dashed line is the difference between the heat fluxes flowing in positive and negative directions

$$q_x = -\frac{1}{2}(nEv_{g,x})\Big|_{x+v\tau_x} + \frac{1}{2}(nEv_{g,x})\Big|_{x-v\tau_x} \tag{2.61}$$

where n is the number of particles per unit volume, $v_{g,x}$ is the group velocity in the x-direction, and E is the energy of a particle. The factor (1/2) means that half of the particles flow in the positive direction, whereas the other half particles flow in the negative direction. Eq. (2.61) can be expressed using the Taylor series as

$$q_x = -v_{g,x}\tau \frac{d(nEv_{g,x})}{dx} \tag{2.62}$$

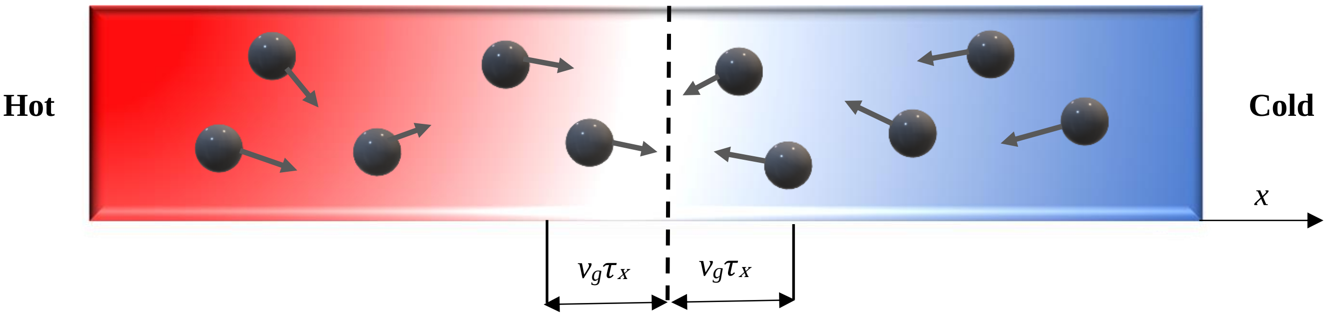

Figure 2.8: Particles movement in one-dimension.

We assume that $v_{g,x}^2 = v_{g,y}^2 = v_{g,z}^2 = (1/3)v_g^2$

$$q_x = -\frac{v_g^2 \tau}{3} \frac{dE_n}{dT} \frac{dT}{dx} \tag{2.63}$$

where $E_n = nE$ is the energy density per unit volume and ($dE_n/dT = c_v$) is the volumetric specific heat at constant volume. Eq. (2.63) leads to Fourier's law

$$q_x = -\frac{c_v v_g^2 \tau}{3} \frac{dT}{dx} = -k \frac{dT}{dx} \tag{2.64}$$

The parameters of Eq. (2.64) can be obtained by solving the BTE. Thermal conductivity is expressed as

$$k = \frac{c_v v_g^2 \tau}{3} = \frac{c_v v_g \Lambda}{3} \tag{2.65}$$

where $\Lambda = v_g \tau$ is the mean free path, which is the average traveling distance of a heat carrier before scattering causes energy loss. Figure 2.9 shows the calculated thermal conductivity of silicon up to room temperature by using RTA approach

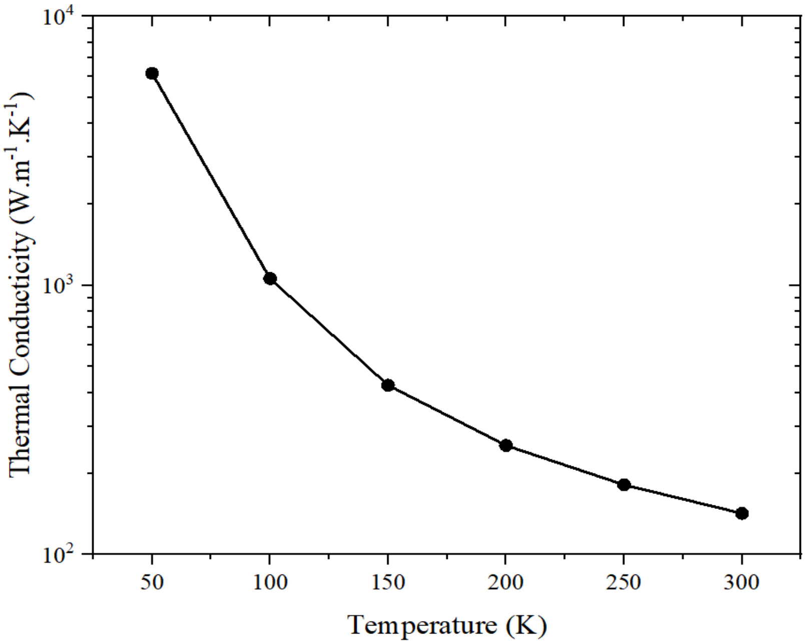

Figure 2.9: Calculated thermal conductivity of silicon using RTA approach.

The volumetric specific heat at constant volume 'c_v' also can be described in terms of equilibrium distribution function 'f^0' as

$$c_v = \frac{k_B}{\mathrm{V}^* N^*} \sum \left(\frac{\hbar\omega}{k_B T} \right)^2 f^0 (1 + f^0) \tag{2.66}$$

where N^* is the total number of q-points (phonon wave vectors) grid. For solids, specific heat at constant volume 'c_v' and specific heat at constant pressure are almost identical 'c_p'

$$c_v \approx c_p \tag{2.67}$$

This is because the change in the volume is negligible due to very small interparticle spaces in solids. To understand this assumption, we define the linear thermal expansion coefficient 'α'

$$\alpha = \frac{1}{3\mathrm{V}} \left(\frac{\partial \mathrm{V}}{\partial T} \right)_P \tag{2.68}$$

In harmonic approximation, the effect of the thermal expansion coefficient vanishes, thus

$$\left(\frac{\partial \mathrm{V}}{\partial T} \right)_P = - \frac{(\partial P / \partial T)_\mathrm{V}}{(\partial P / \partial \mathrm{V})_T} = 0 \tag{2.69}$$

Specific heat relation is

$$c_p = c_v - \frac{T}{\mathrm{V}} \frac{(\partial P / \partial T)^2{}_\mathrm{V}}{(\partial P / \partial \mathrm{V})_T} \approx c_v \tag{2.70}$$

In an anharmonicity case, however, we use a dimensionless called Grüneisen parameter 'γ', which describes the thermal systems and the impact of changing a crystal lattice volume

$$\gamma_i = - \frac{\mathrm{V}}{\omega_i} \frac{\partial \omega_i}{\partial \mathrm{V}} = - \frac{\partial (\ln \omega_i)}{\partial (\ln \mathrm{V})} \tag{2.71}$$

where subscript i represents a phonon mode. The average Grüneisen parameter '$\bar{\gamma}$' is related to the heat capacity 'C'

$$\bar{\gamma} = \frac{\sum \gamma_i C_i}{\sum C_i} = \frac{\sum \gamma_i C_i}{C} \tag{2.72}$$

Thermal expansion coefficient is given by

$$\alpha = \frac{\bar{\gamma} C}{3\mathrm{B}} \tag{2.73}$$

The heat capacity at mode '*i*' can be calculated by differentiating the internal energy with respect to temperature

$$C_i = \frac{dU_i}{dT} = \hbar\omega_i \frac{df^0}{d\mathrm{T}} = \hbar\omega_i \left(\frac{\left(\frac{\hbar\omega_i}{k_B}\right) e^{\left(\frac{\hbar\omega_i}{k_B T}\right)}}{T^2 \left(e^{\left(\frac{\hbar\omega_i}{k_B T}\right)} - 1 \right)^2} \right) \tag{2.74}$$

2.1.4 Phonon Hydrodynamics

In the case of strong normal scattering, the thermal conductivity increases significantly, and the flow of phonons can become collective, giving rise to phonon hydrodynamics. One signature of phonon hydrodynamics is *second sound*, which was observed experimentally in a handful of materials in the past several decades [1]–[3], [13], [53]. This phenomenon establishes the existence of wavelike propagation of thermal energy, which was interpreted first by Landau [54] based on the superfluidity theory of Helium II. The earliest second sound observation was in liquid helium at a low temperature of below 2.17 K [1]. For solids, the second sound was observed in Bi in the range of (1.2 - 4.0 K) [2] and NaF at ~ 15 K [3]. Recent studies reported the second sound in graphite above 100 K using a transient thermal grating technique [55] and above 200 K using a sub-picosecond transient grating technique [56].

Theoretical conditions for the existence phonon hydrodynamics was attempted by Guyer and Krumhansl, henceforth referred to as Guyer's condition [14]. This condition states that phonon hydrodynamics can be observed if the average boundary scattering rate $\left\langle \tau_B^{-1} \right\rangle$ is greater than the average Umklapp scattering rate $\left\langle \tau_U^{-1} \right\rangle$ but less than the average Normal scattering rate $\left\langle \tau_N^{-1} \right\rangle$ at a given temperature and a characteristic length [14]

$$\left\langle \tau_N^{-1} \right\rangle > \left\langle \tau_B^{-1} \right\rangle > \left\langle \tau_U^{-1} \right\rangle \tag{2.75}$$

In other words, phonon hydrodynamics can be observed if Normal scattering dominates over Umklapp scattering. This condition is also valid for Poiseuille's flow (Poiseuille hydrodynamic). The average resistive scattering rate $\left\langle \tau_R^{-1} \right\rangle$ (sum of Umklapp and isotope scattering rates) can also be used instead of the average Umklapp scattering rate

$$\left\langle \tau_N^{-1} \right\rangle > \left\langle \tau_B^{-1} \right\rangle > \left\langle \tau_R^{-1} \right\rangle \tag{2.76}$$

where $\left\langle \; \right\rangle$ represents the average. At a given temperature, each phonon mode has several phonon scattering rates (Normal, Umklapp, Boundary, and Isotopes). Therefore, for each type of phonon scattering rate, the average scattering rate is calculated, representing all phonon modes at a single temperature

$$\left\langle \tau^{-1} \right\rangle = \frac{\sum \tau_i^{-1} C_i}{\sum C_i} = \frac{\sum \tau_i^{-1} C_i}{C} \tag{2.77}$$

As discussed in the introduction, the ballistic regime occurs when mean free path is greater than the characteristic length. In this regime, the Normal and Umklapp phonon scattering rates are much weaker (effectively zero) than the boundary phonon scattering rate. The diffusive regime occurs when the characteristic length is much greater than all the mean free paths.

$$\textbf{Ballistic}: \left\langle \tau_B^{-1} \right\rangle > \left\langle \tau_N^{-1} \right\rangle, \left\langle \tau_B^{-1} \right\rangle > \left\langle \tau_U^{-1} \right\rangle \tag{2.78}$$

$$\textbf{Diffusive}: \left\langle \tau_U^{-1} \right\rangle > \left\langle \tau_N^{-1} \right\rangle, \left\langle \tau_U^{-1} \right\rangle > \left\langle \tau_B^{-1} \right\rangle \tag{2.79}$$

Therefore, the hydrodynamics regime, if it exists, should occur between the ballistic and diffusive regimes. There are two types of second sound; drifting and driftless [57], [58]. N-scattering must predominate to have a 'drifting' second sound. Hardy [58] stated that the presence of the second sound is not necessarily dependent upon the dominance of N-scattering. The 'driftless' second sound happens when all the scattering operator's eigenstates have the same amount of time to relax, which does not need strong N-scattering [59]. So far, experimentalists have not observed a driftless type of second sound.

2.2 Computational Methods

A bottom-up framework has been developed for studying thermal transport in the phonon hydrodynamics regime. In solids, microscopic methods rely on solving the equations of motion, such as Newton's laws of motion, which can be accomplished using Molecular Dynamics (MD). However, MD traditionally relies on empirical potentials and is therefore of limited use in accurately predicting real material properties. To obtain physically accurate properties, the quantum mechanics of atoms must be considered, which involves attempting to solving the many-body Schrodinger equation.

$$i\hbar \frac{d}{dt}\left|\psi(t)\right\rangle = H\left|\psi(t)\right\rangle \tag{2.80}$$

The first-principles method based on density functional theory (DFT) bypasses the challenge of solving the many-body Schrödinger equation through a sequence of approximations. Kohn–Sham equations deal with a single electron approximation in an effective potential '$V_e(r)$' [60].

$$\left[-\frac{\hbar^2}{2m_e}\nabla_r^2 + V_e(r)\right]\psi_i(r) = \varepsilon_i \psi_i(r) \tag{2.81}$$

By solving the Kohn–Sham equations, one can obtain a description of the interatomic force constants. However, the bypassing of the original many-body problem comes at a cost. An approximation technique for the exchange-correlation energy functional, called a pseudopotential, is required to determine the energies and wave functions of a many-body system. In this work, we examine the effect of various pseudopotentials on the material properties and phonon hydrodynamics regime. Local density approximation (LDA) is the oldest pseudopotential technique used, which was first proposed by Kohn and Sham in 1965 [60]. In LDA, the exchange-correlation energy of an inhomogeneous system can be determined based on the exchange-correlation energy for each particle in a homogeneous electron gas [60]

$$E_{xc}^{LDA}\left[\rho(r)\right] = \int \rho(r) E_{xc}^{\hom}(\rho(r))dr \tag{2.82}$$

Another type of exchange-correlation energy is based on the generalized gradient approximations (GGA). Since the exchange-correlation energy is dependent on the electron density ‘ρ(*r*)’ and its gradient ‘∇ρ(r)’, It is expected to perform more effectively with finite systems [61]

$$E_{xc}^{GGA}\left[\rho(r)\right]=\int\rho(r)E_{xc}^{\hom}(\rho(r),\nabla\rho(r))dr \tag{2.83}$$

Many GGA functions have been suggested since there are several ways to characterize the gradient of electron density ‘∇ρ(r)’ [61]–[63]. We use two common GGA functions in this work, which are the Perdew -Burke -Ernzerhof generalized gradient approximation (PBE) [61] and the modified Perdew-Burke-Ernzerhof generalized gradient approximation (PBESOL) [63].

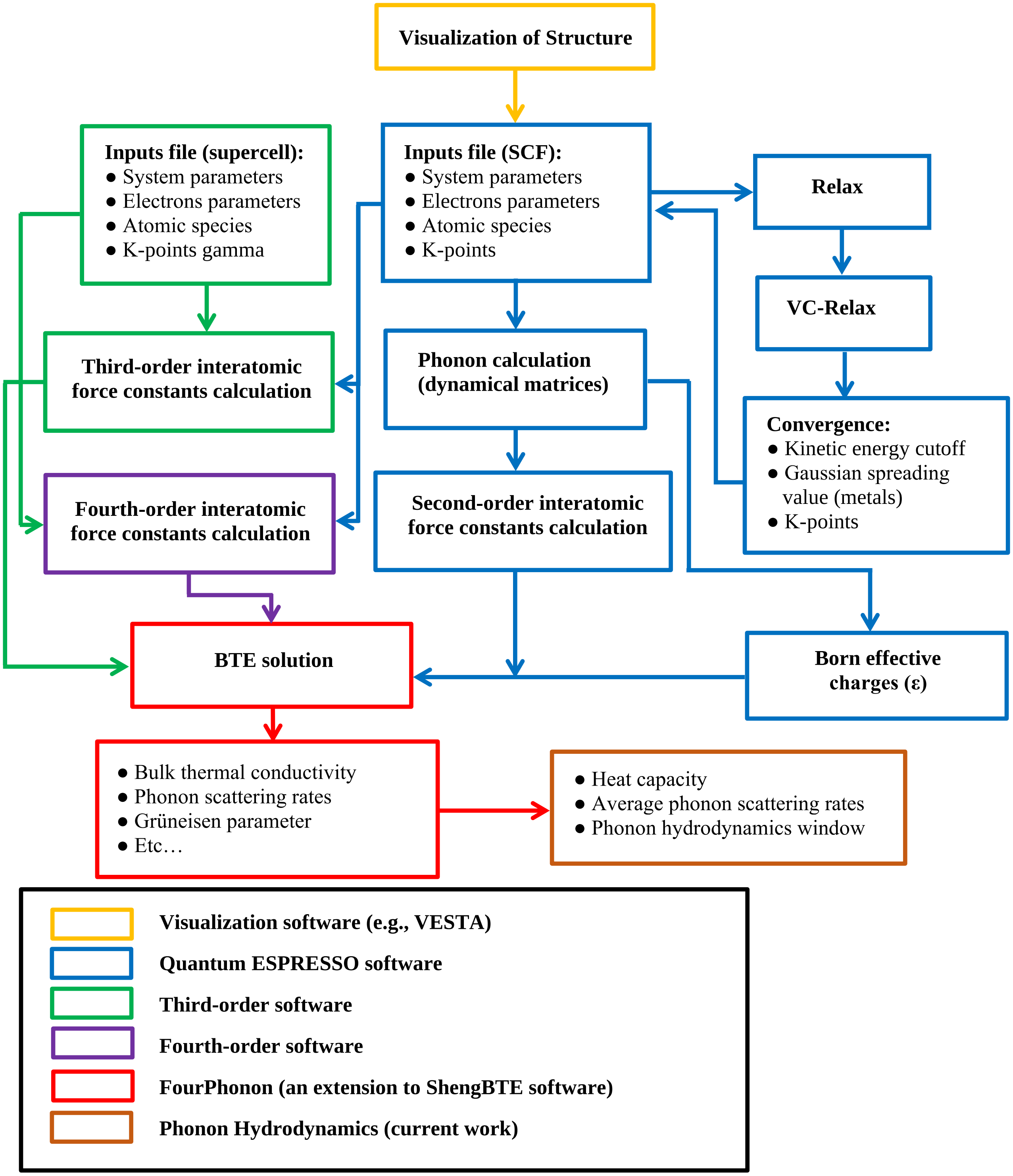

Figure 2.10: Workflow schematic.

In our workflow, as shown in Figure 2.10, we use several computational software packages to predict thermal phonon hydrodynamics based on Guyer's condition. Visualizing crystal structures is a crucial step for obtaining the initial structural data of the unit cell, including the atomic positions and unit cell dimensions. Many sophisticated software packages can visualize crystal structures (i.e., VESTA [64]). For first-principles calculations, Quantum ESPRESSO [65] is used to obtain second-order interatomic force constants, whereas thirdorder.py [66] is used to obtain third-order interatomic force constants. It should be noticed that structures of materials must be relaxed first, and some parameters (i.e., Monkhorst-Pack κ-points grid) must be converged for accuracy of calculations. There are two stages for relaxation: first, relaxation of atomic positions up to zero force (relax), and then optimization of atomic positions as well as crystal cell shape ‘cell parameters’ by variable cell-relaxation (vc-relax). The self-consistent field method is required to determine the energy of a many-body system. In this step, a pseudopotential must be selected to minimize the numerical effort.

Along with the interatomic force constants, the Born effective charges ‘Z^*’ and dielectric tensor of the solid ‘ε’ are used as additional inputs in the BTE solver for calculating the vibrational spectrum [66], [67]. For three-phonon scattering, ShengBTE is used to solve BTE [66]; in contrast, Fourphonon is used to solve BTE for four-phonon scattering [68]. Using the Python code we developed (Appendix A-5), the average scattering rates are computed to show the phonon hydrodynamics window based on Guyer’s condition at a given characteristic length.

CHAPTER 3

RESULTS AND DISCUSSIONS

3.1 Phonon Hydrodynamics in Fluorides and Alkali Hydrides

3.1.1 DFT Calculations

Density-functional theory (DFT) calculations provide valuable information necessary for the first-principles modeling of materials in the fields of material science, physics, chemistry, and engineering. DFT has been used to compute electronic structures of solids for more than five decades [69]. Due to significant technical and computational advancements, modeling the heat transfer of materials has become more manageable, especially for nanomaterials at low temperatures where the classical laws (e.g., Fourier's law) do not hold. The first-principles (*ab initio*) approach, based on DFT, has developed to become a state of the art technique to model heat transfer. However, there are always deviations of the theoretical data from experimental data. In the case of thermal conductivity of semiconductors, it is usually less than 20 % [70]. However, this error may be considered unacceptable if we seek accurate results. The goal of this chapter is to understand the impact of pseudopotential on the accuracy of the results according to the workflow (Figure 2.10) described in chapter 2.

Fluorides (NaF, LiF) and alkali hydrides (LiH, NaH) are diatomic inorganic compounds, and their applications have been studied for many years, including water treatment [71], hydrogen storage [72], [73], medical imaging [74], [75], optics [76], nuclear reactors [77], batteries [78], and many others. Several studies focused on NaF and selected it for the experiments of second sound [3], [15], [79] since there is only one naturally stable isotope of each sodium and fluorine [59], [80]. Thus, it is considered a pure crystal. Our reference is a value reported in NaF from a previous experiment in 1970 [3]. In this experiment, the heat pulse technique was used as described in Ref.[15]. By propagating the heat pulses in a NaF sample, it was found that there is a second sound at a temperature of 15 K with a characteristic length of 8.3 mm [3], as illustrated in Figure 3.1. We examine phonon hydrodynamics in NaF at the same characteristic length and different characteristic lengths based on Guyer's condition (Eq. 2.75). Average scattering rates (Normal, Umklapp, Boundary, and Isotopes) are computed depending on Eq. (2.77). Phonon thermal transport regimes are shown as a function of temperature and characteristic length. We also obtain phonon hydrodynamics of LiF, LiH, and NaH. We show the three phonon thermal transport regimes (ballistic, hydrodynamic, and diffusive) for each of these four materials. Moreover, we discuss the effect of isotopes on phonon hydrodynamics windows of these materials

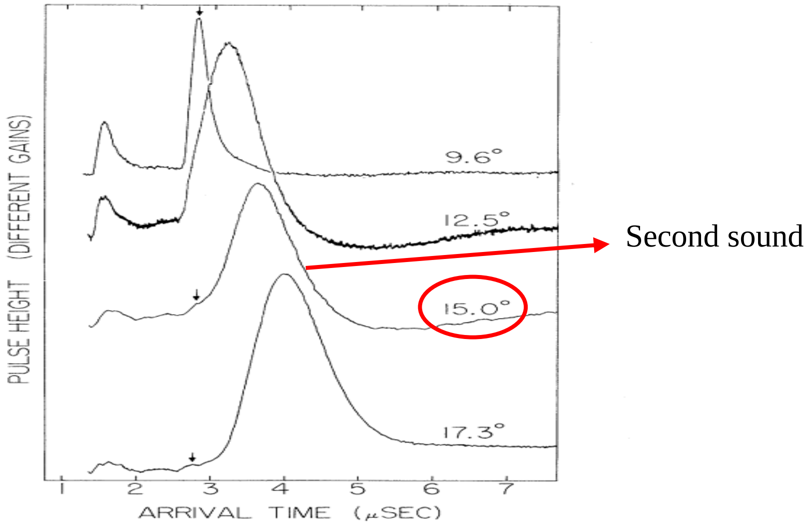

Figure 3.1: Observation of the second sound in NaF at 15 K with L = 8.3 mm (adapted from Ref.[3])

In addition, our study provides a comprehensive set of properties of fluorides (NaF, LiF) and alkali hydrides (LiH, NaH), including phonon dispersion, band gap, lattice thermal conductivity, heat capacity, bulk modulus, elastic constants, and other properties. The calculations were done using PBE, PBESOL, and LDA pseudopotentials. The structures of NaF, LiF, LiH, and NaH adopt the NaCl face-centered cubic (FCC) crystal structure. For first-principles calculations, a 14 × 14 × 14 κ-points mesh of Monkhorst-Pack with a convergence threshold of 1.0E-16 Ry is used. The number of supercells of harmonic force constants (second-order) and anharmonic force constants (third-order), cutoff, and *q* mesh are converged for each type of pseudopotential. Table 3.1 lists the supercells and *q* meshes that were obtained.

Table 3.1: The selected supercells and *q* meshes for BTE.

Material	Pseudopotential	Second-order supercell	Third-order supercell	Cutoff	*q* mesh
NaF	PBE	6 × 6 × 6	3 × 3 × 3	-2	30 × 30 ×30
	PBESOL	3 × 3 × 3	3 × 3 × 3	-5	35 × 35 ×35
	LDA	3 × 3 × 3	3 × 3 × 3	-4	40 × 40 ×40
LiF	PBE	8 × 8 × 8	3 × 3 × 3	-2	40 × 40 ×40
	PBESOL	6 × 6 × 6	3 × 3 × 3	-2	45 × 45 ×45
	LDA	6 × 6 × 6	3 × 3 × 3	-5	30 × 30 ×30
LiH	PBE	2 × 2 × 2	4 × 4 × 4	-5	45 × 45 ×45
	PBESOL	6 × 6 × 6	3 × 3 × 3	-2	40 × 40 ×40
	LDA	8 × 8 × 8	3 × 3 × 3	-2	35 × 35 ×35
NaH	PBE	3 × 3 × 3	4 × 4 × 4	-4	40 × 40 ×40
	PBESOL	4 × 4 × 4	3 × 3 × 3	-2	45 × 45 ×45
	LDA	8 × 8 × 8	3 × 3 × 3	-2	35 × 35 ×35

3.1.2 Phonon Hydrodynamics in Sodium Fluoride (NaF)

The calculated phonon dispersion and phonon density of states are shown in Figure 3.2. Phonon dispersion relations for NaF are determined in the crystallographic of {100}, {101}, and {111} symmetry directions; the path in the Brillouin zone is (Γ → X → K → Γ → L). There are six modes for NaF, LiF, LiH, and NaH: three acoustic (TA_1, TA_2, LA) and three optical (TO_1, TO_2, LO) modes, corresponding to the two atoms per primitive cell. The optical modes are located at a non-zero frequency. In the left figure, we compare the calculated and the measured phonon dispersion relations [81]. We notice that the PBE method is in excellent agreement with the measured values [81]. The agreement of calculated phonon dispersion with experiment verifies the accuracy of the calculations of the second-order interatomic force constants. The frequencies of the longitudinal and transverse optical phonon (LO-TO) at the gamma point are listed in Table 3.2.

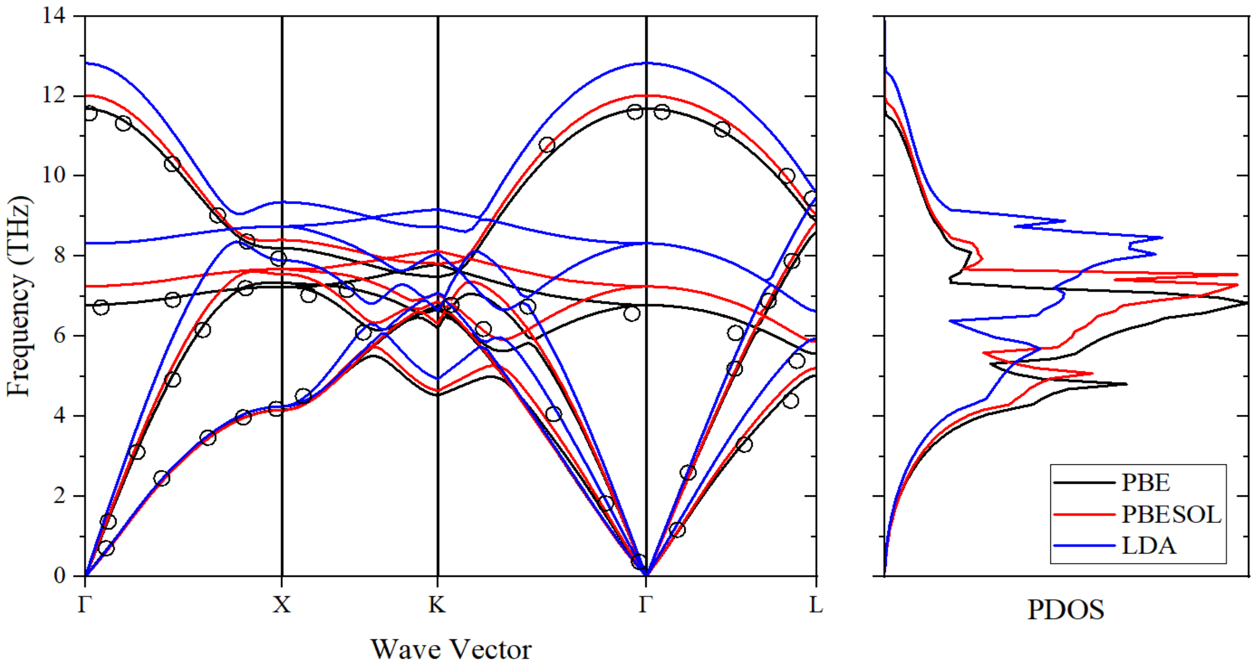

Figure 3.2: Calculated phonon dispersion (left) and phonon density of states (right) for NaF. Calculations were done with PBE (black solid lines), PBESOL (red solid lines), and LDA (blue solid lines). Black circles are the measured data from Ref.[81].

Table 3.2 compares our results with other theoretical and experimental data. The calculated equilibrium lattice constants from PBE, PBESOL, and LDA methods are 4.72, 4.65, and 4.52 Å, respectively, well-consistent with the experimental value *a*(exp) = 4.6295 Å that was measured at 0 ^{o}C by Pathak *et al.*[82]. The percentage errors (|experimental value − theoretical value| /theoretical value ×100 %) are 1.92, 0.44, and 2.42 %, respectively. The dielectric-constant tensor 'ε' and Born effective charges 'Z^{*}' are calculated based on the density functional perturbation theory (DFPT) to capture the longitudinal and transverse optical phonon (LO-TO) splitting at the gamma point [83]. For fluorides and alkali hydrides (NaF, LiF, LiH, and NaH), the underlying Bravais lattice is cubic (FCC crystal); hence there is only one independent component in the Born effective charge tensor. Our calculations for the Born effective charge using PBE are identical to the experimental value ($Z^{*}_{\text{exp}} = 1.02$) [84]. In contrast, we notice that these methods (PBE, PBESOL, and LDA) are not accurate in computing the electrical band gap. It was found that other methods, such as the modified Becke–Johnson (mBJ) exchange potential, can be used to obtain a more accurate estimate of the band gap [85]–[87]. The electrical band structures of fluoride and alkali hydride materials can be found in Appendix A-4, where the Fermi energy (E_f) is shifted to zero eV.

Table 3.2: Lattice constant *a* (Å), dielectric constant ε, Born effective charge Z^{*}, phonon frequencies at gamma ω (THz), and band gap E_g (eV) of calculated, other theoretical data, and experimental data for NaF.

	PBE	PBESOL	LDA	Other theoretical data	Experiments
a	4.72	4.65	4.52	4.67^{a}, 4.69^{b}, 4.63^{c}, 4.80^{d}, 4.695^{e1}, 4.693^{e2}	4.6295^{f}, 4.6342^{g}
ε	1.86	1.89	1.93	1.85^{e}	1.74^{h}
Z^{*}	1.02	1.01	0.99	1.019^{e}, 0.956^{i}	1.02^{j}
ω_{LO}	11.67	12.01	12.81	11.90^{e}	12.65^{k}
ω_{TO}	6.78	7.24	8.32	6.95^{e}	7.385^{k}
E_g	6.02	6.11	6.34	12.0^{a}, 6.12^{e3}, 7.11^{e4}, 11.69^{e5}	11.50^{l}

[a] Ref.[88]. [b] Ref.[89]. [c] Ref.[90]. [d] Ref.[91]. [e] Ref.[87]. [e1] Ref.[87], calculated using full-potential linearized augmented plane wave (FP-LAPW) method. [e2] Ref.[87], calculated using pseudopotential. [e3] Ref.[87], calculated using generalized gradient approximation (GGA). [e4] Ref.[87], calculated using Engel–Vosko (EV) approximation. [e5] Ref.[87], calculated using the modified Becke–Johnson (mBJ) exchange potential. [f] Ref.[82], measured at 0 ^{o}C. [g] Ref.[92]. [h] Ref.[93]. [i] Ref.[94]. [j] Ref.[84]. [k] Ref.[95]. [l] Ref.[96].

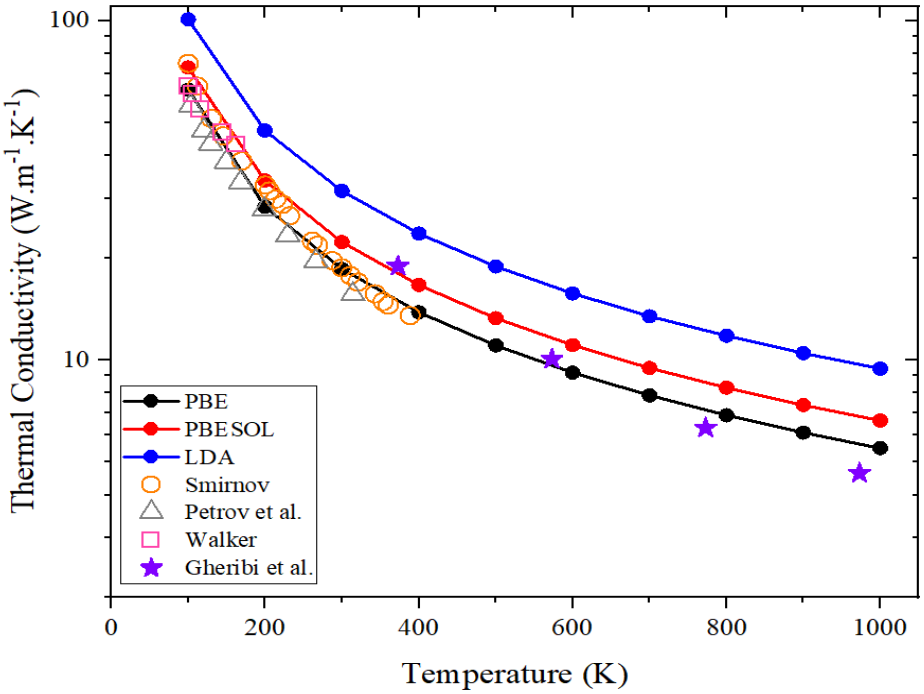

Figure 3.3: Calculated lattice thermal conductivity for NaF. Calculations were done with PBE (black circles), PBESOL (red circles), and LDA (blue circles). Experimental data: Ref.[97] (orange circles), Ref.[98] (gray triangles), Ref.[99] (pink squares). Theoretical data: Ref.[100] (purple stars).

The lattice thermal conductivity is calculated at different temperatures ranging from 100 K to 1000 K and compared with values from the literature [97]–[100], as shown in Figure 3.3. Experimental values of thermal conductivity were measured below 400 K [97]–[99]. Most experimental values are close to the PBE curve but distant from the LDA curve. Table 3.3 lists the thermal conductivity, specific heat, average Grüneisen parameter, and density values at room temperature. It shows that PBE is an accurate choice to calculate the thermal conductivity for NaF with a percentage error of 0.86 %. For the three-phonon scattering processes, the accurate Grüneisen parameter value reflects the reliability of the third-order interatomic force constants calculations (anharmonic term). All values obtained in Table 3.3 using the PBE method agree well with experimental data [97], [101]–[104].

Table 3.3: Thermal conductivity k ($W.m^{-1}.K^{-1}$), specific heat c_p ($kJ.kg^{-1}.K^{-1}$), average Grüneisen parameter $\bar{\gamma}$, and density ρ ($g.cm^{-3}$) of calculated, other theoretical data, and experimental data for NaF at room temperature.

	PBE	PBESOL	LDA	Other theoretical data	Experiments
k	18.54	22.26	31.48	-	18.7[a]
c_p	1.09	1.08	1.06	-	1.09[b]
$\bar{\gamma}$	1.78	1.61	1.59	1.79[c]	1.83[c]
ρ	2.66	2.78	3.01	2.80[d]	2.769[e], 2.804[f]

[a]Ref.[97]. [b]Ref.[101], measured at 276.20 K. [c]Ref.[102]. [d]Ref.[105]. [e]Ref.[103]. [f]Ref.[104].

The mechanical properties for NaF, including the bulk modulus and elastic constants, are given in Table 3.4. As discussed in Chapter 2, the three independent components of a cubic crystal are C_{11}, C_{12}, and C_{44}. We calculated bulk modulus ‘B’ and elastic constants ‘C_{ij}’ at 0 K of temperature. Some researchers have looked into how single-crystal elastic constants vary with temperature. Lewis *et al.* measured elastic constants of NaF at 4.2 K [103], which differ slightly from the calculated values at 0 K. Our calculated bulk modulus and elastic constants for NaF with different pseudopotential methods are in good agreement with the experimental results [103], [104], [106].

Table 3.4: Bulk modulus B (GPa) and elastic constants C_{ij} (Gpa) of calculated, other theoretical data, and experimental data for NaF.

	PBE	PBESOL	LDA	Other theoretical data	Experiments
B	46.79	48.46	61.14	40.8[a], 61.6[b]	45.7[c]
C_{11}	95.68	101.86	133.97	97.1[d], 145.14[e]	97.0[c], 108.5[f], 96.90[g]
C_{12}	22.84	21.75	24.73	24.3[d], 33.83[e]	24.3[c], 22.90[f], 24.50[g]
C_{44}	26.35	26.59	28.31	28.0[d], 33.83[e]	28.1[c], 28.99[f], 28.01[g]

[a]Ref.[91]. [b]Ref.[107], calculated using LDA pseudopotential. [c]Ref .[104]. [d]Ref.[105]. [e]Ref.[108]. [f]Ref.[103]. [g]Ref.[106].

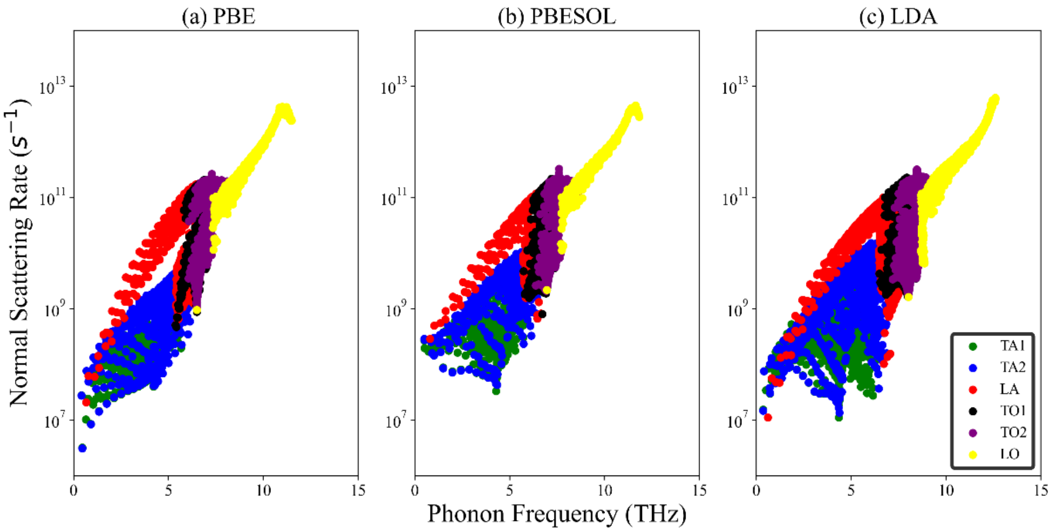

Figure 3.4: Normal scattering rates for NaF as a function of phonon frequency at T = 20 K using: (a) PBE, (b) PBESOL, and (c) LDA methods. Colorful circles denote phonon branches. The green, blue, and red circles are the acoustic phonons modes (TA_1, TA_2, LA), whereas the black, purple, and yellow circles are the optical modes (TO_1, TO_2, LO).

We present in Appendix A-3 the convergence tests for lattice thermal conductivity and average scattering rates for NaF, LiF, LiH, and NaH at 50 and 300 K, respectively, to obtain an appropriate *q*-points mesh for BTE calculation. From the calculations of thermal properties, one can extend these calculations to determine the phonon hydrodynamics window at a particular characteristic length by applying Eq. (2.75) (Guyer's condition). Figure 3.4 shows the Normal scattering rates at a temperature of 20 K with different phonon branches. According to Table 3.1, the convergence test of the *q*-points mesh for NaF produces 27,000, 42,875, and 64,000 *q*-points for PBE, PBESOL, and LDA, respectively. For all phonon modes at a given temperature, we calculate the average Normal scattering rate (ANSR). As given in Table 3.5, ANSRs at T = 20 K for PBE, PBESOL, and LDA are 3.48×10^{-4}, 5.76×10^{-4}, and 3.75×10^{-4} ps^{-1}. Table 3.5 also lists the average Umklapp scattering rate (AUSR) and average isotope scattering rate (AISR) at the same temperature. We select this temperature as an example since it can display the phonon hydrodynamics regime clearly at an extended range of characteristic lengths ($>10^3$ – $\sim10^6$ nm). ANSR is much higher than AUSR for all three pseudopotentials, which indicates that phonon hydrodynamic can exist at this temperature. The average phonon scattering rate (APSR) is the sum of ANSR and AUSR. As we discussed, both sodium and fluorine elements have naturally unique isotopes; therefore, the AISR for NaF at any temperature equals zero. For each temperature, the average boundary scattering rate (ABSR) can be calculated at a given characteristic length.

Table 3.5: Average Phonon Scattering Rate – APSR (ps^{-1}), Average Normal Scattering Rate – ANSR (ps^{-1}), Average Umklapp Scattering Rate – AUSR (ps^{-1}), and Average Isotope Scattering Rate – AISR (ps^{-1}) for NaF at T = 20 K.

	PBE	PBESOL	LDA
APSR	3.58×10^{-4}	5.83×10^{-4}	3.78×10^{-4}
ANSR	3.48×10^{-4}	5.76×10^{-4}	3.75×10^{-4}
AUSR	0.10×10^{-4}	0.07×10^{-4}	0.03×10^{-4}
AISR	0.00	0.00	0.00

Calculations at different temperatures and characteristic lengths were performed to probe the three different transport regimes. From Figure 3.5 (a), the hydrodynamics window is located between 2 K and 15.5 K for PBE, between 2 K and 16 K for PBESOL, and between 2 K and 17.2 K for LDA at L = 8.3 mm, which satisfies the experimental value [3]. Figures 3.5 (b) and (c) show the hydrodynamics windows at L = 10 μm and L = 10 nm, respectively. Figure 3.5 (d) shows the three phonon thermal transport regimes (ballistic, hydrodynamics, and diffusive) in a temperature range of (10 – 80 K) and a characteristic length of (10^2 – 10^8 nm). In these ranges, we expect to observe the phonon hydrodynamics regime.

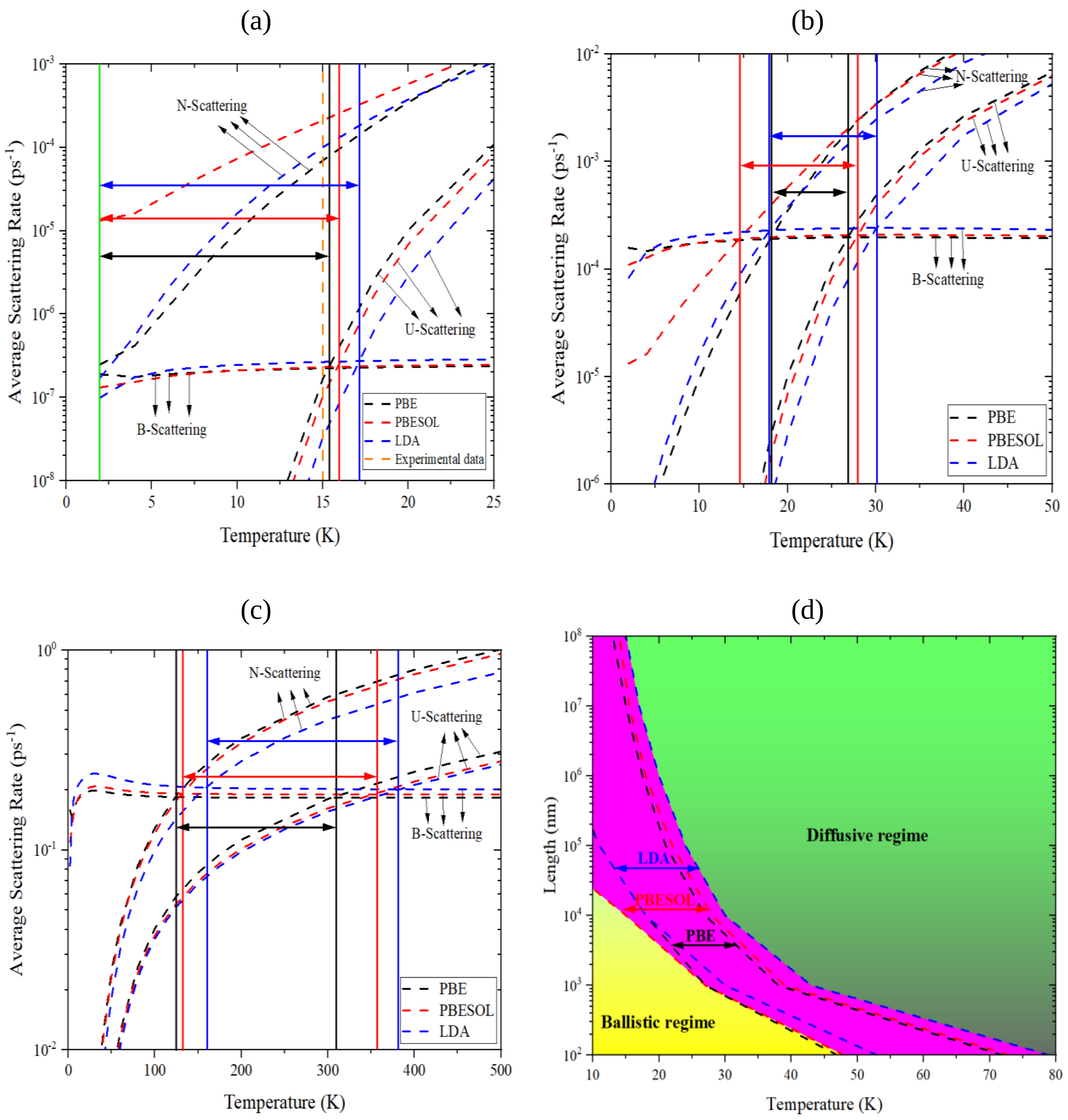

Figure 3.5: Phonon hydrodynamics windows for NaF. Calculations were done with PBE (black dashed lines), PBESOL (red dashed lines), and LDA (blue dashed lines). Double arrow lines show the hydrodynamics range for each pseudopotential. (a) At *L* = 8.3 mm. The experimental value [3] is shown as a dashed vertical orange line. The vertical green solid line means that the hydrodynamics range for all three pseudopotentials starts at the same temperature, which is at 2 K in this case. (b) At *L* = 10 µm. (c) At *L* = 10 nm. (d) Thermal transport regimes: hydrodynamics regime (pink), ballistic regime (yellow), and diffusive regime (green).

3.1.3 Phonon Hydrodynamics in Lithium Fluoride (LiF)

As LiF shares the same crystal symmetry as NaF, the presented phonon dispersion relations of LiF follow the symmetry directions as NaF. The calculated longitudinal optical mode (LO) values using LDA functional match almost with Ref.[109], while the calculated transverse optical modes (TO) values using PBESOL functional are in good agreement with the measured value of the same reference. From the dispersion relations of LiF, the transverse optical modes (TO_1, TO_2) are doubly degenerate at the gamma point due to high- symmetry in the Brillouin zone. From the LDA functional dispersion curves, the longitudinal optical mode (LO) of LiF reaches a frequency of ~ 20 THz at the gamma point, a greater value than the LO mode's frequency of NaF (~ 11.7 THz) using the PBE functional. For a given frequency, there are a number of phonon modes that may share that frequency, which is described by the phonon density of states (PDOS), as shown in Figure 3.6.

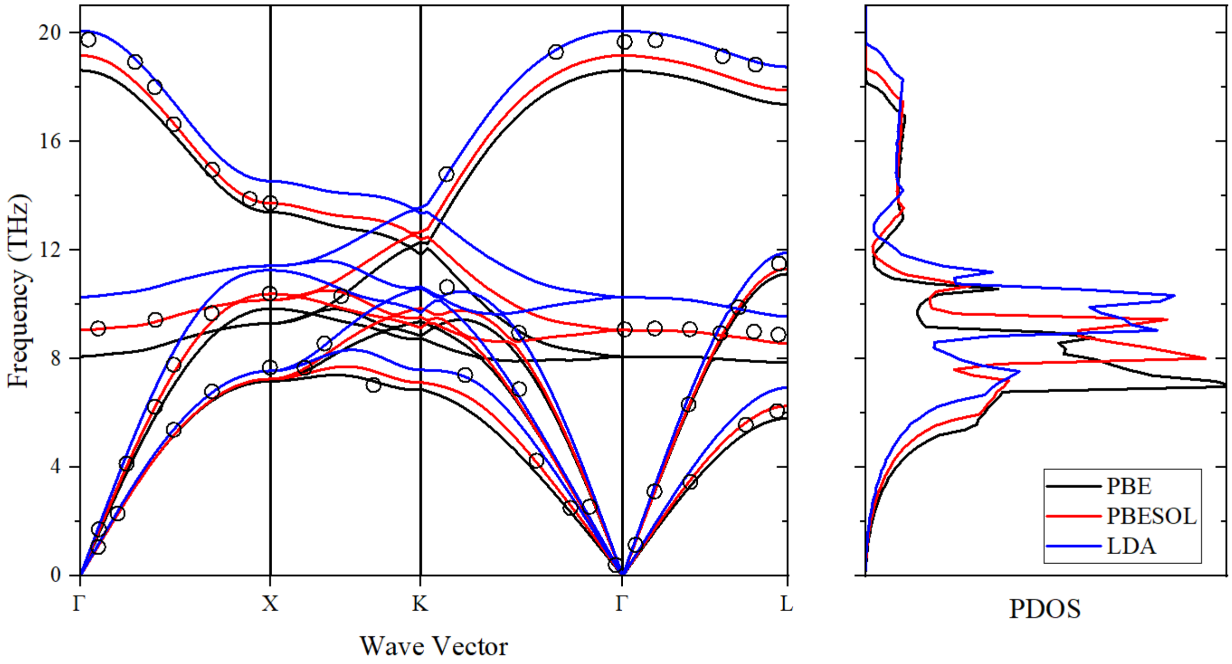

Figure 3.6: Calculated phonon dispersion (left) and phonon density of states (right) for LiF. Calculations were done with PBE (black solid lines), PBESOL (red solid lines), and LDA (blue solid lines). Black circles are the measured data from Ref.[109].

Table 3.6: Lattice constant *a* (Å), dielectric constant ε, Born effective charge Z^*, phonon frequencies at gamma ω (THz), and band gap E_g (eV) of calculated, other theoretical data, and experimental data for LiF.

	PBE	PBESOL	LDA	Other theoretical data	Experiments
a	4.07	4.01	3.91	3.886[a1], 4.005[a2], 4.002[b1], 4.103[b2], 4.02[c], 4.07[d]	4.02[e], 3.99[f]
ε	2.04	2.08	2.11	2.04[b], 2.19[g]	1.93[h]
Z^*	1.05	1.05	1.04	1.03[b], 1.06[d], 0.998[i]	-
ω_{LO}	18.63	19.18	20.09	19.89[b], 19.92[d],	19.70[j]
ω_{TO}	8.09	9.06	10.28	10.61[b], 10.29[d],	9.15[j]
E_g	8.82	9.04	9.64	8.727[d], 7.64[k1], 9.15[k2], 8.7[l]	13.6[m], 14.2[n]

[a1] Ref.[110], calculated using LDA. [a2] Ref.[110], calculated using GGA. [b] Ref.[83]. [b1] Ref.[83], calculated using LDA. [b2] Ref.[83], calculated using GGA. [c] Ref.[90]. [d] Ref.[111]. [e] Ref.[112]. [f] Ref.[113]. [g] Ref.[114]. [h] Ref.[93]. [i] Ref.[94]. [j] Ref.[109]. [k1] Ref.[115], calculated using LDA. [k2] Ref.[115], calculated using PBE. [l] Ref.[116], calculated using LDA. [m] Ref.[117]. [n] Ref.[118].

In order to obtain the lowest calculated electronic energy for PBE, PBESOL, and LDA, the lattice constant (*a*) was adjusted by relaxing the LiF structure. The calculated lattice constant for PBE (a_{PBE} = 4.07 Å) is greater than the experimental value (a_{exp} = 4.02 Å) that was found from the typical incident angular scan in the {100} direction [112], while the calculated lattice constants for PBESOL (a_{PBESOL} = 4.01 Å) and LDA (a_{LDA} = 3.91 Å) are smaller compared to the experimental value. Like in the case of NaF, the LO-TO splitting value is determined based on the Born effective charge (Z^*) calculation. The calculated Z^* for PBE and PBESOL was computed to be 1.05 and -1.05 for Li and F elements, respectively, in the atomic unit, and using LDA was found to be 1.04 and -1.04 for Li and F elements, respectively. From Table 3.6, the frequencies for the LO-TO splitting ($\omega_{\text{LO}} - \omega_{\text{TO}}$) at the gamma point are 10.53, 10.12, and 9.81 THz for PBE, PBESOL, and LDA, respectively, which are in good agreement with the experimental value (ω_{exp} = 10.55 THz) [109]. The greatest band gap value of LiF was obtained by LDA method (E_g = 9.64 eV,) yet it is less than the experimental values with an error of ~ 41% [117], [118]. However, the calculated value for the valence bandwidth using LDA is 3.5 eV, which is identical to the measured bandwidth of 3.5 eV in Ref.[119].

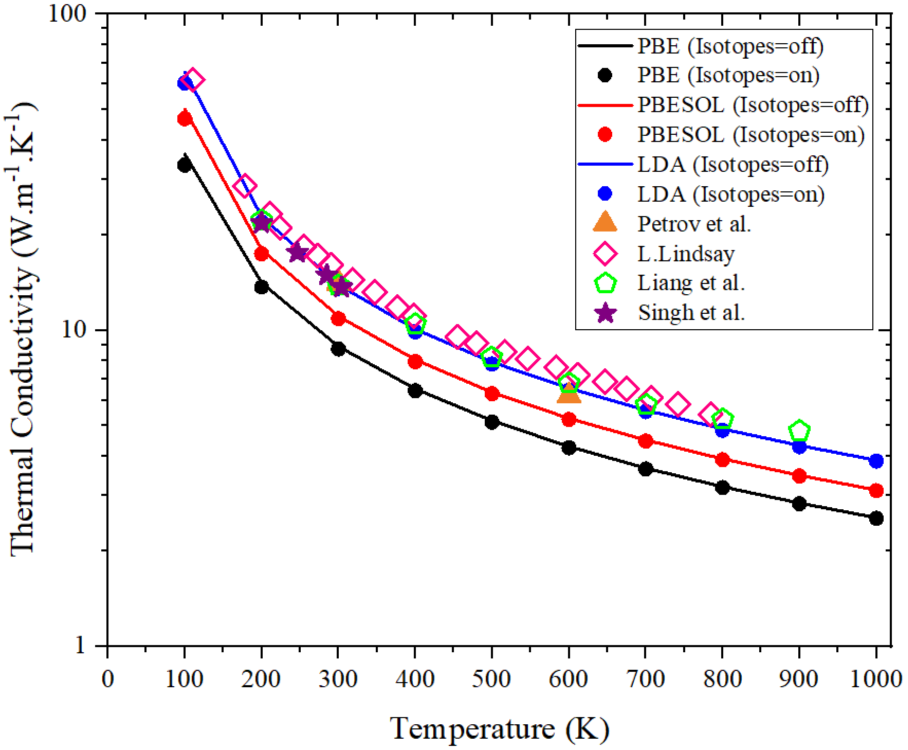

Figure 3.7: Calculated lattice thermal conductivity for LiF. Calculations were done with PBE (black solid line), PBESOL (red solid line), and LDA (blue solid line). Calculations show the effect of the isotopes on the thermal conductivity: PBE (black circles), PBESOL (red circles), and LDA (blue circles). Experimental data: Ref.[120] (orange triangles). Theoretical data: Ref.[110] (pink diamonds), Ref.[83] (green pentagons), Ref.[121] (purple stars).

The effect of isotopes on the thermal conductivity calculations for LiF is seen in Figure 3.7. It shows that the difference between the thermal conductivity values of pure LiF and impure LiF (with isotopes) is quite small (< 3 %). The calculated thermal conductivity for pure LiF using LDA method (k = 13.91 W.m^{-1}.K^{-1}) at room temperature is close to the measurable value ($k_{\exp}$ = 14.09 W.m^{-1}.K^{-1}) by Petrov *et al.*[120] with an error of 1.28 %, whereas the calculated thermal conductivity, including the isotopes, is 13.56 W.m^{-1}.K^{-1} with an error of 3.76 %. Furthermore, the percentage errors of calculated specific heat (c_p = 1.55 kJ.kg^{-1}.K^{-1}), average Grüneisen parameter ($\bar{\gamma}$ = 1.54), and density (ρ = 2.88 g.cm^{-3}) at room temperature using LDA method for pure LiF are 0.65, 3.14, and 10.77 %, respectively, compared to experimental results [101], [122], [123].

Table 3.7: Thermal conductivity k ($W.m^{-1}.K^{-1}$), specific heat c_p ($kJ.kg^{-1}.K^{-1}$), average Grüneisen parameter $\bar{\gamma}$, and density ρ ($g.cm^{-3}$) of calculated, other theoretical data, and experimental data for LiF at room temperature.

	PBE	PBESOL	LDA	Other theoretical data	Experiments
k	8.88	11.07	13.91	14.59[a1],22.42[a2] 13.89[b1], 13.48[b2], 14.80[c], 13.60[d]	14.09[e]
c_p	1.62	1.59	1.55	1.62[f]	1.54[f]
$\bar{\gamma}$	2.08	1.88	1.54	1.24[b1], 1.36[b2]	1.59[g]
ρ	2.56	2.67	2.88	-	2.60[h]

[a1] Ref.[110], calculated using a_0 = 3.894 Å. [a2] Ref.[110], calculated using a(300 K) = 4.004 Å. [b1] Ref.[83], calculated using a_0 = 4.002 Å. [b2] Ref.[83], calculated using a(300 K) = 4.03 Å. [c] Ref.[124]. [d] Ref.[121]. [e] Ref.[120]. [f] Ref.[101]. [g] Ref.[122], given at T = 323.15 K. [h] Ref.[123].

The calculated bulk modulus and elastic constants of LiF are shown in Table 3.8. There are four conditions for the mechanical stability of the elastic constants in cubic crystals, which are: $C_{11} > 0$, $C_{44} > 0$, $C_{11} - C_{12} > 0$, and $C_{11} + 2C_{12} > 0$ [111]. Our elastic constants values for fluoride materials (NaF and LiF) satisfy all these conditions. In contrast, comparing theoretical elastic constants with experiments is challenging because of the uncertainties in measuring C_{12}, where its value is a linear combination of elastic constants with the crystal in the {110} direction, whereas C_{11} and C_{44} values can be measured directly by ultrasonic techniques [125]. Nevertheless, our C_{12} value (C_{12} = 50.61 GPA) with LDA agrees with the experimental value of 47.4 GPa [106], with an error of 6.75 %.

Table 3.8: Bulk modulus B (GPa) and elastic constants C_{ij} (GPa) of calculated, other theoretical data, and experimental data for LiF.

	PBE	PBESOL	LDA	Other theoretical data	Experiments
B	67.17	72.55	86.78	67.71[a1], 73.59 [a2], 72.99[b1], 70.53[b2], 87.1125[c], 76.1[d]	76.9[e]
C_{11}	109.45	126.71	143.12	153.15[b], 129.1[d]	135.8[e]
C_{12}	46.03	45.48	50.61	45.62[b], 49.5[d]	47.4[e]
C_{44}	60.32	61.91	68.07	55.08[b], 49.5[d]	68.7[e]

[a1] Ref.[83], calculated using GGA, [a2] Ref.[83], calculated using LDA. [b] Ref.[111]. [b1] Ref.[111], calculated using Birch-Murnaghan EOS. [b2] Ref.[111], calculated using Vinet EOS. [c] Ref.[107]. [d] Ref.[125]. [e] Ref.[106].

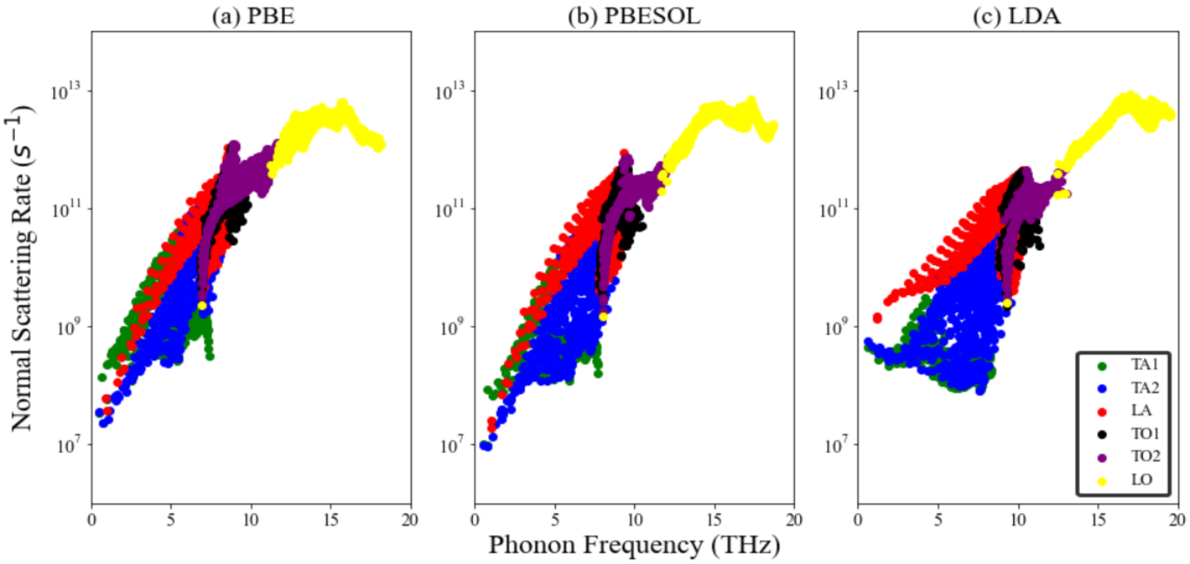

Figure 3.8: Normal scattering rates for LiF as a function of phonon frequency at T = 20 K using: (a) PBE, (b) PBESOL, and (c) LDA methods. Colorful circles denote phonon branches. The green, blue, and red circles are the acoustic phonons modes (TA_1, TA_2, LA), whereas the black, purple, and yellow circles are the optical modes (TO_1, TO_2, LO).

The normal scattering rates for LiF using different pseudopotentials at T = 20 K is shown in Figure 3.8. As listed in Table 3.9, AUSR has a negligible value compared to ANSR at T = 20 K. The phonon hydrodynamics windows of LiF at various characteristic lengths are shown in Figures 3.9 (a), (b), and (c), respectively. In comparison to NaF, LiF has a broader phonon hydrodynamics range, as illustrated in Figure 3.9 (d).

Table 3.9: Average Phonon Scattering Rate – APSR (ps^{-1}), Average Normal Scattering Rate – ANSR (ps^{-1}), Average Umklapp Scattering Rate – AUSR (ps^{-1}), and Average Isotope Scattering Rate – AISR (ps^{-1}) for LiF at T = 20 K.

	PBE	PBESOL	LDA
APSR	4.87×10^{-4}	1.66×10^{-4}	6.77×10^{-4}
ANSR	4.82×10^{-4}	1.65×10^{-4}	6.76×10^{-4}
AUSR	0.05×10^{-4}	0.01×10^{-4}	0.01×10^{-4}
AISR	1.36×10^{-4}	0.75×10^{-4}	0.48×10^{-4}

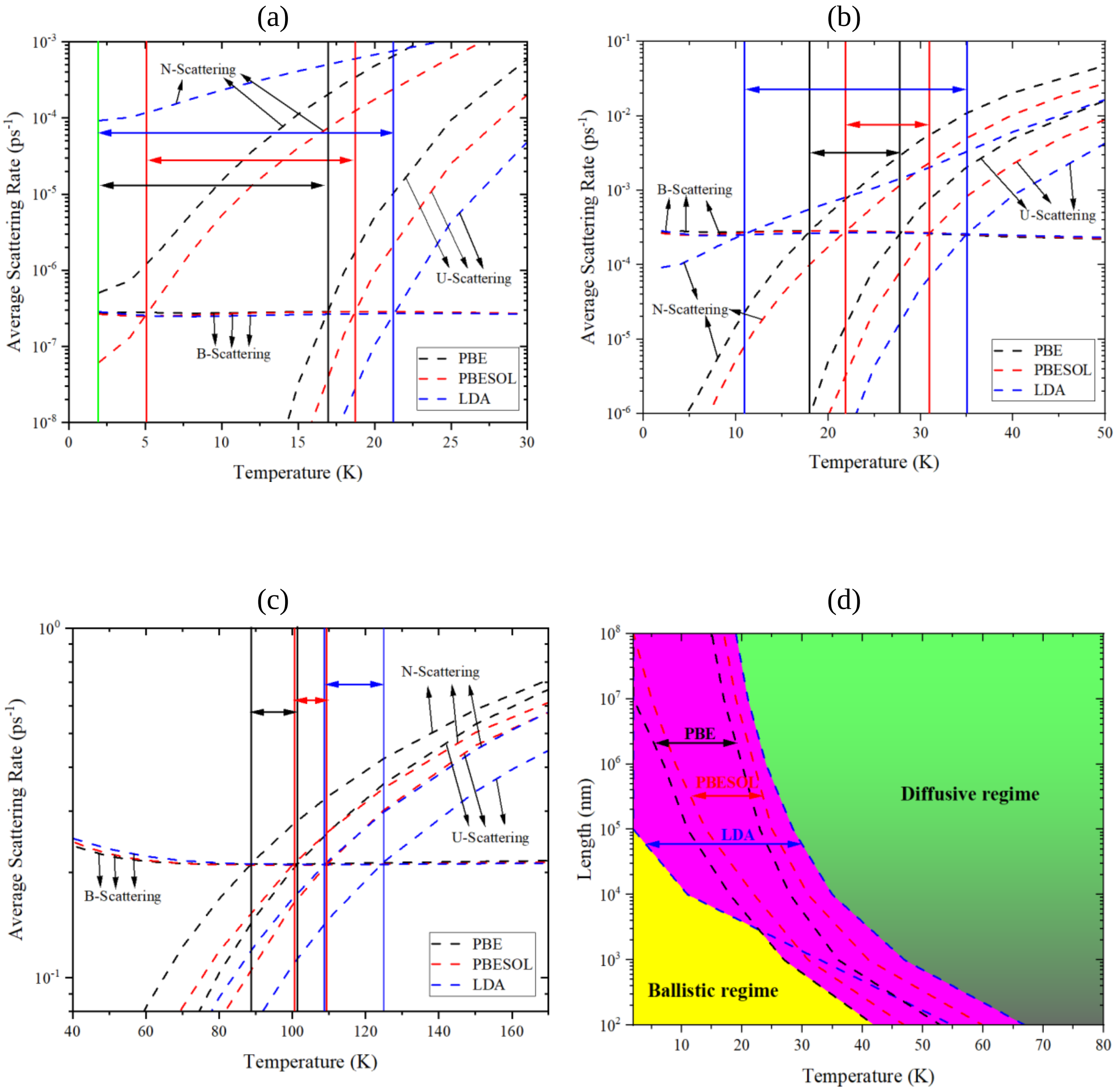

Figure 3.9: Phonon hydrodynamics windows for LiF. Calculations were done with PBE (black dashed lines), PBESOL (red dashed lines), and LDA (blue dashed lines). Double arrow lines show the hydrodynamics range for each pseudopotential. (a) At *L* = 10 mm. The vertical green solid line means that the hydrodynamics range for all three pseudopotentials starts at the same temperature, which is at 2 K in this case. (b) At *L* = 10 μm. (c) At *L* = 10 nm. (d) Thermal transport regimes: hydrodynamics regime (pink), ballistic regime (yellow), and diffusive regime (green).

3.1.4 Phonon Hydrodynamics in Lithium Hydride (LiH)

The calculated phonon dispersion of LiH along the high-symmetry directions is plotted in Figure 3.10. The phonon dispersion curves of alkali hydrides (LiH, NaH) are characterized by a gap existing between the acoustic and optical modes. The acoustic – optical (*a-o*) gap happens because of the mass variation between the component elements [110], [126]. The three-phonon scattering processes play a role in understanding the interactions between the acoustic and optical modes. The three-optical scattering processes (*ooo*) in LiH is forbidden due to energy conservation. The bunching of the acoustic branches can be calculated at the *X* point through $(\omega_{LA} - \omega_{TA})/\ \omega_{LA}$. This mathematical relation gives values of 0.24, 0.25, and 0.26 for PBE, PBESOL, and LDA, respectively, which is in good accordance with the calculated value of 0.23 [110]. Also, this results in values of 0.26 and 0.24 for LiF, and NaH, respectively, but NaF has a greater value of 0.43, indicating an effect of (*aaa*) scattering. For LiH, the dispersion data using PBE functional is well-consistent with Ref.[127]. It is noted that TO_2 breaks up from TO_1 and degenerates with LO at the *K* wave vector.

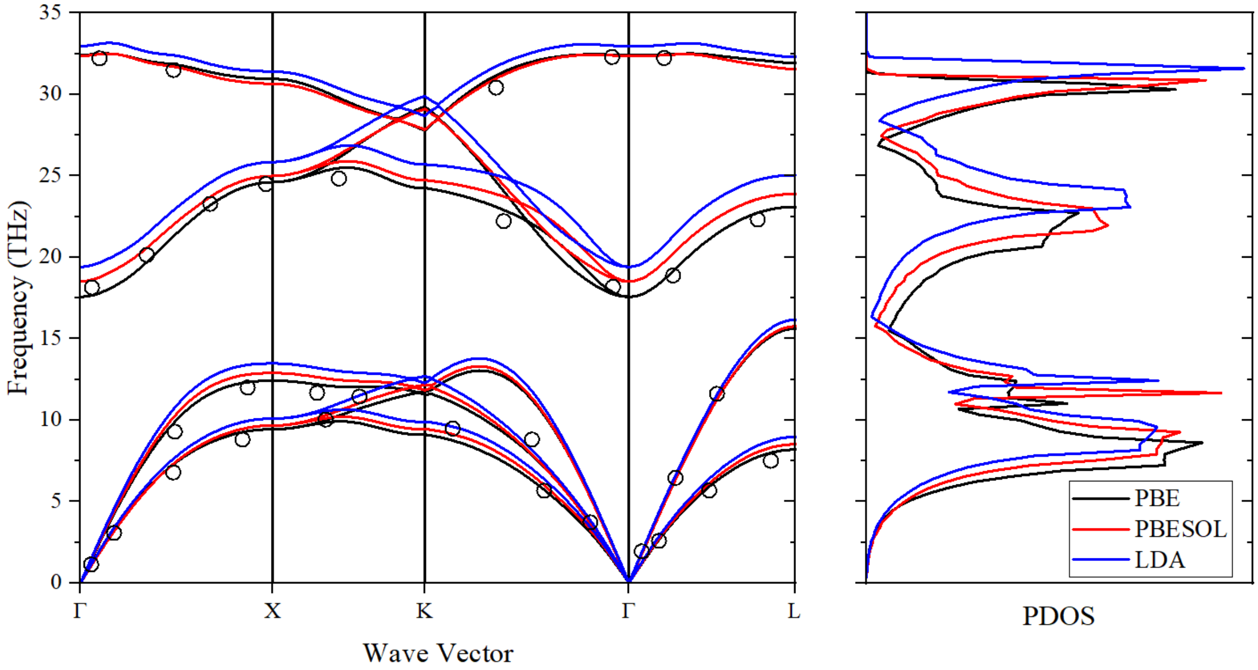

Figure 3.10: Calculated phonon dispersion (left) and phonon density of states (right) for LiH. Calculations were done with PBE (black solid lines), PBESOL (red solid lines), and LDA (blue solid lines). Black circles are the measured data from Ref.[127].

For LiH, the calculated lattice constants using PBE, PBESOL, and LDA methods (a_{PBE} = 4.01 Å, a_{PBESOL} = 3.98 Å, and a_{LDA} = 3.91 Å) are all in close agreement with the experimental values (a_{exp1} = 4.069 Å [127] and a_{exp2} = 4.083 Å [128]) with an error of less than 5 %. The experimental born effective charge of LiH ($Z^*_{\mathrm{exp1}} = 0.991$) was computed by Shukla [94] using experimental values of the Szigeti charge 'Z_s' and the high-frequency dielectric constant 'ε_∞' from Ref.[129] and applying the mathematical relation of $Z^* = [(\varepsilon_\infty+2)/3]Z_s$, which is described in Ref.[130]. This computed value and the other experimental value ($Z^*_{\mathrm{exp2}} = 1.11$ [131]) agree with our results. From Table 3.10, the frequency of LO is much higher than TO due to the strong depolarization field in LiH. The LO frequency at the gamma point can also be obtained from the Lyddane-Sachs-Teller (LST) relation ($\omega^2_{\mathrm{LO}} / \omega^2_{\mathrm{TO}} = \varepsilon_0 / \varepsilon_\infty$) [132], which gives a value of 32.40 THz. ε_0 refers to the static-frequency dielectric constant. Both values from first-principles calculations and LST relation agree the experimental values [127], [129], [131], [133].

Table 3.10: Lattice constant *a* (Å), dielectric constant ε, Born effective charge Z^*, phonon frequencies at gamma ω (THz), and band gap E_g (eV) of calculated, other theoretical data, and experimental data for LiH.

	PBE	PBESOL	LDA	Other theoretical data	Experiments
a	4.01	3.98	3.91	3.947[a1],3.894[a2], 4.02[b], 3.997[c]	4.069[d], 4.083[e], 4.083[f], 4.083[g]
ε	4.39	4.70	4.99	4.34[b], 4.81[h]	3.61[e]
Z^*	1.02	1.02	1.03	1.020[c], 1.03[h], 1.046[i]	0.991[j], 1.11[h]
ω_{LO}	32.43	32.37	32.96	28.3[h]	32.21[d], 33.50[h], 33.60[j], 33.15[k]
ω_{TO}	17.56	18.52	19.41	18.1[h], 17.86[l]	18.14[d], 18.40[h], 17.76[j], 17.70[k]
E_g	2.98	2.73	2.54	3.00[b1], 2.61[b2], 4.75[b3], 2.53[l]	5.00[m], 4.92[n]

[a1] Ref.[110], calculated using GGA. [a2] Ref.[110], calculated using LDA. [b] Ref.[134]. [b1] Ref.[134], calculated using GGA. [b2] Ref.[134], calculated using LDA. [b3] Ref.[134] , calculated using GW. [c] Ref.[135]. [d] Ref.[127]. [e] Ref.[128]. [f] Ref.[136]. [g] Ref.[137]. [h] Ref.[131]. [i] Ref.[94]. [j] Ref.[129]. [k] Ref.[133]. [l] Ref.[138]. [m] Ref.[139]. [n] Ref.[140].

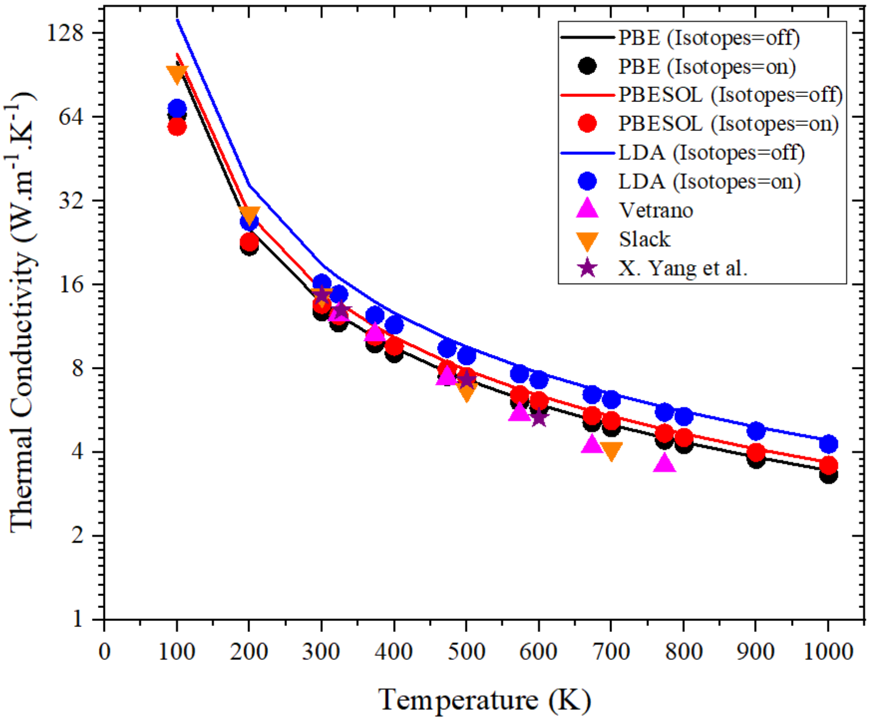

Figure 3.11: Calculated lattice thermal conductivity for LiH. Calculations were done with PBE (black solid line), PBESOL (red solid line), and LDA (blue solid line). Calculations show the effect of the isotopes on the thermal conductivity: PBE (black circles), PBESOL (red circles), and LDA (blue circles). Experimental data: Ref.[141] (pink up triangles), Ref.[142] (orange down triangles). Theoretical data: Ref.[135] (purple stars).

Several experiments and theoretical calculations have been performed to determine the thermal conductivity of LiH [110], [135], [141], [142], as shown in Figure 3.11. Vetrano [141] measured the thermal conductivity of LiH at T = 327 K (k_{exp} = 12.47 W.m^{-1}.K^{-1}). Referring to Table 3.11, previous theoretical studies yielded higher thermal conductivity values at the same temperature [110], [135]. Our calculations using PBE are in good agreement with Vatrano's value if the effect of isotopes is excluded. Including isotopes in our calculations leads to an increase in the error percentage to 6 %. Specific heat value (c_p = 3.69 kJ.kg^{-1}.K^{-1}) with PBE is also in good agreement with the experiment value (c_p = 3.64 kJ.kg^{-1}.K^{-1}) [143]. LiH has relatively a low density ($\rho \approx$ 0.775 g.cm^{-3} by experiments [128], [129], [136]) and, again, our calculated density values using PBE agree with these experiments.

Table 3.11: Thermal conductivity k (W.m^{-1}.K^{-1}), specific heat c_p (kJ.kg^{-1}.K^{-1}), average Grüneisen parameter $\bar{\gamma}$, and density ρ (g.cm^{-3}) of calculated, other theoretical data, and experimental data for LiH at room temperature.

	PBE	PBESOL	LDA	Other theoretical data	Experiments
k[*]	12.47	13.76	16.98	25.51[a1], 23.00[a2], 12.98[b]	12.47[c]
c_p	3.69	3.57	3.45	-	3.64[d]
$\bar{\gamma}$	1.64	1.57	1.42	1.64[e]	1.28[f]
ρ	0.81	0.84	0.88	-	0.775[g], 0.775[h], 0.7754[i]

[*] Thermal conductivity values were obtained at T = 327 K. [a1] Ref.[110], calculated using a_0 = 3.894 Å. [a2] Ref.[110], calculated using a(300 K) = 4.004 Å. [b] Ref.[135]. [c] Ref.[141]. [d] Ref.[143]. [e] Ref.[144]. [f] Ref.[145]. [g] Ref.[128]. [h] Ref.[136]. [i] Ref.[129].

The experimental and first-principles data for the elastic constants of LiH is shown in Table 3.12. An important mechanical parameter of elastic properties for alkali hydrides (LiH, NaH) is the elastic anisotropy factor 'AF'. The degree of anisotropy is based on the magnitude of the directional dependence of the properties [146]. AF = 2C$_{44}$/(C$_{11}$-C$_{12}$), where AF = 1 for an elastic isotropic medium [147]. AF values of LiH with PBE, PBESOL, and LDA are 1.65, 1.29, and 1.21, respectively. Like LiH, LiF also has a large AF value (AF = 1.90 using PBE). These values indicate a strong elastic anisotropy in these materials. One of the effects of elastic anisotropy is the phenomenon of long-wavelength phonon focusing [148]. At high AF, it is expected a strong phonon focusing will takes place even at the long-wavelength elastic limit. It has been suggested that phonon focusing is connected to the phonon hydrodynamics in fluorides and alkali hydrides because all crystals may exhibit phonon focusing at the same low temperatures where phonon hydrodynamics is observed [149].

Table 3.12: Bulk modulus B (GPa) and elastic constants C$_{ij}$ (GPa) of calculated, other theoretical data, and experimental data for LiH.

	PBE	PBESOL	LDA	Other theoretical data	Experiments
B	34.24	37.06	40.60	34.03[a1], 41.33[a2], 36.6[b], 36.07[c]	34.24[b], 31.7[d]
C$_{11}$	73.06	85.34	95.36	78.9[e], 79.8[f], 65.82[g]	74.10[f], 67.20[h]
C$_{12}$	14.03	10.42	10.22	44.3[e], 45.9[f], 15.44[g]	14.20[f], 14.93[h]
C$_{44}$	48.62	48.31	51.48	44.1[e], 45.7[f], 42.91[g]	48.40[f], 46.37[h]

[a1] Ref.[150], calculated using PBE. [a2] Ref.[150], calculated using LDA. [b] Ref.[151]. [c] Ref.[152]. [d] Ref.[153]. [e] Ref.[154]. [f] Ref.[155] . [g] Ref.[156]. [h] Ref.[145]

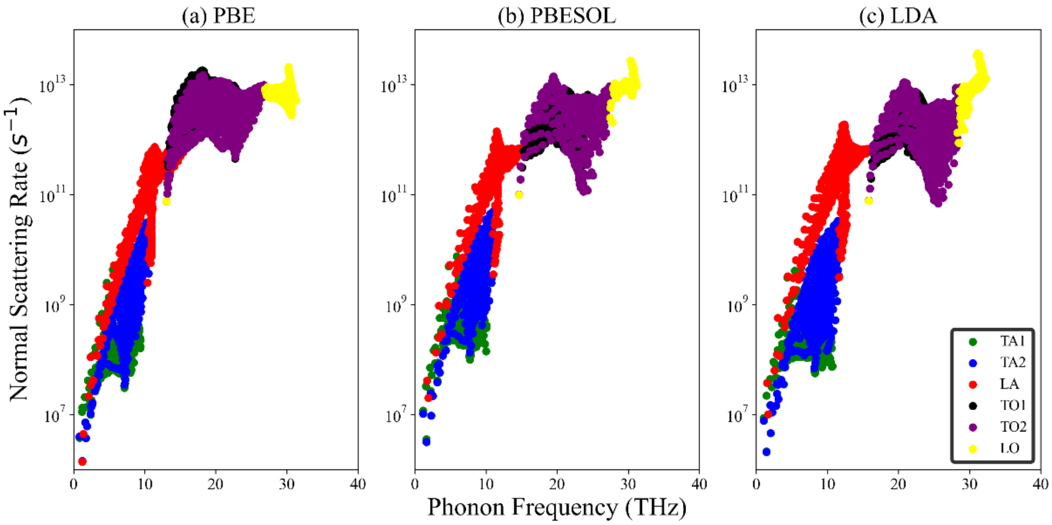

Figure 3.12: Normal scattering rates for LiH as a function of phonon frequency at $T = 20$ K using: (a) PBE, (b) PBESOL, and (c) LDA methods. Colorful circles denote phonon branches. The green, blue, and red circles are the acoustic phonons modes (TA_1, TA_2, LA), whereas the black, purple, and yellow circles are the optical modes (TO_1, TO_2, LO).

In Figure 3.12, the Normal scattering rates for LiH show the variations between the acoustic and optical branches. As seen in Table 3.13, the value of AUSR at $T = 20$ K is less than 1×10^{-7} ps^{-1}, which is much less than ANSR. The phonon hydrodynamics windows of LiH, as shown in Figures 3.13 (a), (b), and (c), emerges at $T < 30$ K for $L = 10$ mm, $30 < T < 50$ K for $L = 10$ μm, and $110 < T < 160$ K for $L = 10$ nm. These figures produce the phonon thermal transports (Figure 3.13 (d)).

Table 3.13: Average Phonon Scattering Rate – APSR (ps^{-1}), Average Normal Scattering Rate – ANSR (ps^{-1}), Average Umklapp Scattering Rate – AUSR (ps^{-1}), and Average Isotope Scattering Rate – AISR (ps^{-1}) for LiH at $T = 20$ K.

	PBE	PBESOL	LDA
APSR	3.06×10^{-5}	6.24×10^{-5}	4.61×10^{-5}
ANSR	3.05×10^{-5}	6.23×10^{-5}	4.60×10^{-5}
AUSR	0.01×10^{-5}	0.01×10^{-5}	0.01×10^{-5}
AISR	5.00×10^{-4}	4.01×10^{-4}	2.89×10^{-4}

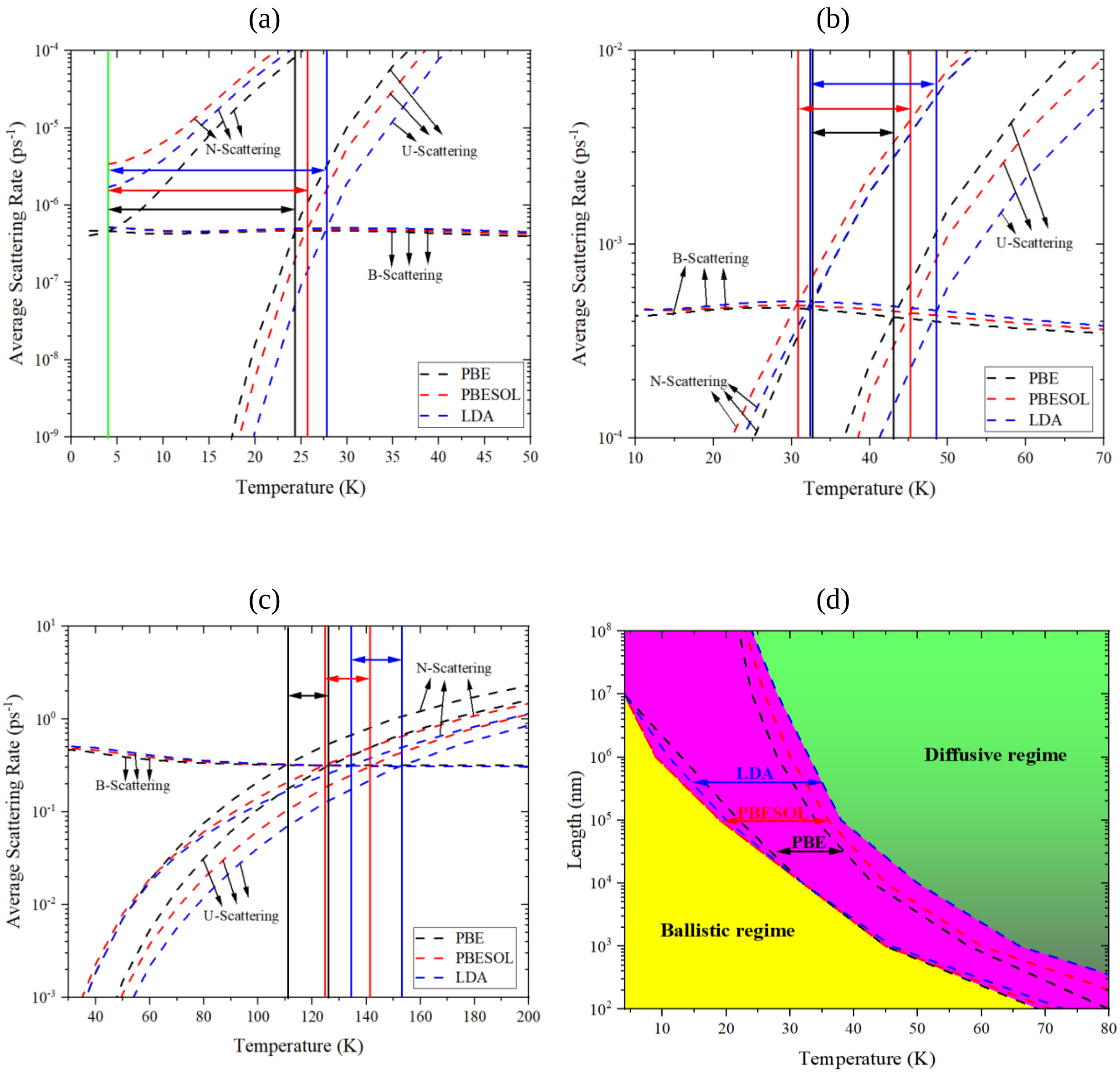

Figure 3.13: Phonon hydrodynamics windows for LiH. Calculations were done with PBE (black dashed lines), PBESOL (red dashed lines), and LDA (blue dashed lines). Double arrow lines show the hydrodynamics range for each pseudopotential. (a) At L = 10 mm. The vertical green solid line means that the hydrodynamics range for all three pseudopotentials starts at the same temperature, which is at 4 K in this case. (b) At L = 10 μm. (c) At L = 10 nm. (d) Thermal transport regimes: hydrodynamics regime (pink), ballistic regime (yellow), and diffusive regime (green).

3.1.5 Phonon Hydrodynamics in Sodium Hydride (NaH)

As shown in Figure 3.14, the calculated phonon dispersion of NaH exhibits disparately from LiH in terms of the (*a*-*o*) gap. The (*a*-*o*) gap in NaH is greater than the (*a*-*o*) gap in LiH because of the large mass difference between ‘Na’ and ‘H’ atoms in contrast to ‘Li’ and ‘H’ atoms. This gap is clearly visible in the PDOS. The calculated (*a*-*o*) gap is about 7.83, 8.27, and 9.43 THz using PBE, PBESOL, and LDA, respectively. Zhao *et al.* [157] calculated the gap value for NaH, (*a*-*o*) gap = 49.3 rad/ps ≈ 7.85 THz, close to the PBE value. The PDOS reveals that the sodium atoms provide practically all of the acoustic vibrations, whilst the hydrogen atoms are the source of the majority of the optical modes [157]. According to the PDOS diagram, the highest frequency for hydrogen atom vibrations is 26.7 THz using PBE, exactly what was found in Ref.[158].

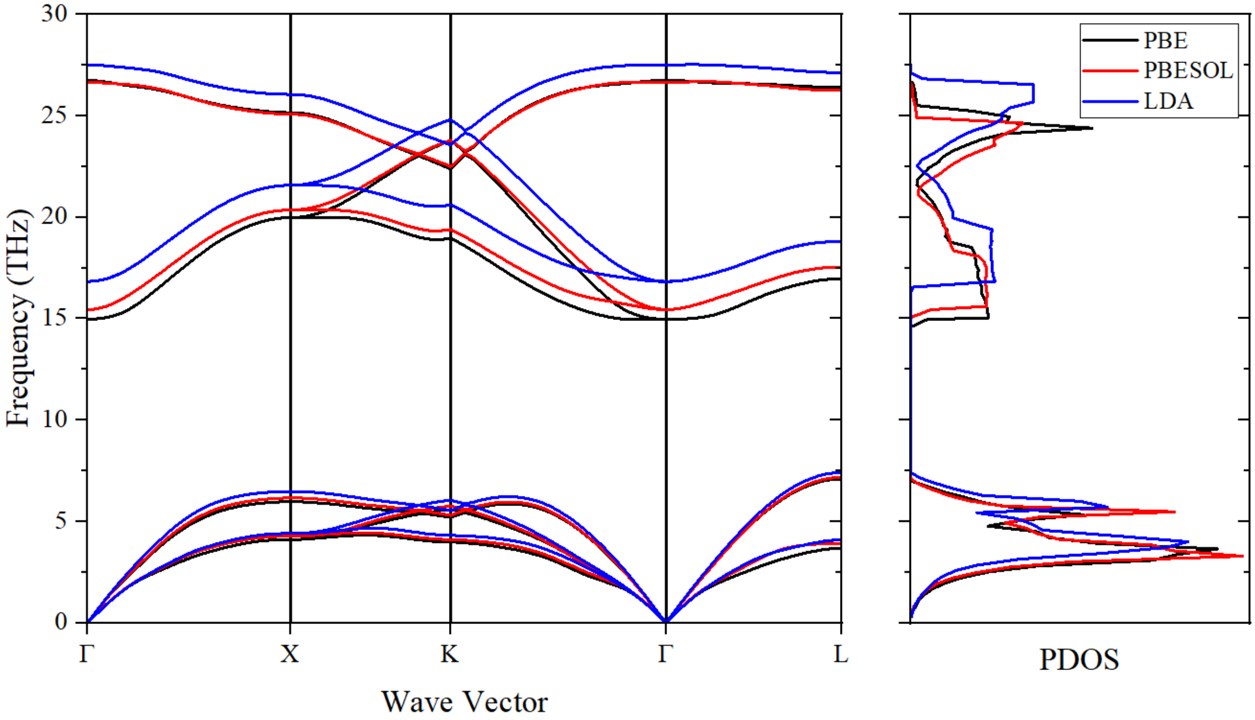

Figure 3.14: Calculated phonon dispersion (left) and phonon density of states (right) for NaH. Calculations were done with PBE (black solid lines), PBESOL (red solid lines), and LDA (blue solid lines).

Table 3.14: Lattice constant a (Å), dielectric constant ε, Born effective charge Z^*, phonon frequencies at gamma ω (THz), and band gap E_g (eV) of calculated, other theoretical data, and experimental data for NaH.

	PBE	PBESOL	LDA	Other theoretical data	Experiments
a	4.84	4.79	4.69	4.82[a], 4.83[b], 4.83[c], 4.862[d]	4.88[e]
ε	3.13	3.26	3.36	3.09[a], 3.06[c]	-
Z^*	0.97	0.96	0.95	0.96[a], 0.97[b]	-
ω_{LO}	26.75	26.65	27.52	~27.06[b]	-
ω_{TO}	14.97	15.44	16.83	16.6[f1], 13.9[f2]	-
E_g	3.76	3.61	3.55	4.90[a], 3.79[c1], 3.42[c2], 5.87[c3], 5.68[g1], 3.39[g2]	-

[a]Ref.[158]. [b]Ref.[157]. [c]Ref.[134]. [c1]Ref.[134], calculated using GGA. [c2]Ref.[134], calculated using LDA. [c3]Ref.[134], calculated using GW. [d]Ref.[159]. [e]Ref.[160]. [f1]Ref.[161], calculated using clamped-nucleus (CN) approximation. [f2]Ref.[161], calculated using quasiharmonic (QH) approximation. [g1]Ref.[162], calculated using GW. [g2]Ref.[162], calculated using LDA.

The calculated lattice constant with PBE (a_{PBE} = 4.84 Å), from Table 3.14, is the closest to the experimental value (a_{exp} = 4.88 Å) [160], where the error is < 1 %. Compared to LiH, NaH has a larger lattice parameter because bandwidths in LiH are larger than those in NaH due to the near distance of the hydrogen atoms [134]. Moreover, the two materials have different types of electronic band gaps. The gap in LiH is direct since the minimum energy gap edges between the conduction and valence are at the same κ-point in the Brillouin zone. As shown in Figure 3.15 (a), the minimum energy gap edges between the conduction and valence are at the *X* point (circled in red). However, the gap in NaH is indirect because the minimum energy gap edges between the conduction and valence are at different κ-point in the Brillouin zone. As seen in Figure 3.15 (b), the minimum energy gap edge is between the conduction band at *L* point and the valence band at *X* point (red double arrow). It is noted that the LO-TO splitting frequencies value of NaH ($\omega_{LO\text{-}TO}$ = 11.78 THz using PBE) and LiH ($\omega_{LO\text{-}TO}$ = 14.87 THz using PBE) are greater than the LO-TO splitting frequencies value of NaF ($\omega_{LO\text{-}TO}$ = 4.89 THz using PBE) and LiF ($\omega_{LO\text{-}TO}$ = 9.81 THz using LDA) at the gamma point. The large LO-TO splitting frequency values are due to strong polar phonon (creation of an oscillating electric field inside a crystal caused by phonons due to local charge polarization [48]) frequencies of hydride materials (LiH, NaH) compared to fluoride materials (NaF, LiF).

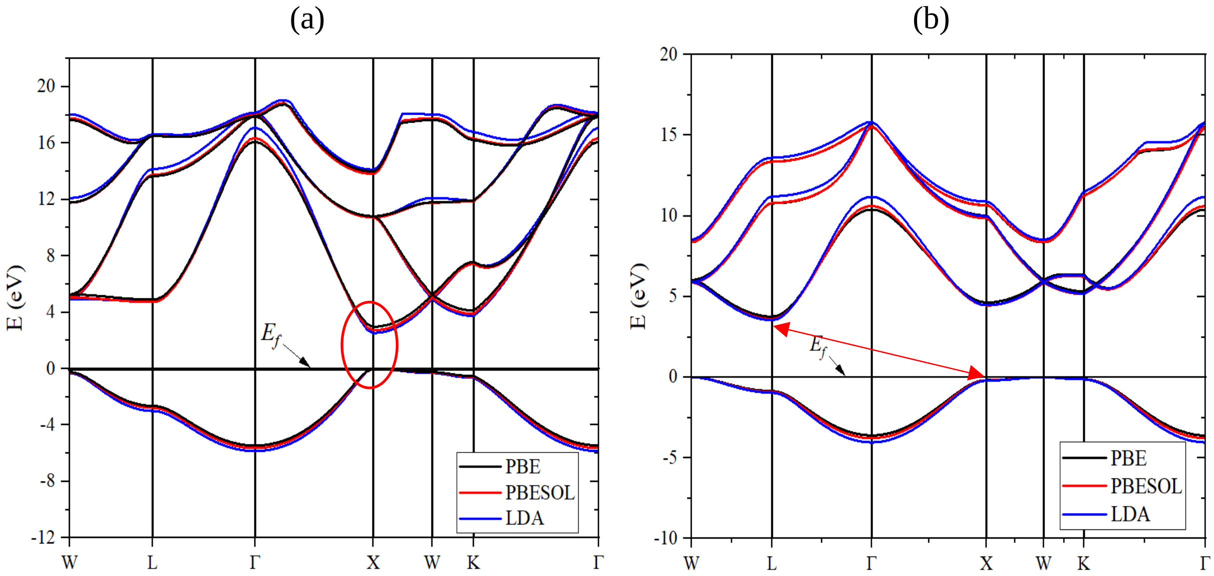

Figure 3.15: Electronic band structures of: (a) LiH. (b) NaH. Fermi energy (E_f) is set at 0 eV.

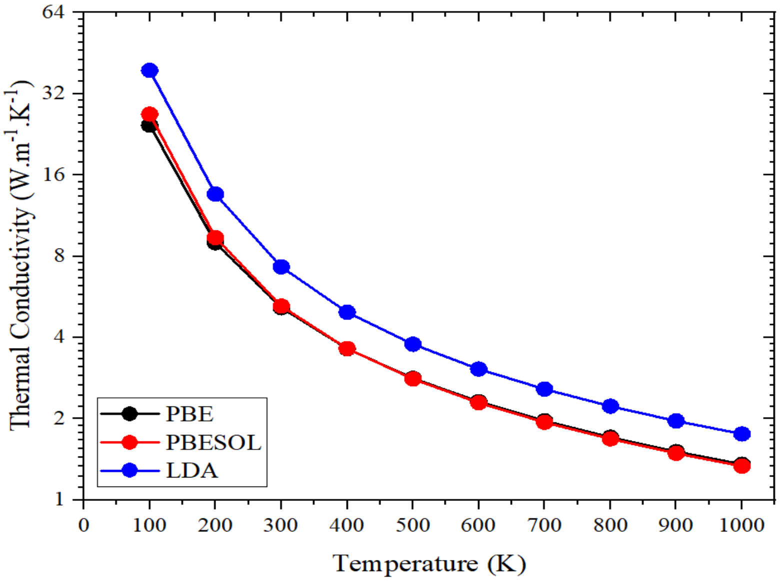

Figure 3.16: Calculated lattice thermal conductivity for NaH. Calculations were done with PBE (black circles), PBESOL (red circles), and LDA (blue circles).

The thermal conductivity of NaH at room temperature is compared with the experiment [163] (Appendix A-2) to select the appropriate second and third-order supercells and cutoff parameters. The calculated thermal conductivity values of NaH, shown in Figure 3.16, are less than LiH, NaF, and LiF. The values are between 1 and 40 W.m^{-1}. K^{-1} for temperature ranges between 100 and 1000 K. At T = 300 K, the calculated thermal conductivity equals 5.16, 5.23, and

7.30 W.m^{-1}.K^{-1} (Table 3.15) for PBE, PBESOL, and LDA, respectively, close enough to the experimental value [163]. The difference between the thermal conductivity values of PBE and PBESOL is nearly negligible.

Table 3.15: Thermal conductivity k (W.m^{-1}.K^{-1}), specific heat c_p (kJ.kg^{-1}.K^{-1}), average Grüneisen parameter $\bar{\gamma}$, and density ρ (g.cm^{-3}) of calculated, other theoretical data, and experimental data for NaH at room temperature.

	PBE	PBESOL	LDA	Other theoretical data	Experiments
k	5.16	5.23	7.30	15.41[a]	5.00[b]
c_p	1.51	1.52	1.46	-	1.52[c]
$\bar{\gamma}$	1.68	1.77	1.65	1.8[d1], 2.2[d2], 1.76[e]	-
ρ	1.41	1.44	1.54	-	1.39[f], 1.37[g]

[a]Ref.[157]. [b]Ref.[163]. [c]Ref.[164]. [d1]Ref.[161], calculated using clamped-nucleus (CN) approximation. [d2]Ref.[161], calculated using quasiharmonic (QH) approximation. [e]Ref.[144]. [f]Ref.[165]. [g]Ref.[166].

Table 3.16 presents the elastic constants of NaH. One also can take advantage of the elastic constants data to see whether the material is brittle or ductile. According to Cauchy pressure ($C_{12} - C_{44}$), if the difference is positive, the material is ductile; otherwise, it is brittle [167]. All materials (NaF, LiF, and LiH) were discussed so far are brittle (negative difference). Another criterion for checking the ductility/brittleness of materials is Pugh's modulus ratio (B/G), where G is the shear modulus [168]. The critical value of Pugh's modulus ratio is 1.75. If the ratio > 1.75, the material is ductile; otherwise, it is brittle [169]. This ratio gives 1.18, 1.17, and 1.20 for PBE, PBESOL, and LDA, respectively, indicating that LiH is brittle. Other materials, such as silicon and germanium, are brittle as well [170].

Table 3.16: Bulk modulus B (GPa) and elastic constants C_{ij} (GPa) of calculated, other theoretical data, and experimental data for NaH.

	PBE	PBESOL	LDA	Other theoretical data	Experiments
B	22.16	23.92	27.43	22.90[a], 22.93[b], 23.7[c], 27[d1], 20[d2]	19.40[e] 14.30[f]
C_{11}	43.69	47.19	55.25	42.12[b], 47.3[g]	-
C_{12}	12.89	12.29	13.52	13.06[b], 22.5[g]	-
C_{44}	22.35	22.31	24.19	22.02[b], 22.5[g]	-

[a]Ref.[171]. [b]Ref.[159]. [c]Ref.[172]. [d1]Ref.[161], calculated using clamped-nucleus (CN) approximation. [d2]Ref.[161], calculated using quasiharmonic (QH) approximation. [e]Ref.[173]. [f]Ref.[174]. [g]Ref.[154].

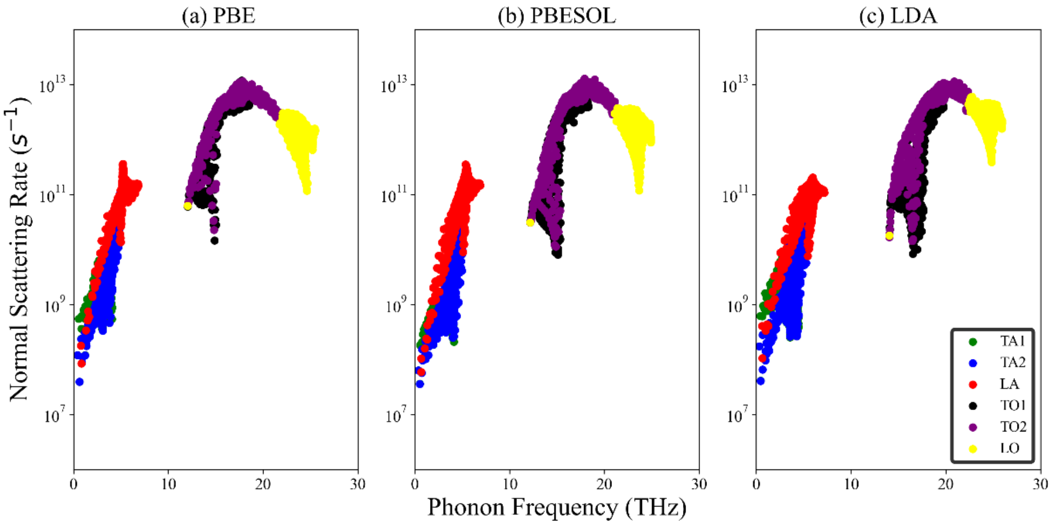

Figure 3.17: Normal scattering rates for NaH as a function of phonon frequency at T = 20 K using: (a) PBE, (b) PBESOL, and (c) LDA methods. Colorful circles denote phonon branches. The green, blue, and red circles are the acoustic phonons modes (TA_1, TA_2, LA), whereas the black, purple, and yellow circles are the optical modes (TO_1, TO_2, LO).

The large gap between the acoustic and optical branches is visible in the Normal scattering rates plot at T = 20 K (Figure 3.17). ANSR, AUSR, and AISR at T = 20 K (Table 3.17) using PBE equal 1.72×10^{-3}, 0.26×10^{-3}, and 6.97×10^{-8} ps^{-1}, respectively. The difference in magnitude between N-scattering and U-scattering curves is not as significant as compared to NaF, LiF, and LiH, as demonstrated in Figures 3.18 (a), (b), and (c), and consequently, the phonon hydrodynamics window is narrower as shown in Figure 3.18 (d).

Table 3.17: Average Phonon Scattering Rate – APSR (ps^{-1}), Average Normal Scattering Rate – ANSR (ps^{-1}), Average Umklapp Scattering Rate – AUSR (ps^{-1}), and Average Isotope Scattering Rate – AISR (ps^{-1}) for NaH at T = 20 K.

	PBE	PBESOL	LDA
APSR	1.98×10^{-3}	1.62×10^{-3}	1.79×10^{-3}
ANSR	1.72×10^{-3}	1.42×10^{-3}	1.69×10^{-3}
AUSR	0.26×10^{-3}	0.20×10^{-3}	0.10×10^{-3}
AISR	6.97×10^{-8}	1.12×10^{-7}	9.55×10^{-8}

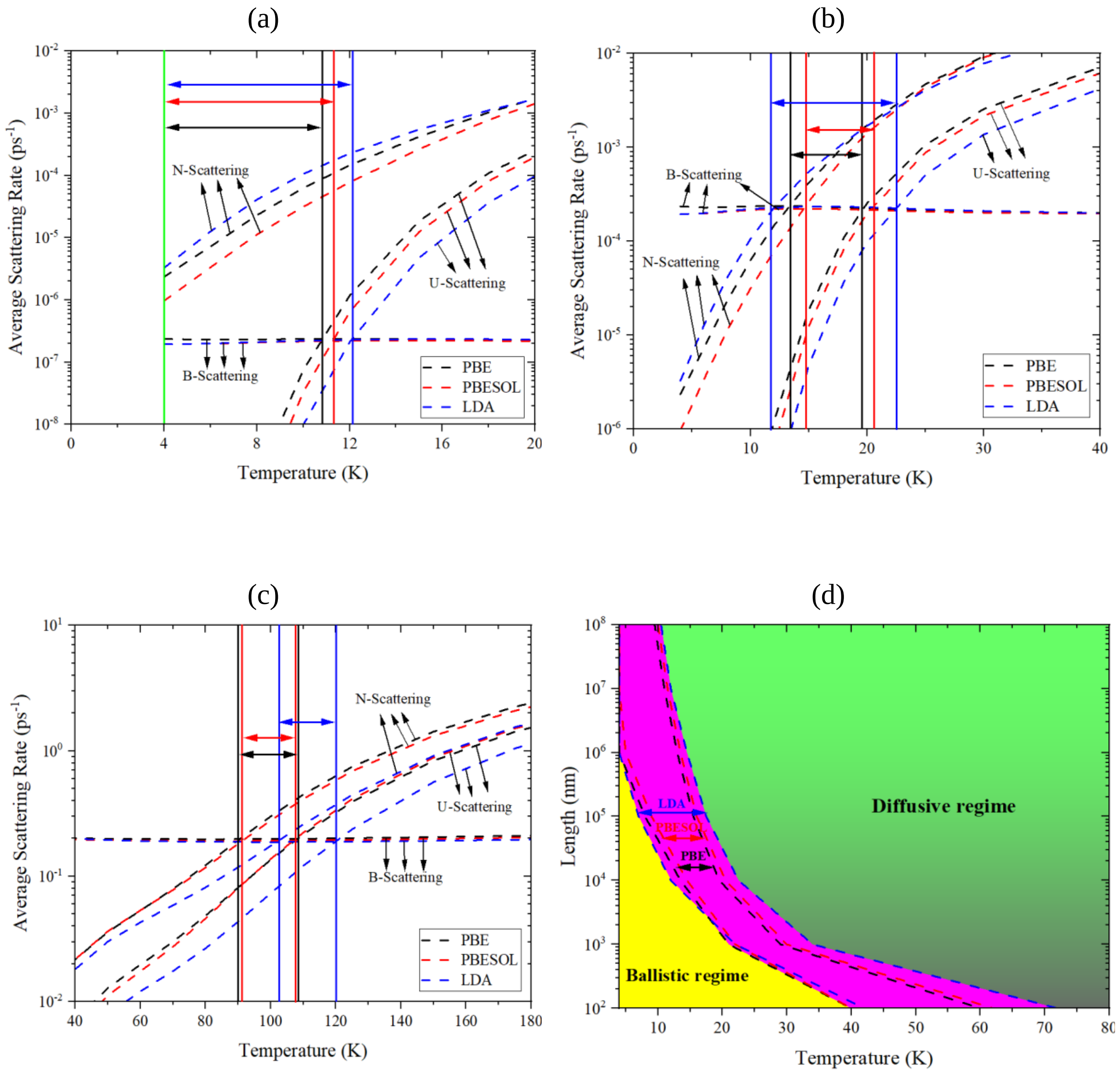

Figure 3.18: Phonon hydrodynamics windows for NaH. Calculations were done with PBE (black dashed lines), PBESOL (red dashed lines), and LDA (blue dashed lines). Double arrow lines show the hydrodynamics range for each pseudopotential. (a) At L = 10 mm. The vertical green solid line means that the hydrodynamics range for all three pseudopotentials starts at the same temperature, which is at 4 K in this case. (b) At L = 10 μm. (c) At L = 10 nm. (d) Thermal transport regimes: hydrodynamics regime (pink), ballistic regime (yellow), and diffusive regime (green).

3.1.6 Discussion – Project (1)

We selected three properties (thermal conductivity, specific heat, and bulk modulus) for which experimental values are available to show the effect of pseudopotentials (PBE, PBESOL, and LDA) on these properties, as illustrated in Figure 3.19. Each quarter represents the properties of one out of the four materials that we studied. The radius of each circle denotes the percentage error; our results do not exceed an error of 50 %. As the accuracy of the prediction increases, the marker moves closer to the center of the circle. Figure 3.19 (right plot) shows that most of our results are between 0 and 10 %. We analyzed the results and found that 75 % of the PBE results were in the range of (0 – 10 %) error, 66.67 % for PBESOL, and 41.67 % for LDA, as listed in Table 3.18. Almost 92 % of PBE results were in the range of (0 – 20 %) error. We examined the PBE also with other materials, such as silicon, germanium, and bilayer system, and found it to be the optimal pseudopotential choice. Since there is no rule for selecting an appropriate pseudopotential, we recommend comparing first-principles calculations using common pseudopotentials with the experimental works from the literature. On the other hand, the selection is to be made on a case-by-case basis. For instance, the inclusion of the spin-orbit effect (coupling/interaction) may be necessary if the knowledge of the material, particularly its magnetic nature, is scarce.

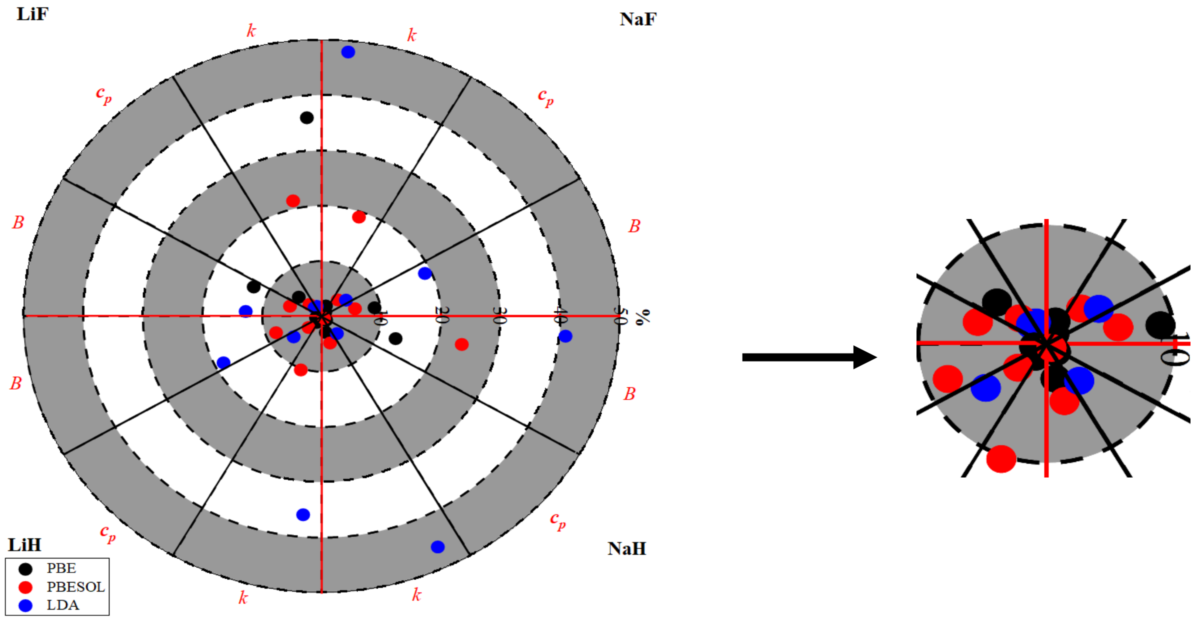

Figure 3.19: Effect of pseudopotentials on calculations of material properties (thermal conductivity, heat capacity, and bulk modulus). PBE (black circles), PBESOL (red circles), and LDA (blue circles).

Table 3.18: Percentage error of PBE, PBESOL, and LDA.

% Error	PBE	PBESOL	LDA
0 - 10	75.00 %	66.67 %	41.67 %
10 - 20	16.67 %	16.67 %	25.00 %
20 - 30	0.00 %	16.67 %	0.00 %
30 - 40	8.33 %	0.00 %	8.33 %
40 - 50	0.00 %	0.00 %	25.00 %

Excluding differences due to pseudopotential choice, differences in the hydrodynamic windows for fluorides (NaF, LiF) and alkali hydrides (LiH, NaF) are observed. This can be partially explained by examining the combined scattering rates (N-scattering + U-scattering) as a function of phonon frequency for these materials at various temperatures, as shown in Figures 3.20 (a) and (b). At T = 50 K, scattering rates for all materials are almost located between 10^8 and 10^{14} s^{-1} and between 10^9 and 10^{15} s^{-1} at T = 300 K. Here, we chose the appropriate pseudopotential for each material based on the agreement of the thermal properties of the material (e.g., thermal conductivity, specific heat, etc.) with experiments.

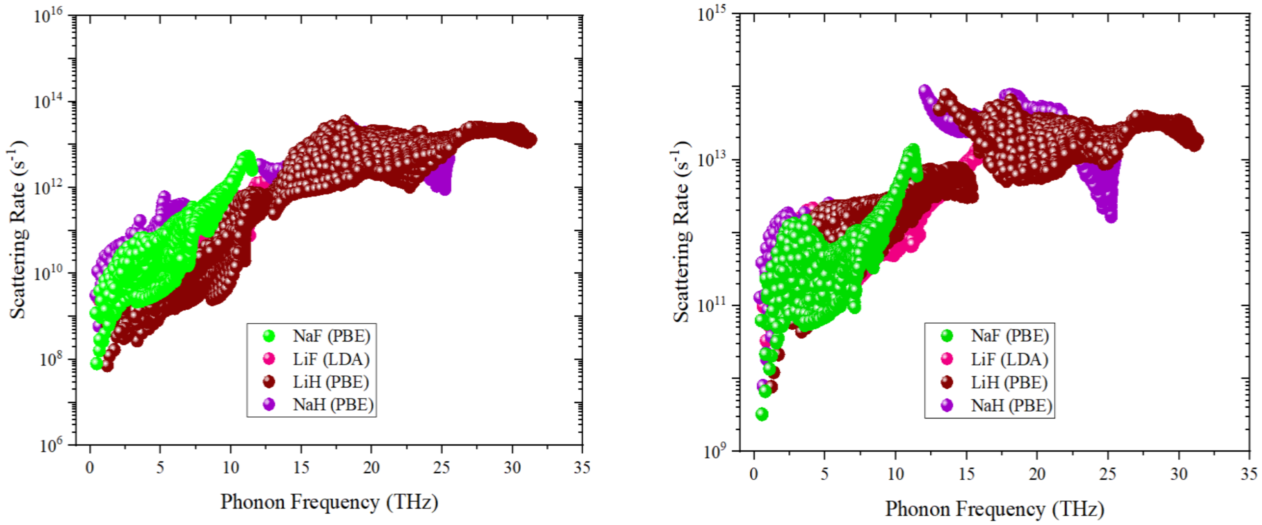
(a)

(b)

Figure 3.20: Phonon scattering rate at: (a) T = 50 K. (b) T = 300 K. NaF (green spheres), LiF (pink spheres), LiH (brown spheres), NaH (purple spheres).

We performed additional calculations to obtain the phonon hydrodynamic windows in pure silicon and germanium crystals based on Guyer's condition. Below a characteristic length of 10^5 nm, the hydrodynamics in both silicon and germanium are nonexistent. Figure 3.21 shows a comparison between phonon hydrodynamics regimes of silicon, germanium, fluorides (NaF, LiF), and alkali hydrides (LiH, NaH) in the ranges of ($10^5 - 10^{10}$ nm) for the characteristic length and (0 – 40 K) for the temperature. The hydrodynamics windows are impractically small for silicon ($T \approx 29.5$ K) and germanium ($T \approx 19.5$ K) at $L = 10^5$ nm, whereas for fluorides and alkali hydrides, the hydrodynamic windows are significantly wider at the same characteristic length. At this characteristic length, phonon hydrodynamics in LiH may occur up to a temperature of 34 K; in contrast, phonon hydrodynamics in NaH may occur up to a temperature of 15.5 K. As the characteristic length increases and the temperature decreases, the hydrodynamics regimes of silicon and germanium become wider.

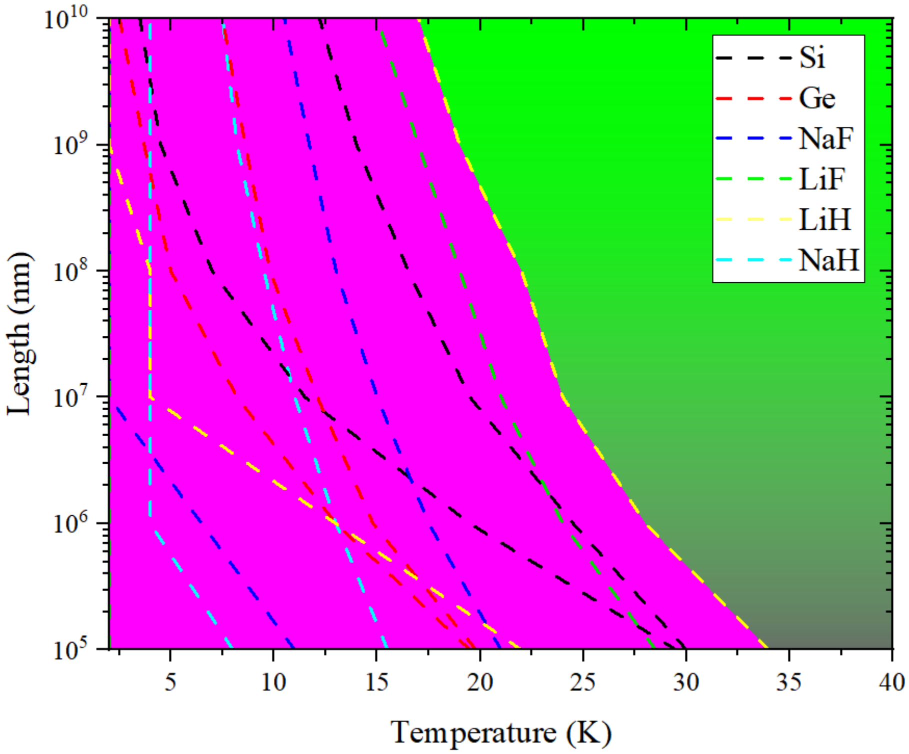

Figure 3.21: Phonon hydrodynamics in silicon (Si), germanium (Ge), sodium fluoride (NaF), lithium fluoride (LiF), lithium hydride (LiH), and sodium hydride (NaF). Thermal transport regimes: hydrodynamics regime (pink) and diffusive regime (green). The hydrodynamics regimes are denoted by colors; Si (black dashed lines), Ge (red dashed lines), NaF (blue dashed lines), LiF (green dashed lines), LiH (yellow dashed lines), and NaH (cyan dashed lines). The hydrodynamics regime of each material is between two dashed lines of the same color.

Furthermore, we examine the impact of naturally abundant isotopes on the phonon hydrodynamics windows in LiF, LiH, and NaH and contrast them with Si and Ge at L = 1 mm [175]. For LiF (Figure 3.22 (a)), the resistive scattering rate (R-scattering) can be used instead of U-scattering to predict phonon hydrodynamics (applying Eq. 2.76). Using R-scattering, the hydrodynamics window range of LiF narrows to 2 K and 9 K (shaded red region), compared with U-scattering, which extends from 2 K and 24.5 K (shaded transparent red region). On the other hand, for NaH (Figure 3.22 (c)), the curves of U-scattering and R-scattering remain close to each other, and consequently, the hydrodynamics windows are nearly the same. Finally, the hydrodynamics windows disappear for LiH, Si, and Ge if isotope scattering is included, as illustrated in Figures 3.22 (b), (d), and (e).

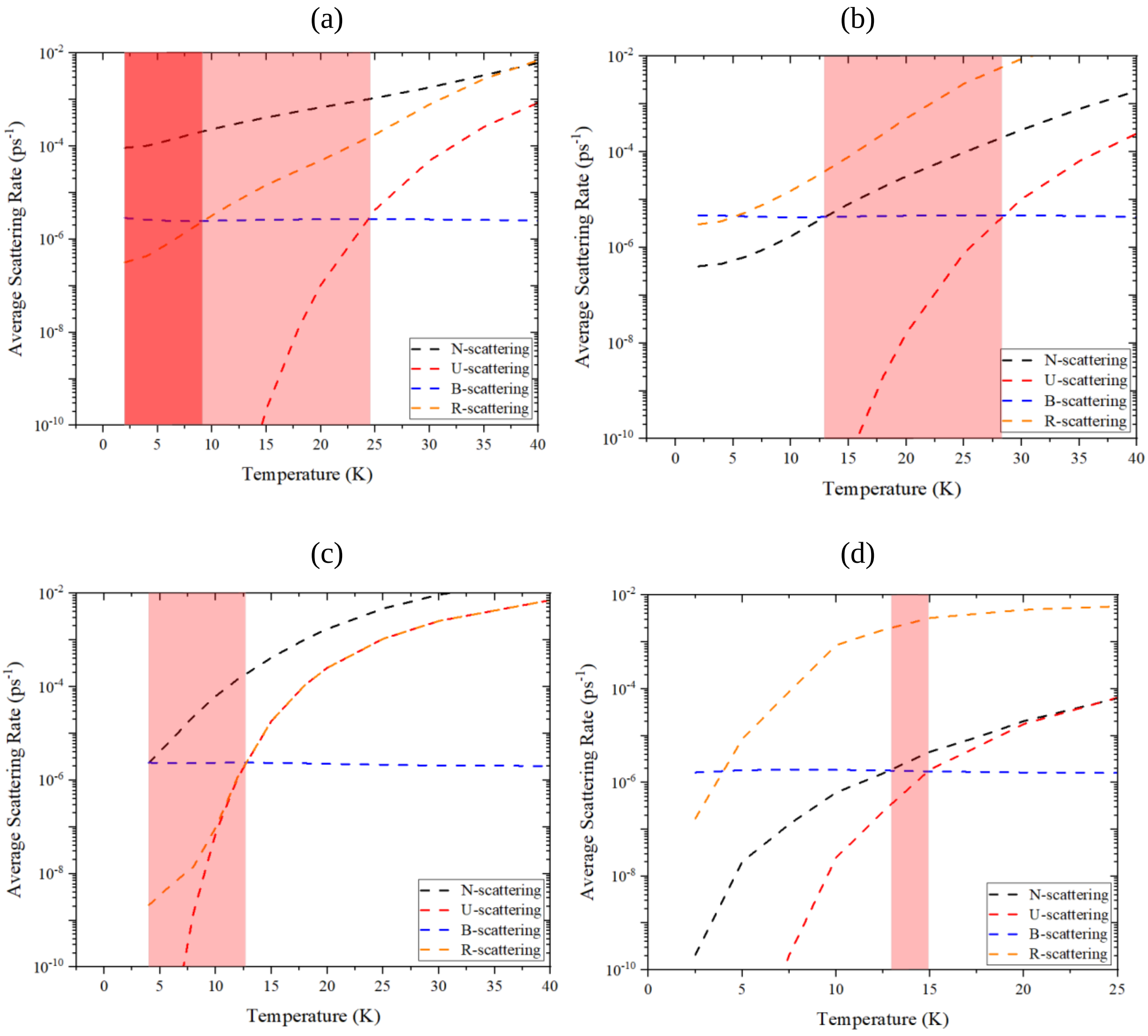
(a) (b) (c) (d)

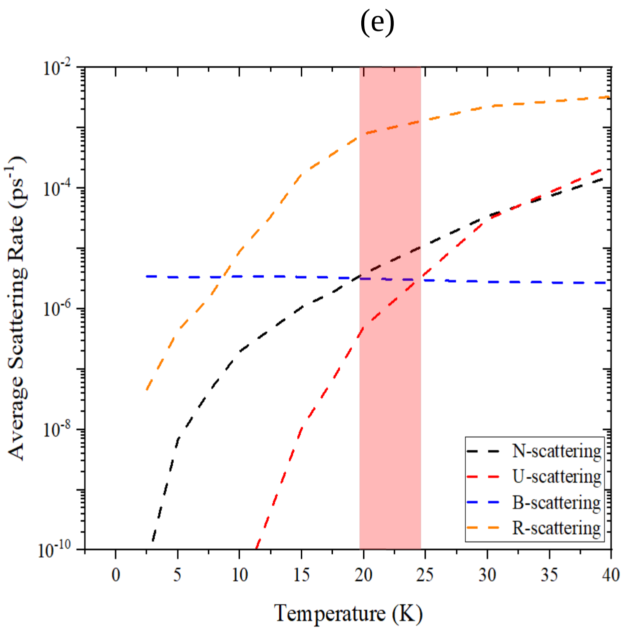

Figure 3.22: Phonon hydrodynamics windows for pure materials (shaded transparent red region) and with impurity (shaded red region) at L = 1 mm for: (a) LiF. (b) LiH. (c) NaH. (d) Ge (adapted from Ref.[175]). (e) Si. The scattering rates are denoted by colors: N-scattering (black dashed lines), U-scattering (red dashed lines), B-scattering (blue dashed lines), and R-scattering (orange dashed lines).

3.2 Phonon Hydrodynamics in Bilayer Graphene

Scientific interest in two-dimensional (2D) materials have greatly increased because of their unique features and sophisticated applications [176]–[178]. Numerous scientific publications focused heavily on graphene and its bilayer over the last decades with extensive investigations of the electrical [179]–[182], optical [183]–[187], and mechanical [188]–[191] properties. Chemical stability, excellent electrical mobility, high mechanical strength, and flexible structure are the some of the properties of interest in bilayer graphene [179], [188]. Bilayer graphene has been developed to adjust the bandgap of graphene from zero to a few electron volts by using various doping materials and electrical fields [192], which is promising for transistor applications. Bilayer graphene exists in two forms known as AA and AB-bilayer graphene. Another type of bilayer graphene is called twisted bilayer graphene, where the top monolayer of graphene is displaced at an angle (~ 1.1°, also referred to as a ‘magic’ angle [193], [194]).

Recently, phonon hydrodynamics research has come to focus on two-dimensional materials. Previous studies showed that phonon hydrodynamics windows in two-dimensional materials have been predicted to exist at higher temperatures than three-dimensional materials, which may reach room temperature [195], [196]. For a range of characteristic lengths, phonon hydrodynamics was predicted to occur between 50 and 300 K for graphene [195] and between 100 and 300 K for boron nitride (BN) [196]. According to first-principles calculations in Ref.[197], phonon hydrodynamics in graphite can be observed in a range of 50 K and 90 K, which have been confirmed experimentally but at a higher range of 85 K $< T <$ 125 K using thermal grating measurement with a grating period of 10 μm [55]. However, a recent experiment [56] captured the second sound in graphite at 200 K and 225 K using a sub-picosecond transient grating approach, which was validated in the same study by *ab-initio* simulations.

Following the procedure outlined in Sec. 2.2, we performed the necessary convergence tests for first-principles calculations. Appendix A-1 gives two examples of κ-points mesh of Monkhorst-Pack and kinetic energy cutoff convergence tests for bilayer graphene system. A 16 × 16 × 1 of κ-points mesh and 100 Ry of kinetic energy cutoff were selected with a convergence threshold of 1.0E-14 Ry. For supercells calculations, an 8 × 8 × 1 second-order supercell, 4 × 4 × 1 third-order supercell, and up to the fifth-nearest neighbor were used. For BTE calculations, interpolation was done on a 100 × 100 ×1 *q* mesh for AA-bilayer graphene and a 120 × 120 ×1 *q* mesh for AB-bilayer graphene. The PBE pseudopotential was selected due to its accuracy compared to previous experimental results. In comparison to previous DFT studies, a 13 × 13 × 1 of κ-points mesh was employed to calculate the thermal conductivity of graphene [198]. Also, a 50 × 50 ×8 *q* mesh was selected to study phonon hydrodynamics in graphite [197]. In a recent study [199], a 14 × 14 × 1 of κ-points mesh, 5 × 5 × 1 supercells, and 57 × 57 × 1 *q* mesh were used to investigate thermal transport in bilayer graphene.

Figure 3.23 presents the unit cells of bilayer graphene systems (AA-bilayer graphene and AB-bilayer graphene) after relaxing the structures with a lattice constant of 2.467 Å and an interlayer distance of 3.40 Å, in good agreement with the literature [200]–[202]. For AA-bilayer graphene (left plot), one layer is stacked directly on top of another layer, while for AB-bilayer graphene (right plot), one layer is rotated relative to the other layer by an angle, which is 67.27^{o} based on our calculations.

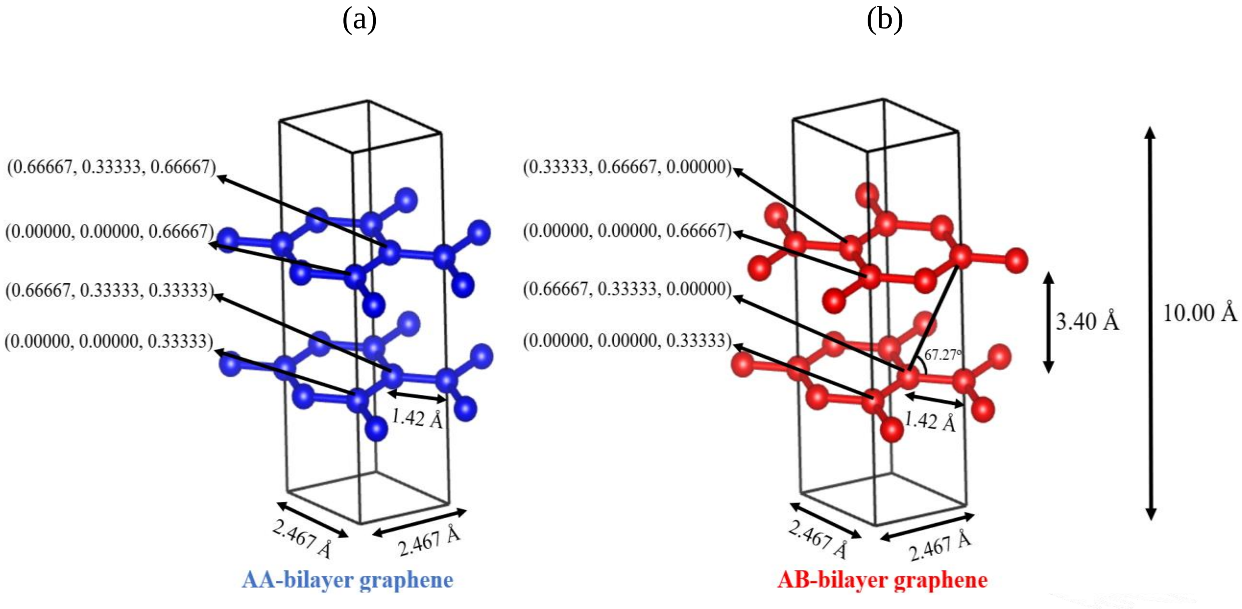

Figure 3.23: Bilayer graphene unit cells with dimensions of (2.467×2.467×10 Å), 3.40 Å interlayer distance, and 1.42 Å bond length (a) AA-bilayer graphene unit cell (b) AB-bilayer graphene unit cell with 67.27° angle between the top and bottom hexagons. The figure also shows the atomic positions of each unit cell.

A comparison between the calculated phonon dispersions of graphene, graphite, and bilayer graphene systems along the high-symmetry directions in the Brillouin zone is shown in Figure 3.24. There are six phonon branches for graphene, while there are twelve phonon branches for graphite and bilayer systems (three acoustic and nine optical phonon branches). The calculations determine a crossing of the longitudinal and transverse optical branches along the Γ-*K* and Γ-*M* directions. The phonon branches are denoted by two letters; the first letters *L*, *T*, and *Z*, for in-plane longitudinal, in-plane transverse, and out-of-plane atomic displacement, respectively. The second letters *A* and *O*, refer to optical and acoustic branches, respectively. A special mode with a finite frequency at the zone center can be observed in graphite and bilayer graphene systems called out-of-plane layer-breathing mode (ZO'), which is related to interlayer coupling [203], [204]. In the small wave vector limit, the TA and LA modes exhibit linear dispersions.

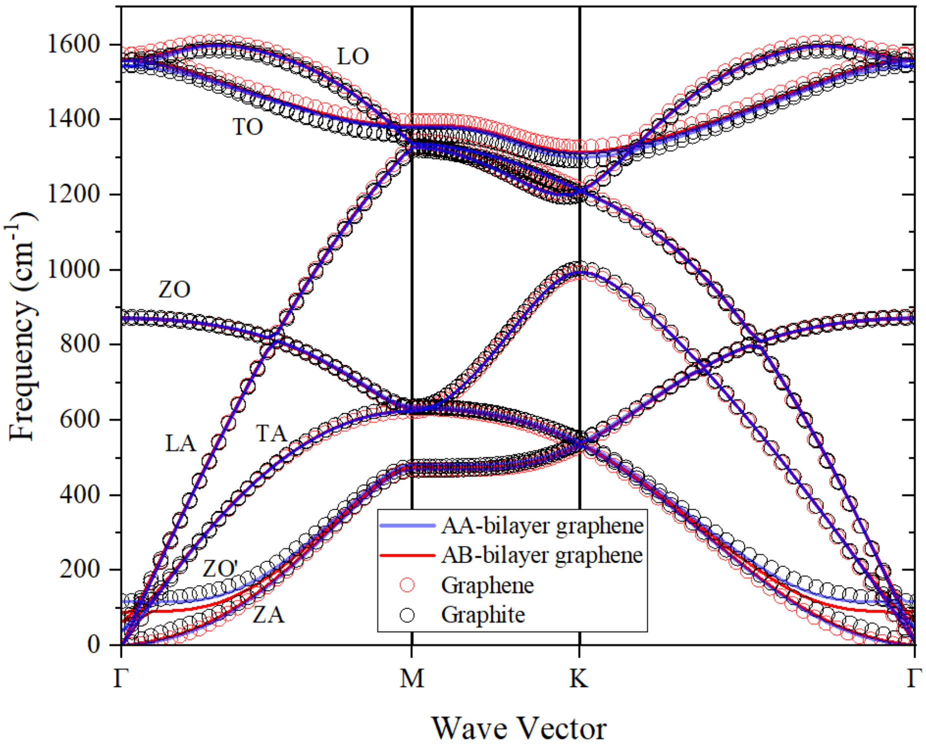

Figure 3.24: Calculated phonon dispersions for AA-bilayer graphene (blue solid line), AB- bilayer graphene (red solid line), graphene (red circles), and graphite (black circles).

For graphite, a small band-gap exists between LO and LA at the *M* point (ω = 35 cm^{-1}), which is in agreement with experiments (ω_{exp} = 33 cm^{-1}) [205], but larger band-gaps result from bilayer systems (ω_{AA} = 54 cm^{-1}, ω_{AB} = 58 cm^{-1}). At the gamma point, LA mode is doubly-degenerate with a frequency of zero; in contrast, TA mode has a low frequency of 38 cm^{-1} (~1.14 THz) for bilayer systems, in agreement with Ref.[206]. Table 3.19 compares frequencies of different phonon modes for graphene, graphite, and bilayer graphene systems at the gamma point. The frequency of ZO' mode for bilayer systems is notably lower than that of graphite. Our calculations for the ZO' mode frequency of the AB-bilayer agree with the experimental value (ω_{exp} = 80 ± 2 cm^{-1}) [204]. After relaxing the AA-bilayer graphene structure, we observed imaginary frequencies around the gamma point in the acoustic modes (~ *i* 1.1 THz) when a PBE ultrasoft pseudopotential (USPP) was used. However, these imaginary frequencies disappear when a PBE projector augmented-wave (PAW) pseudopotential and a dense second-order supercell is used. If the structure relaxed well, the imaginary frequencies indicate the presence of a phonon instability, as observed in Ref.[207] where the imaginary frequencies in the TA mode (~ *i* 1.04 THz) were found at the gamma point of the AA-bilayer graphene. It is noticed from Table 3.19 that AA-bilayer has a larger LO/TO splitting compared to AB-bilayer but less LO/TO frequencies, as found in Ref.[207]. In any case, since graphene systems are nonpolar, LO/TO splitting is negligible.

Table 3.19: Phonon frequencies (cm^{-1}) of graphene, graphite, and bilayer graphene systems at the gamma point.

		$\Gamma_{ZO'}$	Γ_{ZO}	Γ_{LO}	Γ_{TO}
Graphene	Present work	-	875	1582	1582
	Theoretical data	-	890[a1], 896[a2], 893[b1], 884[b2], 881[c1], 869[d1], 870[d2]	1595[a1], 1597[a2], 1597[b1], 1569[b2], 1554[c1], 1578[d1], 1552[d2]	1595[a1], 1597[a2], 1597[b1], 1569[b2], 1554[c1], 1578[d1], 1552[d2]
Graphite	Present work	119	876	1570	1574
	Theoretical data	135[c1], 113[c2]	879[c1], 899[c2],867[d]	1559[c1], 1593[c2], 1575[d]	1567[c1], 1604[c2], 1587[d]
	Experiments	126[e], 95[f]	861[f], 868[g]	1590[f], 1587[g,h],1575[i]	1590[f], 1587[g,h], 1575[i]
AA-bilayer	Present work	118	874	1560	1557
	Theoretical data	72[j]	895[j]	1591[j]	1572[j]
AB-bilayer	Present work	90	873	1564	1566
	Theoretical data	75[j]	870[d], 891[j]	1578[d], 1602[j]	1578[d], 1596[j]

[a1] Ref.[208], calculated using LDA – Soft PAW. [a2] Ref.[208], calculated using LDA – Hard PAW. [b1] Ref.[209], calculated using LDA. [b2] Ref.[209], calculated using GGA. [c1] Ref.[210], calculated using GGA. [c2] Ref.[210], calculated using LDA. [d] Ref.[211]. [d1] Ref.[211], calculated using C_pbevan_bm_UPF pseudopotential. [d2] Ref.[211], calculated using C.blyp_van.ak.UPF pseudopotential. [e] Ref.[212], taken from Ref.[210]. [f] Ref.[213], taken from Ref.[210]. [g] Ref.[214]. [h] Ref.[215] . [i] Ref.[216]. [j] Ref.[207], values have been converted to cm^{-1}.

Figure 3.25 shows the calculated thermal conductivity for bilayer systems in a temperature range of $T = 100 – 1000$ K. Thermal conductivity of AA-bilayer exhibits small differences from AB-bilayer at high temperatures ($T > 500$ K) with growing differences at lower temperatures ($T <$

500 K). Thermal conductivity values of AB-bilayer are in good agreement with the data from Ref.[217] between 300 K and 425 K.

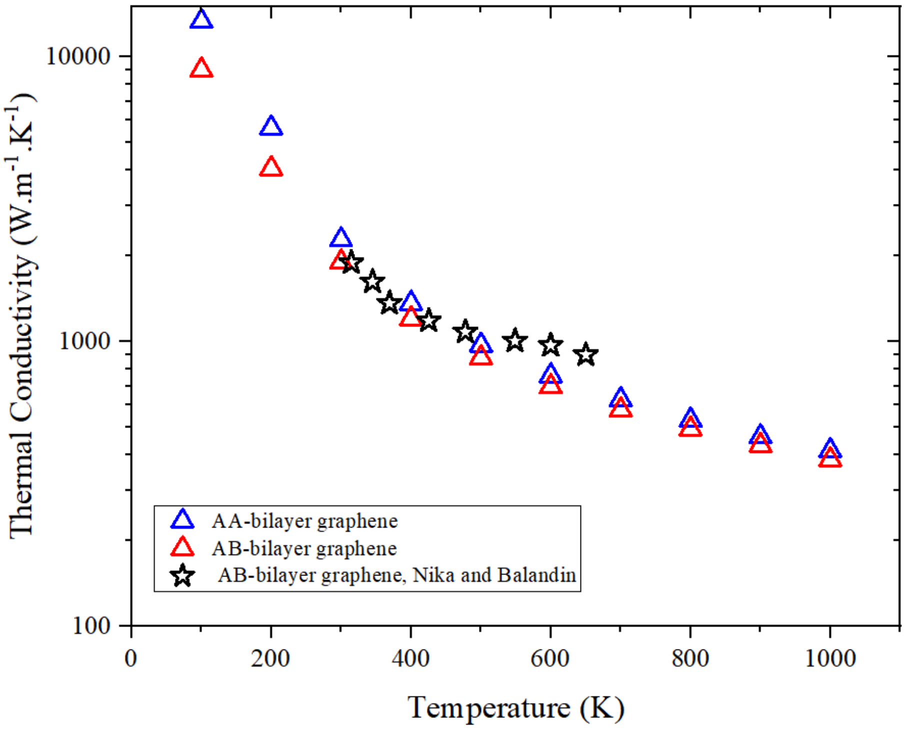

Figure 3.25: Calculated lattice thermal conductivity for bilayer systems. AA-bilayer (blue triangles), AB-bilayer (red triangles), and AB-bilayer from Ref.[217] (black stars).

We applied Guyer's condition to show phonon hydrodynamics windows in bilayer systems. For bilayer systems, as illustrated in Figures 3.26 (d) and 3.27 (d), the hydrodynamics regime appears above room temperature at a characteristic length of 100 nm. Broadly speaking, the differences in phonon hydrodynamics windows of the AA and AB bilayer systems are insignificant. The ranges of hydrodynamics windows for pure bilayer systems are the following: (i) Figures 3.26 (a) and 3.27 (a), below 60 and 50 K for AA-bilayer and AB-bilayer, respectively, at L = 10 mm. (ii) Figures 3.26 (b) and 3.27 (b), $4 < T < 110$ K for AA-bilayer and $6 < T < 105$ K for AB-bilayer at L = 10 µm. (iii) Figures 3.26 (c) and 3.27 (c), $4 < T < 325$ K for AA-bilayer and $190 < T < 332$ K for AB-bilayer at L = 100 nm. The figures also demonstrate the impact of R-scattering on the hydrodynamics windows with temperature ranges of $6 < T < 53$ K for AA-bilayer and $6 < T < 47$ K for AB-bilayer at L = 10 mm, $80 < T < 110$ K for AA-bilayer and $90 < T < 105$

K for AB-bilayer at L = 10 μm, and 305 < T < 325 K for AA-bilayer and 308 < T < 332 K for AB-bilayer at L = 100 nm.

3.2.1 Phonon Hydrodynamics in AA-bilayer graphene

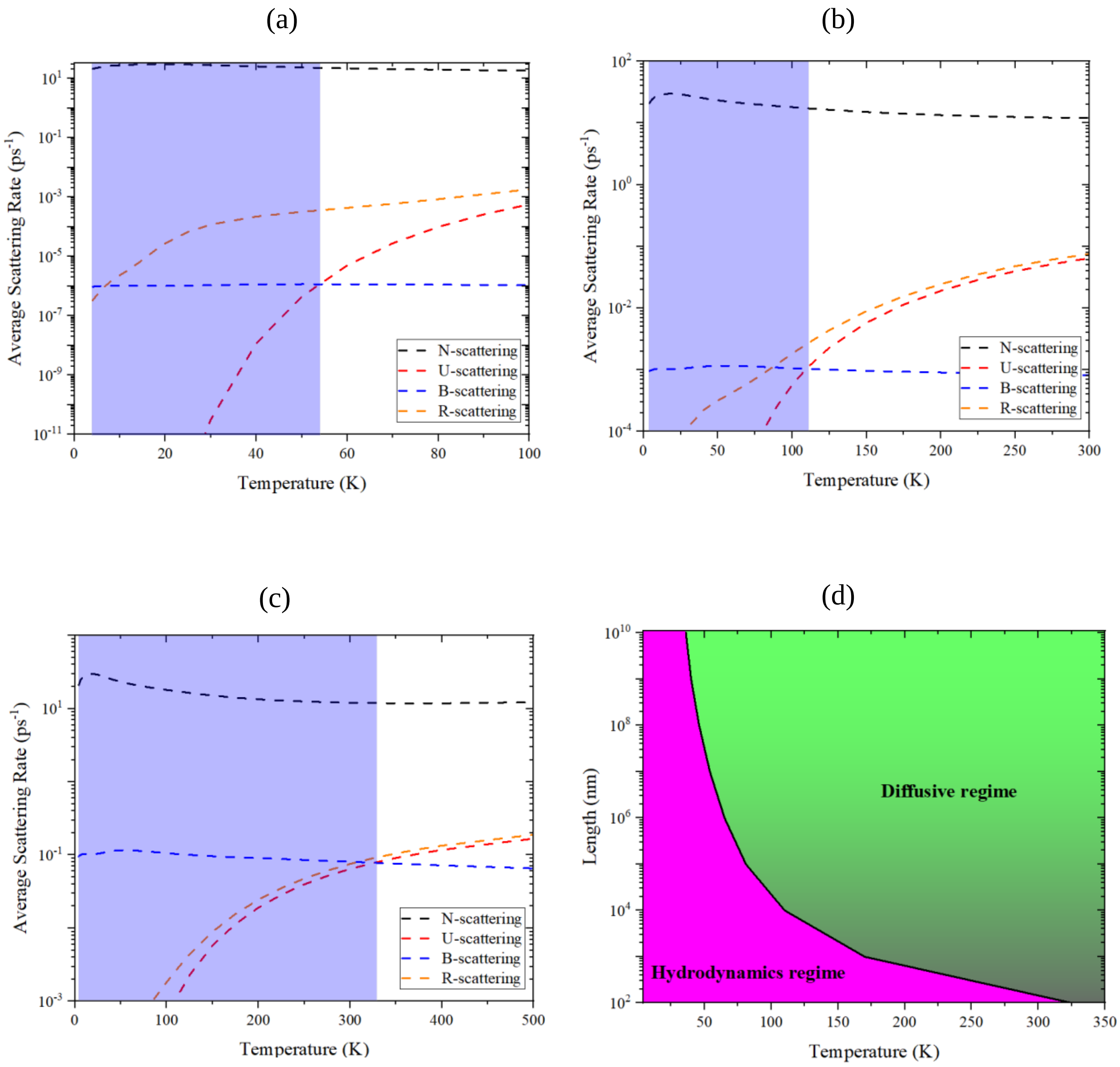

Figure 3.26: Phonon hydrodynamics windows for AA-bilayer graphene. The transparent blue color represents the hydrodynamics range. (a) At L = 10 mm. (b) At L = 10 μm. (c) At L = 100 nm. (d) Thermal transport regimes: hydrodynamics regime (pink) and diffusive regime (green). The scattering rates are denoted by colors: N-scattering (black dashed lines), U-scattering (red dashed lines), B-scattering (blue dashed lines), and R-scattering (orange dashed lines).

3.2.2 Phonon Hydrodynamics in AB-bilayer graphene

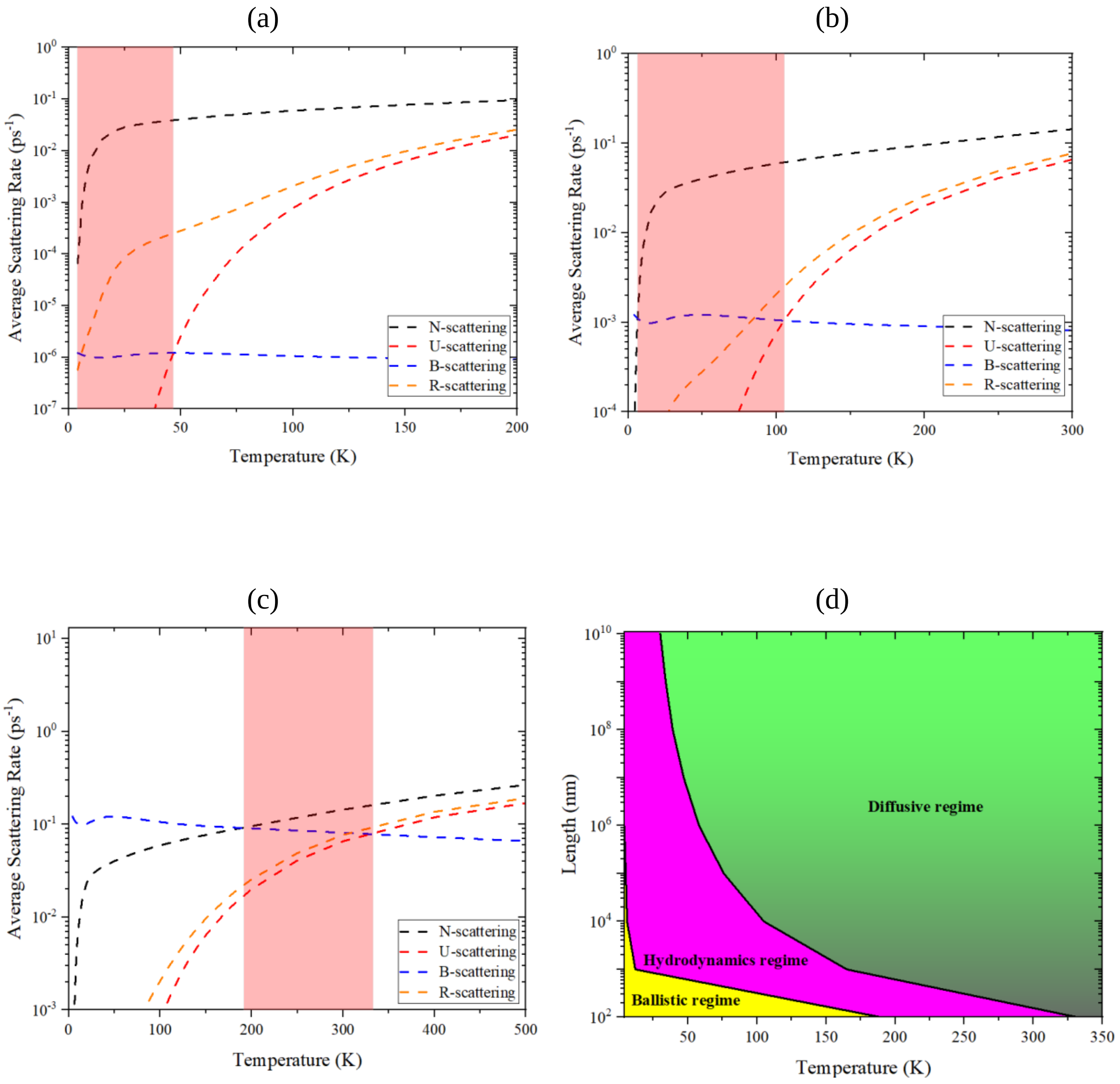

Figure 3.27: Phonon hydrodynamics windows for AB-bilayer graphene. The transparent red color represents the hydrodynamics range. (a) At L = 10 mm. (b) At L = 10 µm. (c) At L = 100 nm. (d) Thermal transport regimes: hydrodynamics regime (pink), ballistic regime (yellow), and diffusive regime (green). The scattering rates are denoted by colors: N-scattering (black dashed lines), U-scattering (red dashed lines), B-scattering (blue dashed lines), and R-scattering (orange dashed lines).

3.2.3 Discussion – Project (2)

To comprehend the differences and similarities between the phonon hydrodynamic regimes of AA and AB, we first compare phonon scattering rates (Normal, Umklapp) of AA-bilayer and AB-bilayer up to 15 THz at room temperature, as illustrated in Figure 3.28 (a). It shows that the scattering rates of bilayer systems are close to each other, with the exception of the ZO' mode (Figure 3.28 (b)).

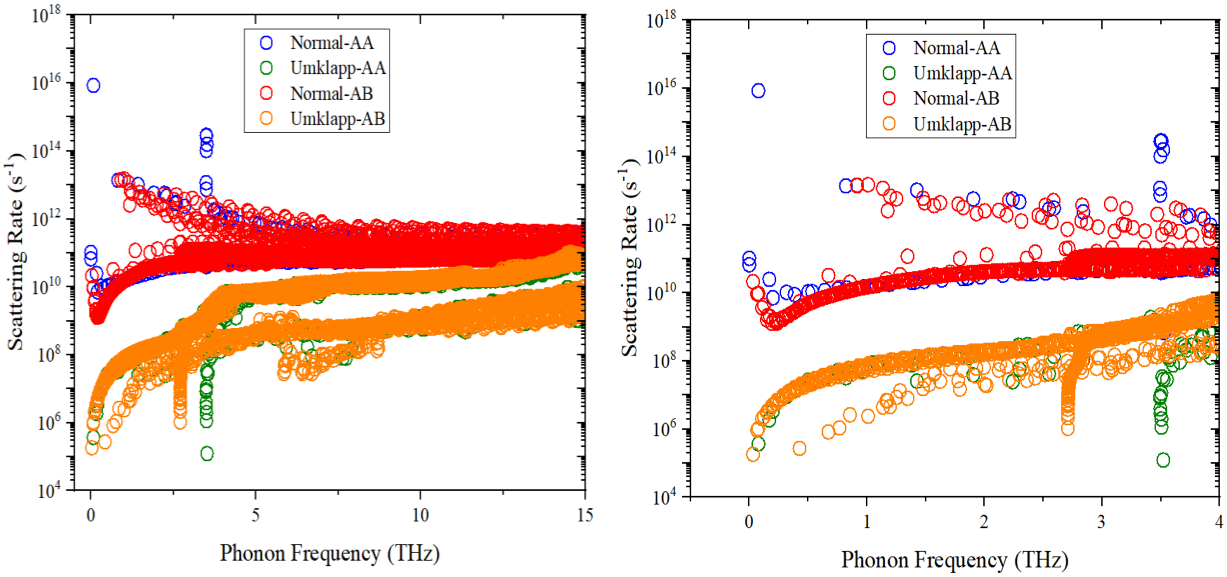
(a)
(b)

Figure 3.28: (a) Phonon scattering rates up to 15 THz at T = 300 K. (b) Phonon scattering rates of the ZO’ mode at T = 300 K. AA-bilayer graphene: Normal (blue circles) and Umklapp (green circles). AB-bilayer graphene: Normal (red circles) and Umklapp (orange circles).

A previous study hypothesized that including four-phonon interactions [218] may be responsible for the differences between the theoretical predictions and experimental observations of phonon hydrodynamics in graphite. To begin to address this question, we study the impact of four-phonon interactions on phonon hydrodynamics in bilayer systems. According to Eq.2.32 described in Sec 2.1.2, the fourth-order interatomic forces term ($\Phi_{\alpha\beta\gamma\theta}$) is written as $\Phi_{\alpha\beta\gamma\theta}(ij,i'j',i''j'',i'''j''') = \left.\frac{\partial^4 V}{\partial u_\alpha(ij)\partial u_\beta(i'j')\partial u_\gamma(i''j'')\partial u_\theta(i'''j''')}\right|_0$, which can be calculated using a real-space finite-difference method [68]. It showed that for a single temperature point with a q mesh of 16 ×16 ×16, the scattering rate calculations of BAs require roughly 1680 CPU hours [68]. Because the calculations of four-phonon are computationally expensive compared with standard three-phonon calculations for a dense *q* mesh, we are currently restricted to a *q* mesh (21 × 21 × 1) for four-phonon calculations (4ph). To check that this small mesh was sufficient to provide a qualitative picture of the impact of 4ph, we inspected the scattering rates to obtain phonon hydrodynamic windows at dense (100 × 100 × 1 for AA bilayer and 120 × 120 × 1 for AB bilayer) and small (21 × 21 × 1 for both bilayer systems) *q* meshes for the three-phonon calculations (3ph), and we compared them with four-phonon calculations (4ph) at a *q* mesh of 21 × 21 × 1, as shown in Figures 3.29 (a) and (b). Using four-phonon calculations only, the temperature may reach a value of 375 K for AA-bilayer graphene and 400 K for AB-bilayer graphene at a characteristic length of 100 nm, but lower temperatures of 350 K for AA-bilayer graphene and 332 K for AB-bilayer graphene were obtained using three-phonon calculations at the same characteristic length and *q* mesh. However, an insignificant four-phonon effect was observed when it was added to the three-phonon term, meaning 4ph shrinks the window. Our preliminary calculations indicate that AB-bilayer graphene would be a suitable candidate for near-term experiments owing to its greater stability over the AA system.

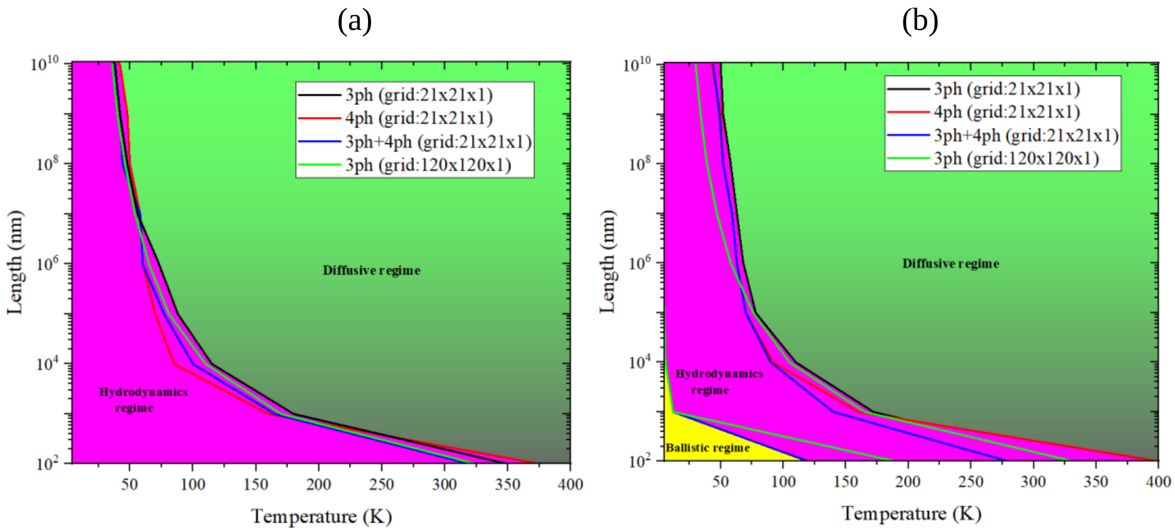

Figure 3.29: Phonon hydrodynamics in bilayer graphene systems using three-phonon (3ph) and four-phonon (4ph) calculations. (a) AA-bilayer (b) AB-bilayer. The hydrodynamics range for AB-bilayer graphene is between two lines from the same color. 3ph with a grid of 21 × 21 × 1 (black lines), 4ph with a grid of 21 × 21 × 1 (red lines), 3ph+4ph with a grid of 21 × 21 × 1 (blue lines), and 3ph with a grid of 120 × 120 × 1 (green lines). Thermal transport regimes: hydrodynamics regime (pink), ballistic regime (yellow), and diffusive regime (green).

CHAPTER 4

CONCLUSIONS AND FUTURE RESEARCH

4.1 Conclusions

First-principles calculations have been shown to be capable of computing the electrical, optical, mechanical, and thermal properties of NaF, NaH, LiH, LiF and bilayer graphene. Phonon scattering rates (BTE outputs) were used to predict phonon hydrodynamics based on Guyer's condition. At a characteristic length of 100 nm, phonon hydrodynamics were reported above room temperature for bilayer systems but below 100 K for fluorides and alkali hydrides materials. On the other hand, we showed that when isotopes were included, the phonon hydrodynamics windows in LiH disappeared, LiF’s phonon hydrodynamics window narrowed, and NaH’s phonon hydrodynamics window was unaffected. For bilayer graphene systems, we discussed the instability of AA-bilayer graphene. Various pseudopotentials (PBE, PBESOL, and LDA) were employed in first-principles calculations. We illustrated through the analysis of the results that GGA pseudopotentials (PBE and PBESOL) provide reasonable predictions of the studied materials’ properties.

4.2 Future Research

The followings are some potential projects for future work.

- Building robust software packages to predict phonon hydrodynamics. In this thesis, we focused on Guyer's condition only. However, there are other approaches, such as solving the linearized BTE with the full scattering matrix.
- Reducing the computational cost of 4ph calculations.
- Studying phonon hydrodynamics in other systems (i.e., crystalline polymers, hBN, MoS_2, etc.).
- Focusing on micro-nano applications of the second sound. To find potential applications, it is required to first understand how to control and engineer second sound. To date, second sound has been used in limited applications, such as a thermometer with helium mixtures (^3He-^4He) at low temperatures [219] and oscillating superleak transducers (OST) [220].

REFERENCES

[1] V. Peshkov, “ Second sound in helium II,” *J. Phys.*, vol. 8, 381–389., 1944.

[2] V. Narayanamurti and R. C. Dynes, “Observation of Second Sound in Bismuth,” *Phys. Rev. Lett.*, vol. 28, no. 22, pp. 1461–1465, May 1972, doi: 10.1103/PhysRevLett.28.1461.

[3] H. E. Jackson, C. T. Walker, and T. F. McNelly, “Second Sound in NaF,” *Phys. Rev. Lett.*, vol. 25, no. 1, pp. 26–28, Jul. 1970, doi: 10.1103/PhysRevLett.25.26.

[4] T. Bergman, A. Lavine, F. Incropera, and D. DeWitt, *Fundamentals of Heat and Mass Transfer*. 2011.

[5] R. Mortimer, *Physical Chemistry*. 2008.

[6] G. Jyh Hwang, *Transport Phenomena In Thermal Control*. 1989.

[7] M. Kaviany, *Essentials of Heat Transfer*. Cambridge University Press, 2011. doi: 10.1017/CBO9780511998195.

[8] G. Chen, *Nanoscale Energy Transport and Conversion: A Parallel Treatment of Electrons, Molecules, Phonons, and Photons*. 2005.

[9] K. D. Sattler, Ed., *21st Century Nanoscience – A Handbook*. Boca Raton, Florida : CRC Press, [2020]: CRC Press, 2019. doi: 10.1201/9780367333003.

[10] M. Kaviany, *Heat Transfer Physics*. Cambridge: Cambridge University Press, 2008. doi: 10.1017/CBO9780511754586.

[11] M. Chester, “Second Sound in Solids,” *Phys. Rev.*, vol. 131, no. 5, pp. 2013–2015, Sep. 1963, doi: 10.1103/PhysRev.131.2013.

[12] J. A. Krumhansl, “Thermal conductivity of insulating crystals in the presence of normal processes,” *Proc. Phys. Soc.*, vol. 85, no. 5, pp. 921–930, May 1965, doi: 10.1088/0370-1328/85/5/310.

[13] L. Mezhov-Deglin, “Measurement of the thermal conductivity of crystalline He4,” *J. Exp.*

Theor. Phys., 1965.

[14] R. A. Guyer and J. A. Krumhansl, “Thermal Conductivity, Second Sound, and Phonon Hydrodynamic Phenomena in Nonmetallic Crystals,” *Phys. Rev.*, vol. 148, no. 2, pp. 778–788, Aug. 1966, doi: 10.1103/PhysRev.148.778.

[15] T. F. McNelly *et al.*, “Heat Pulses in NaF: Onset of Second Sound,” *Phys. Rev. Lett.*, vol. 24, no. 3, pp. 100–102, Jan. 1970, doi: 10.1103/PhysRevLett.24.100.

[16] D. Raabe, “Overview of the lattice Boltzmann method for nano- and microscale fluid dynamics in materials science and engineering,” *Model. Simul. Mater. Sci. Eng.*, vol. 12, no. 6, pp. R13–R46, Nov. 2004, doi: 10.1088/0965-0393/12/6/R01.

[17] R. T. Hanlon, *Block by Block: The Historical and Theoretical Foundations of Thermodynamics*. Oxford University Press, 2020. doi: 10.1093/oso/9780198851547.001.0001.

[18] M. Born and T. von Karman, “Uber Schwingungen im Raumgittern,” *Phys. Zeitschrift*, vol. 13, pp. 297–309.

[19] D. Saint-James, “Détermination des lois de force dans les cristaux du type du diamant,” *J. Phys. Chem. Solids*, vol. 5, no. 4, pp. 337–355, Jan. 1958, doi: 10.1016/0022-3697(58)90037-4.

[20] C. Kittel, *Introduction to Solid State Physics*. 1953.

[21] T. Hom, W. Kiszenik, and B. Post, “Accurate lattice constants from multiple reflection measurements. II. Lattice constants of germanium, silicon, and diamond,” *J. Appl. Crystallogr.*, vol. 8, no. 4, pp. 457–458, Aug. 1975, doi: 10.1107/S0021889875010965.

[22] N. W. Ashcroft and N. D. Mermin, *Solid State Physics*. 1976.

[23] *Thermophysical Properties of Materials*. Elsevier, 1999. doi: 10.1016/B978-0-444-82794-4.X5000-1.

[24] J. F. Nye, *Physical Properties of Crystals*. 1964.

[25] M. T. Dove, *Introduction to Lattice Dynamics*. Cambridge University Press, 1993. doi: 10.1017/CBO9780511619885.

[26] H. J. McSkimin and P. Andreatch, “Elastic Moduli of Silicon vs Hydrostatic Pressure at 25.0°C and − 195.8°C,” *J. Appl. Phys.*, vol. 35, no. 7, pp. 2161–2165, Jul. 1964, doi: 10.1063/1.1702809.

[27] W. B. Daniels, “Pressure Variation of the Elastic Constants of Sodium,” *Phys. Rev.*, vol. 119, no. 4, pp. 1246–1252, Aug. 1960, doi: 10.1103/PhysRev.119.1246.

[28] H. J. McSkimin, “Measurement of the Elastic Constants of Single Crystal Cobalt,” *J. Appl. Phys.*, vol. 26, no. 4, pp. 406–409, Apr. 1955, doi: 10.1063/1.1722007.

[29] A. R. Wazzan and L. B. Robinson, “Elastic Constants of Magnesium-Lithium Alloys,” *Phys. Rev.*, vol. 155, no. 3, pp. 586–594, Mar. 1967, doi: 10.1103/PhysRev.155.586.

[30] A. de Bretteville, E. R. Cohen, A. D. Ballato, I. N. Greenberg, and S. Epstein, “Least-Squares Determination of the Elastic Constants of Antimony and Bismuth,” *Phys. Rev.*, vol. 148, no. 2, pp. 575–579, Aug. 1966, doi: 10.1103/PhysRev.148.575.

[31] E. Fermi, P. Pasta, S. Ulam, and M. Tsingou, “STUDIES OF THE NONLINEAR PROBLEMS,” Los Alamos, NM (United States), May 1955. doi: 10.2172/4376203.

[32] D. K. Campbell, P. Rosenau, and G. M. Zaslavsky, “Introduction: The Fermi–Pasta–Ulam problem—The first fifty years,” *Chaos An Interdiscip. J. Nonlinear Sci.*, vol. 15, no. 1, p. 15101, Mar. 2005, doi: 10.1063/1.1889345.

[33] D. J. Korteweg and G. de Vries, “XLI. On the change of form of long waves advancing in a rectangular canal, and on a new type of long stationary waves,” *London, Edinburgh, Dublin Philos. Mag. J. Sci.*, vol. 39, no. 240, pp. 422–443, May 1895, doi: 10.1080/14786449508620739.

[34] N. J. Zabusky and M. D. Kruskal, “Interaction of ‘Solitons’ in a Collisionless Plasma and the Recurrence of Initial States,” *Phys. Rev. Lett.*, vol. 15, no. 6, pp. 240–243, Aug. 1965, doi: 10.1103/PhysRevLett.15.240.

[35] T. Dauxois, M. Peyrard, and S. Ruffo, “The Fermi–Pasta–Ulam ‘numerical experiment’: history and pedagogical perspectives,” *Eur. J. Phys.*, vol. 26, no. 5, pp. S3–S11, Sep. 2005, doi: 10.1088/0143-0807/26/5/S01.

[36] L. I. Schiff, *Quantum Mechanics*, 3rd Edition. 1968.

[37] M. Lundstrom and C. Jeong, *Near-Equilibrium Transport*, vol. 2. WORLD SCIENTIFIC, 2013. doi: 10.1142/7975.

[38] R. Peierls, "Zur kinetischen Theorie der Wärmeleitung in Kristallen," *Ann. Phys.*, vol. 395, no. 8, pp. 1055–1101, 1929, doi: 10.1002/andp.19293950803.

[39] J. Callaway, "Model for Lattice Thermal Conductivity at Low Temperatures," *Phys. Rev.*, vol. 113, no. 4, pp. 1046–1051, Feb. 1959, doi: 10.1103/PhysRev.113.1046.

[40] A. Ward and D. A. Broido, "Intrinsic phonon relaxation times from first-principles studies of the thermal conductivities of Si and Ge," *Phys. Rev. B*, vol. 81, no. 8, p. 85205, Feb. 2010, doi: 10.1103/PhysRevB.81.085205.

[41] J. Zou and A. Balandin, "Phonon heat conduction in a semiconductor nanowire," *J. Appl. Phys.*, vol. 89, no. 5, pp. 2932–2938, Mar. 2001, doi: 10.1063/1.1345515.

[42] S. Succi, *The Lattice Boltzmann Equation for Fluid Dynamics and Beyond*. 2001.

[43] H. Beck, P. F. Meier, and A. Thellung, "Phonon hydrodynamics in solids," *Phys. Status Solidi*, vol. 24, no. 1, pp. 11–63, Jul. 1974, doi: 10.1002/pssa.2210240102.

[44] C. Jacoboni and L. Reggiani, "The Monte Carlo method for the solution of charge transport in semiconductors with applications to covalent materials," *Rev. Mod. Phys.*, vol. 55, no. 3, pp. 645–705, Jul. 1983, doi: 10.1103/RevModPhys.55.645.

[45] G. A. Bird, *Molecular Gas Dynamics and the Direct Simulation of Gas Flows*, 2nd Edition. 1994.

[46] T. Klitsner, J. E. VanCleve, H. E. Fischer, and R. O. Pohl, "Phonon radiative heat transfer and surface scattering," *Phys. Rev. B*, vol. 38, no. 11, pp. 7576–7594, Oct. 1988, doi: 10.1103/PhysRevB.38.7576.

[47] S. Mazumder and A. Majumdar, "Monte Carlo Study of Phonon Transport in Solid Thin Films Including Dispersion and Polarization," *J. Heat Transfer*, vol. 123, no. 4, pp. 749–759, Aug. 2001, doi: 10.1115/1.1377018.

[48] S. Bandyopadhyay, *Physics of Nanostructured Solid State Devices*. Boston, MA: Springer

US, 2012. doi: 10.1007/978-1-4614-1141-3.

[49] S. Pettersson, “Solving the phonon Boltzmann equation with the variational method,” *Phys. Rev. B*, vol. 43, no. 11, pp. 9238–9246, Apr. 1991, doi: 10.1103/PhysRevB.43.9238.

[50] V. Chiloyan, L. Zeng, S. Huberman, A. A. Maznev, K. A. Nelson, and G. Chen, “Variational approach to solving the spectral Boltzmann transport equation in transient thermal grating for thin films,” *J. Appl. Phys.*, vol. 120, no. 2, p. 25103, Jul. 2016, doi: 10.1063/1.4955164.

[51] S. L. Shindé and G. P. Srivastava, Eds., *Length-Scale Dependent Phonon Interactions*, vol. 128. New York, NY: Springer New York, 2014. doi: 10.1007/978-1-4614-8651-0.

[52] M. G. Holland, “Analysis of Lattice Thermal Conductivity,” *Phys. Rev.*, vol. 132, no. 6, pp. 2461–2471, Dec. 1963, doi: 10.1103/PhysRev.132.2461.

[53] C. C. Ackerman and W. C. Overton, “Second Sound in Solid Helium-3,” *Phys. Rev. Lett.*, vol. 22, no. 15, pp. 764–766, Apr. 1969, doi: 10.1103/PhysRevLett.22.764.

[54] L. Landau, “Theory of the Superfluidity of Helium II,” *Phys. Rev.*, vol. 60, no. 4, pp. 356–358, Aug. 1941, doi: 10.1103/PhysRev.60.356.

[55] S. Huberman *et al.*, “Observation of second sound in graphite at temperatures above 100 K,” *Science (80-.).*, vol. 364, no. 6438, pp. 375–379, Apr. 2019, doi: 10.1126/science.aav3548.

[56] Z. Ding *et al.*, “Observation of second sound in graphite over 200 K,” *Nat. Commun.*, vol. 13, no. 1, p. 285, Dec. 2022, doi: 10.1038/s41467-021-27907-z.

[57] C. P. Enz, “One-particle densities, thermal propagation, and second sound in dielectric crystals,” *Ann. Phys. (N. Y).*, vol. 46, no. 1, pp. 114–173, Jan. 1968, doi: 10.1016/0003-4916(68)90305-9.

[58] R. J. Hardy, “Phonon Boltzmann Equation and Second Sound in Solids,” *Phys. Rev. B*, vol. 2, no. 4, pp. 1193–1207, Aug. 1970, doi: 10.1103/PhysRevB.2.1193.

[59] S. Lee and X. Li, “Hydrodynamic phonon transport: past, present and prospects,” in *Nanoscale Energy Transport*, IOP Publishing, 2020, pp. 1-1-1–26. doi: 10.1088/978-0-7503-1738-2ch1.

[60] W. Kohn and L. J. Sham, “Self-Consistent Equations Including Exchange and Correlation Effects,” *Phys. Rev.*, vol. 140, no. 4A, pp. A1133–A1138, Nov. 1965, doi: 10.1103/PhysRev.140.A1133.

[61] J. P. Perdew, K. Burke, and M. Ernzerhof, “Generalized Gradient Approximation Made Simple,” *Phys. Rev. Lett.*, vol. 77, no. 18, pp. 3865–3868, Oct. 1996, doi: 10.1103/PhysRevLett.77.3865.

[62] Z. Chen and J. Yang, “The B3LYP hybrid density functional study on solids,” *Front. Phys. China*, vol. 1, no. 3, pp. 339–343, Sep. 2006, doi: 10.1007/s11467-006-0026-8.

[63] J. P. Perdew *et al.*, “Restoring the Density-Gradient Expansion for Exchange in Solids and Surfaces,” *Phys. Rev. Lett.*, vol. 100, no. 13, p. 136406, Apr. 2008, doi: 10.1103/PhysRevLett.100.136406.

[64] K. Momma and F. Izumi, “VESTA : a three-dimensional visualization system for electronic and structural analysis,” *J. Appl. Crystallogr.*, vol. 41, no. 3, pp. 653–658, Jun. 2008, doi: 10.1107/S0021889808012016.

[65] P. Giannozzi *et al.*, “QUANTUM ESPRESSO: a modular and open-source software project for quantum simulations of materials,” *J. Phys. Condens. Matter*, vol. 21, no. 39, p. 395502, Sep. 2009, doi: 10.1088/0953-8984/21/39/395502.

[66] W. Li, J. Carrete, N. A. Katcho, and N. Mingo, “ShengBTE: A solver of the Boltzmann transport equation for phonons,” *Comput. Phys. Commun.*, vol. 185, no. 6, pp. 1747–1758, Jun. 2014, doi: 10.1016/j.cpc.2014.02.015.

[67] N. A. Spaldin, “A beginner’s guide to the modern theory of polarization,” *J. Solid State Chem.*, vol. 195, pp. 2–10, Nov. 2012, doi: 10.1016/j.jssc.2012.05.010.

[68] Z. Han, X. Yang, W. Li, T. Feng, and X. Ruan, “FourPhonon: An extension module to ShengBTE for computing four-phonon scattering rates and thermal conductivity,” *Comput. Phys. Commun.*, vol. 270, p. 108179, Jan. 2022, doi: 10.1016/j.cpc.2021.108179.

[69] T. van Mourik, M. Bühl, and M.-P. Gaigeot, “Density functional theory across chemistry, physics and biology,” *Philos. Trans. R. Soc. A Math. Phys. Eng. Sci.*, vol. 372, no. 2011, p. 20120488, Mar. 2014, doi: 10.1098/rsta.2012.0488.

[70] K. Esfarjani, J. Garg, and G. Chen, “MODELING HEAT CONDUCTION FROM FIRST PRINCIPLES,” *Annu. Rev. Heat Transf.*, vol. 17, no. N/A, pp. 9–47, 2014, doi: 10.1615/AnnualRevHeatTransfer.2014007746.

[71] J. R. Rice, W. A. Boyd, D. Chandra, M. V. Smith, P. K. Den Besten, and J. H. Freedman, “Comparison of the toxicity of fluoridation compounds in the nematode Caenorhabditis elegans,” *Environ. Toxicol. Chem.*, vol. 33, no. 1, pp. 82–88, Jan. 2014, doi: 10.1002/etc.2394.

[72] J. Mao, Q. Gu, and D. Gregory, “Revisiting the Hydrogen Storage Behavior of the Na-O-H System,” *Materials (Basel).*, vol. 8, no. 5, pp. 2191–2203, Apr. 2015, doi: 10.3390/ma8052191.

[73] L. Wang, M. Z. Quadir, and K.-F. Aguey-Zinsou, “Direct and reversible hydrogen storage of lithium hydride (LiH) nanoconfined in high surface area graphite,” *Int. J. Hydrogen Energy*, vol. 41, no. 40, pp. 18088–18094, Oct. 2016, doi: 10.1016/j.ijhydene.2016.07.073.

[74] F. D. Grant, F. H. Fahey, A. B. Packard, R. T. Davis, A. Alavi, and S. T. Treves, “Skeletal PET with 18 F-Fluoride: Applying New Technology to an Old Tracer,” *J. Nucl. Med.*, vol. 49, no. 1, pp. 68–78, Jan. 2008, doi: 10.2967/jnumed.106.037200.

[75] A. A. Ordonez, V. P. DeMarco, M. H. Klunk, S. Pokkali, and S. K. Jain, “Imaging Chronic Tuberculous Lesions Using Sodium [18F]Fluoride Positron Emission Tomography in Mice,” *Mol. Imaging Biol.*, vol. 17, no. 5, pp. 609–614, Oct. 2015, doi: 10.1007/s11307-015-0836-6.

[76] M. D. Furnish, L. C. Chhabildas, and W. D. Reinhart, “Time-resolved particle velocity measurements at impact velocities of 10 km/s,” *Int. J. Impact Eng.*, vol. 23, no. 1, pp. 261–270, Dec. 1999, doi: 10.1016/S0734-743X(99)00078-0.

[77] Y. Ishii, K. Sato, M. Salanne, P. A. Madden, and N. Ohtori, “Thermal Conductivity of Molten Alkali Metal Fluorides (LiF, NaF, KF) and Their Mixtures,” *J. Phys. Chem. B*, vol. 118, no. 12, pp. 3385–3391, Mar. 2014, doi: 10.1021/jp411781n.

[78] M. He, R. Guo, G. M. Hobold, H. Gao, and B. M. Gallant, “The intrinsic behavior of lithium fluoride in solid electrolyte interphases on lithium,” *Proc. Natl. Acad. Sci.*, vol. 117, no. 1,

pp. 73–79, Jan. 2020, doi: 10.1073/pnas.1911017116.

[79] H. E. Jackson and C. T. Walker, “Thermal Conductivity, Second Sound, and Phonon-Phonon Interactions in NaF,” *Phys. Rev. B*, vol. 3, no. 4, pp. 1428–1439, Feb. 1971, doi: 10.1103/PhysRevB.3.1428.

[80] M. E. Wieser *et al.*, “Atomic weights of the elements 2011 (IUPAC Technical Report),” *Pure Appl. Chem.*, vol. 85, no. 5, pp. 1047–1078, Apr. 2013, doi: 10.1351/PAC-REP-13-03-02.

[81] W. J. L. Buyers, “Lattice Dynamics of Sodium Fluoride,” *Phys. Rev.*, vol. 153, no. 3, pp. 923–930, Jan. 1967, doi: 10.1103/PhysRev.153.923.

[82] P. D. Pathak, J. M. Trivedi, and N. G. Vasavada, “Thermal expansion of NaF, KBr and RbBr and temperature variation of the frequency spectrum of NaF,” *Acta Crystallogr. Sect. A*, vol. 29, no. 4, pp. 477–479, Jul. 1973, doi: 10.1107/S0567739473001142.

[83] T. Liang, W.-Q. Chen, C.-E. Hu, X.-R. Chen, and Q.-F. Chen, “Lattice dynamics and thermal conductivity of lithium fluoride via first-principles calculations,” *Solid State Commun.*, vol. 272, pp. 28–32, Apr. 2018, doi: 10.1016/j.ssc.2018.01.004.

[84] M. Born, K. Huang, and M. Lax, “Dynamical Theory of Crystal Lattices,” *Am. J. Phys.*, vol. 23, no. 7, pp. 474–474, Oct. 1955, doi: 10.1119/1.1934059.

[85] F. Tran and P. Blaha, “Accurate Band Gaps of Semiconductors and Insulators with a Semilocal Exchange-Correlation Potential,” *Phys. Rev. Lett.*, vol. 102, no. 22, p. 226401, Jun. 2009, doi: 10.1103/PhysRevLett.102.226401.

[86] J. A. Camargo-Martínez and R. Baquero, “Performance of the modified Becke-Johnson potential for semiconductors,” *Phys. Rev. B*, vol. 86, no. 19, p. 195106, Nov. 2012, doi: 10.1103/PhysRevB.86.195106.

[87] I. S. Messaoudi, A. Zaoui, and M. Ferhat, “Band-gap and phonon distribution in alkali halides,” *Phys. status solidi*, vol. 252, no. 3, pp. 490–495, Mar. 2015, doi: 10.1002/pssb.201451268.

[88] H.-Y. Wang, Q.-K. Hu, C.-Y. Li, Y.-C. Wang, and G.-F. Mi, “Phase transition, elastic, and

thermodynamic properties of NaF under high pressure," *Phase Transitions*, vol. 85, no. 5, pp. 409–418, May 2012, doi: 10.1080/01411594.2011.635521.

[89] S. Härtel, J. Vogt, and H. Weiss, "Relaxation and thermal vibrations at the NaF(100) surface," *Surf. Sci.*, vol. 604, no. 21–22, pp. 1996–2001, Oct. 2010, doi: 10.1016/j.susc.2010.08.009.

[90] M. Prencipe, A. Zupan, R. Dovesi, E. Aprà, and V. R. Saunders, "Ab Initio Study of the Structural Properties of LiF, NaF, KF, LiCl, NaCl, and KCl," *Phys. Rev. B*, vol. 51, no. 6, pp. 3391–3396, Feb. 1995, doi: 10.1103/PhysRevB.51.3391.

[91] A. Solovyeva and O. A. von Lilienfeld, "Alchemical screening of ionic crystals," *Phys. Chem. Chem. Phys.*, vol. 18, no. 45, pp. 31078–31091, 2016, doi: 10.1039/C6CP04258A.

[92] *CRC Handbook of Chemistry and Physics*. CRC Press, 2014. doi: 10.1201/b17118.

[93] R. P. Lowndes and D. H. Martin, "Dielectric dispersion and the structures of ionic lattices," *Proc. R. Soc. London. Ser. A. Math. Phys. Sci.*, vol. 308, no. 1495, pp. 473–496, Jan. 1969, doi: 10.1098/rspa.1969.0021.

[94] A. Shukla, "Ab Initio Hartree-Fock Born Effective Charges of LiH, LiF, LiCl, NaF, and NaCl," *Phys. Rev. B*, vol. 61, no. 19, pp. 13277–13282, May 2000, doi: 10.1103/PhysRevB.61.13277.

[95] G. Raunio, L. Almqvist, and R. Stedman, "Phonon Dispersion Relations in NaCl," *Phys. Rev.*, vol. 178, no. 3, pp. 1496–1501, Feb. 1969, doi: 10.1103/PhysRev.178.1496.

[96] F. C. Brown, C. Gähwiller, H. Fujita, A. B. Kunz, W. Scheifley, and N. Carrera, "Extreme-Ultraviolet Spectra of Ionic Crystals," *Phys. Rev. B*, vol. 2, no. 6, pp. 2126–2138, Sep. 1970, doi: 10.1103/PhysRevB.2.2126.

[97] I. A. Smirnov, "Thermal conductivity of sodium fluoride single crystals with potassium, lithium, and chlorine impurities," *Fiz. Tverd. Tela* , vol. 9, 1845−7, 1967.

[98] A. V Petrov, N. S. Tsypkina, and Y. A. Logachev, "Temperature dependence of the thermal conductivity of alkali metal halides at elevated temperatures," *Fiz. Tverd. Tela* , vol. 16, 65−70, 1974.

[99] C. T. Walker, “Thermal Conductivity of Some Alkali Halides Containing F Centers,” *Phys. Rev.*, vol. 132, no. 5, pp. 1963–1975, Dec. 1963, doi: 10.1103/PhysRev.132.1963.

[100] A. E. Gheribi, M. Salanne, and P. Chartrand, “Formulation of Temperature-Dependent Thermal Conductivity of NaF, β-Na3AlF6, Na5Al3F14, and Molten Na3AlF6 Supported by Equilibrium Molecular Dynamics and Density Functional Theory,” *J. Phys. Chem. C*, vol. 120, no. 40, pp. 22873–22886, Oct. 2016, doi: 10.1021/acs.jpcc.6b07959.

[101] Y.S. Touloukian and E. H. Buyco, *Thermophysical Properties of Matter*, vol. Vol.5. 1970.

[102] C. M. Kachhava and S. C. Saxena, “Semiempirical Formulas for Thermal Expansion and Grüneisen Constants of Ionic Crystals,” *J. Appl. Phys.*, vol. 39, no. 6, pp. 2973–2975, May 1968, doi: 10.1063/1.1656711.

[103] J. T. Lewis, A. Lehoczky, and C. V. Briscoe, “Elastic Constants of the Alkali Halides at 4.2°K,” *Phys. Rev.*, vol. 161, no. 3, pp. 877–887, Sep. 1967, doi: 10.1103/PhysRev.161.877.

[104] R. A. Miller and C. S. Smith, “Pressure derivatives of the elastic constants of LiF and NaF,” *J. Phys. Chem. Solids*, vol. 25, no. 12, pp. 1279–1292, Dec. 1964, doi: 10.1016/0022-3697(64)90043-5.

[105] K. Spangenberg and S. Haussühl, “Die elastischen Konstanten der Alkalihalogenide vom Steinsalz-Typus,” *Zeitschrift für Krist.*, vol. 109, no. 1–6, pp. 422–437, Jan. 1957, doi: 10.1524/zkri.1957.109.1-6.422.

[106] S. Haussühl, *Z. Phys.*, vol. 159, 223, 1960.

[107] A. Otero-de-la-Roza and V. Luaña, “Gibbs2: A new version of the quasi-harmonic model code. I. Robust treatment of the static data,” *Comput. Phys. Commun.*, vol. 182, no. 8, pp. 1708–1720, Aug. 2011, doi: 10.1016/j.cpc.2011.04.016.

[108] M. J. L. Sangster and R. M. Atwood, “Interionic potentials for alkali halides. II. Completely crystal independent specification of Born-Mayer potentials,” *J. Phys. C Solid State Phys.*, vol. 11, no. 8, pp. 1541–1555, Apr. 1978, doi: 10.1088/0022-3719/11/8/015.

[109] G. Dolling, H. G. Smith, R. M. Nicklow, P. R. Vijayaraghavan, and M. K. Wilkinson, “Lattice Dynamics of Lithium Fluoride,” *Phys. Rev.*, vol. 168, no. 3, pp. 970–979, Apr.

1968, doi: 10.1103/PhysRev.168.970.

[110] L. Lindsay, "Isotope scattering and phonon thermal conductivity in light atom compounds: LiH and LiF," *Phys. Rev. B*, vol. 94, no. 17, p. 174304, Nov. 2016, doi: 10.1103/PhysRevB.94.174304.

[111] H. J. Hou, H. Guan, S. R. Zhang, L. H. Xie, and L. Wang, "Structural, Phonon and Thermodynamic Properties of the Rocksalt Structure LiF from First Principles," *Mater. Sci. Forum*, vol. 850, pp. 348–353, Mar. 2016, doi: 10.4028/www.scientific.net/MSF.850.348.

[112] Y. Ekinci and J. . Toennies, "Thermal expansion of the LiF(001) surface," *Surf. Sci.*, vol. 563, no. 1–3, pp. 127–134, Aug. 2004, doi: 10.1016/j.susc.2004.06.147.

[113] W. G. Wyckoff, "Crystal Structures," *Wiley*, vol. Vol. 1, 1968.

[114] F. Bernardini and V. Fiorentini, "Electronic dielectric constants of insulators calculated by the polarization method," *Phys. Rev. B*, vol. 58, no. 23, pp. 15292–15295, Dec. 1998, doi: 10.1103/PhysRevB.58.15292.

[115] M. Guo, X. Zhang, H. Gu, and N. Wang, "Ab initio calculations of electronic and optical properties in O-doped LiF crystal," *Open Phys.*, vol. 6, no. 2, Jan. 2008, doi: 10.2478/s11534-008-0007-3.

[116] E. L. Shirley, L. J. Terminello, J. E. Klepeis, and F. J. Himpsel, "Detailed theoretical photoelectron angular distributions for LiF(100)," *Phys. Rev. B*, vol. 53, no. 15, pp. 10296–10309, Apr. 1996, doi: 10.1103/PhysRevB.53.10296.

[117] D. M. Roessler and W. C. Walker, "Electronic spectrum of crystalline lithium fluoride," *J. Phys. Chem. Solids*, vol. 28, no. 8, pp. 1507–1515, Aug. 1967, doi: 10.1016/0022-3697(67)90280-6.

[118] M. Piacentini, D. W. Lynch, and C. G. Olson, "Thermoreflectance of LiF between 12 and 30 eV," *Phys. Rev. B*, vol. 13, no. 12, pp. 5530–5543, Jun. 1976, doi: 10.1103/PhysRevB.13.5530.

[119] F. J. Himpsel, L. J. Terminello, D. A. Lapiano-Smith, E. A. Eklund, and J. J. Barton, "Band Dispersion of Localized Valence States in LiF(100)," *Phys. Rev. Lett.*, vol. 68, no. 24, pp.

3611–3614, Jun. 1992, doi: 10.1103/PhysRevLett.68.3611.

[120] A. V. Petrov, N. S. Tsypkina, and V. E. Seleznev, *High Temp.- High. Press*, vol. 8, 536, 1976.

[121] B. K. Singh, M. K. Roy, V. J. Menon, and K. C. Sood, “Effects of dispersion, correction term, and isotopes on the thermal conductivity of LiF crystal,” *Phys. Rev. B*, vol. 67, no. 1, p. 14302, Jan. 2003, doi: 10.1103/PhysRevB.67.014302.

[122] P. D. Pathak and N. G. Vasavada, “Thermal expansion of LiF by X-ray diffraction and the temperature variation of its frequency spectrum,” *Acta Crystallogr. Sect. A*, vol. 28, no. 1, pp. 30–33, Jan. 1972, doi: 10.1107/S0567739472000063.

[123] G.Simmons and H. Wang, *Single Crystal Elastic Constants and Calculated Aggregate Properties Handbook, Second Edition*. 1971.

[124] A. E. Gheribi and P. Chartrand, “Application of the CALPHAD method to predict the thermal conductivity in dielectric and semiconductor crystals,” *Calphad*, vol. 39, pp. 70–79, Dec. 2012, doi: 10.1016/j.calphad.2012.06.002.

[125] A. J. Cohen and R. G. Gordon, “Theory of the lattice energy, equilibrium structure, elastic constants, and pressure-induced phase transitions in alkali-halide crystals,” *Phys. Rev. B*, vol. 12, no. 8, pp. 3228–3241, Oct. 1975, doi: 10.1103/PhysRevB.12.3228.

[126] X. Yang, T. Feng, J. Li, and X. Ruan, “Stronger role of four-phonon scattering than three-phonon scattering in thermal conductivity of III-V semiconductors at room temperature,” *Phys. Rev. B*, vol. 100, no. 24, p. 245203, Dec. 2019, doi: 10.1103/PhysRevB.100.245203.

[127] J. L. Verble, J. L. Warren, and J. L. Yarnell, “Lattice Dynamics of Lithium Hydride,” *Phys. Rev.*, vol. 168, no. 3, pp. 980–989, Apr. 1968, doi: 10.1103/PhysRev.168.980.

[128] F. E. Pretzel, G. N. Rupert, C. L. Mader, E. K. Storms, G. V. Gritton, and C. C. Rushing, “Properties of lithium hydride I. Single crystals,” *J. Phys. Chem. Solids*, vol. 16, no. 1–2, pp. 10–20, Nov. 1960, doi: 10.1016/0022-3697(60)90064-0.

[129] M. H. Brodsky and E. Burstein, “Infrared lattice vibrations of single crystal lithium hydride and some of its isotopic derivations,” *J. Phys. Chem. Solids*, vol. 28, no. 9, pp. 1655–1668,

Sep. 1967, doi: 10.1016/0022-3697(67)90139-4.

[130] G. Lucovsky, R. M. Martin, and E. Burstein, “Localized Effective Charges in Diatomic Crystals,” *Phys. Rev. B*, vol. 4, no. 4, pp. 1367–1374, Aug. 1971, doi: 10.1103/PhysRevB.4.1367.

[131] D. K. Blat, N. E. Zein, and V. I. Zinenko, “Calculations of phonon frequencies and dielectric constants of alkali hydrides via the density functional method,” *J. Phys. Condens. Matter*, vol. 3, no. 29, pp. 5515–5524, Jul. 1991, doi: 10.1088/0953-8984/3/29/006.

[132] R. H. Lyddane, R. G. Sachs, and E. Teller, “On the Polar Vibrations of Alkali Halides,” *Phys. Rev.*, vol. 59, no. 8, pp. 673–676, Apr. 1941, doi: 10.1103/PhysRev.59.673.

[133] D. Laplaze, “Étude expérimentale de LiH, LiD ; spectres de réflexion infrarouge et spectres de diffusion Raman du second ordre,” *J. Phys.*, vol. 37, no. 9, pp. 1051–1059, 1976, doi: 10.1051/jphys:019760037090105100.

[134] M. J. van Setten, V. A. Popa, G. A. de Wijs, and G. Brocks, “Electronic structure and optical properties of lightweight metal hydrides,” *Phys. Rev. B*, vol. 75, no. 3, p. 35204, Jan. 2007, doi: 10.1103/PhysRevB.75.035204.

[135] X. Yang, Y. Zhao, Z. Dai, M. Zulfiqar, J. Zhu, and J. Ni, “Thermal expansion induced reduction of lattice thermal conductivity in light crystals,” *Phys. Lett. A*, vol. 381, no. 40, pp. 3514–3518, Oct. 2017, doi: 10.1016/j.physleta.2017.08.061.

[136] C. E. Messer, “A SURVEY REPORT ON LITHIUM HYDRIDE,” U.S. Atomic Energy Commission, Oct. 1960. doi: 10.2172/4062196.

[137] J. L. Anderson, J. Nasise, K. Phllipson, and F. E. Pretzel (deceased), “Isotopic effects on the thermal expansion of lithium hydride,” *J. Phys. Chem. Solids*, vol. 31, no. 4, pp. 613–618, Apr. 1970, doi: 10.1016/0022-3697(70)90195-2.

[138] G. Roma, C. M. Bertoni, and S. Baroni, “The phonon spectra of LiH and LiD from density-functional perturbation theory,” *Solid State Commun.*, vol. 98, no. 3, pp. 203–207, Apr. 1996, doi: 10.1016/0038-1098(96)00067-1.

[139] Y. Kondo and K. Asaumi, “Effect of Pressure on the Direct Energy Gap of LiH,” *J. Phys.*

Soc. Japan, vol. 57, no. 1, pp. 367–371, Jan. 1988, doi: 10.1143/JPSJ.57.367.

[140] V. G. Plekhanov, “Wannier-Mott excitons in isotope-disordered crystals,” *Reports Prog. Phys.*, vol. 61, no. 8, pp. 1045–1097, Aug. 1998, doi: 10.1088/0034-4885/61/8/003.

[141] J. B. Vetrano, “Batelle Memorial Institute (unpublished), quoted by C. E. Messer and T. B. P. Gibb, Jr.,” 1957.

[142] G. A. Slack, “Nonmetallic crystals with high thermal conductivity,” *J. Phys. Chem. Solids*, vol. 34, no. 2, pp. 321–335, Jan. 1973, doi: 10.1016/0022-3697(73)90092-9.

[143] B. Yates, G. H. Wostenholm, and J. L. Bingham, “The Specific Heats of 7LiH and 7LiD at Low Temperatures,” *J. Phys. C Solid State Phys.*, vol. 7, no. 10, pp. 1769–1778, May 1974, doi: 10.1088/0022-3719/7/10/005.

[144] A. K. M. A. Islam, E. Haque, and A. S. Azad, “Crystal anharmonicity in Li(H,D) and Na(H,D) systems,” *Phys. status solidi*, vol. 183, no. 1, pp. 117–129, May 1994, doi: 10.1002/pssb.2221830108.

[145] D. Gerlich and C. S. Smith, “The pressure and temperature derivatives of the elastic moduli of lithium hydride,” *J. Phys. Chem. Solids*, vol. 35, no. 12, pp. 1587–1592, Jan. 1974, doi: 10.1016/S0022-3697(74)80167-8.

[146] D. G. R. William D. Callister Jr., *Fundamentals of Materials Science and Engineering*. 2018.

[147] V. G. Plekhanov, *Isotope Effects in Solid State Physics*. 2001.

[148] W. P. Mason, Ed., *Physical Acoustics: Principles and Methods*. 1964.

[149] J. P. Wolfe, *Imaging Phonons*. Cambridge University Press, 1998. doi: 10.1017/CBO9780511665424.

[150] J. Y. Zhang *et al.*, “A first-principles study of electron–phonon coupling in electron-doped LiH,” *J. Phys. Condens. Matter*, vol. 19, no. 42, p. 425218, Oct. 2007, doi: 10.1088/0953-8984/19/42/425218.

[151] J. Hama, K. Suito, and N. Kawakami, “First-principles calculation of the shock-wave equation of state of isotopic lithium hydrides,” *Phys. Rev. B*, vol. 39, no. 5, pp. 3351–3360,

Feb. 1989, doi: 10.1103/PhysRevB.39.3351.

[152] Y. Bouhadda, A. Rabehi, and S. Bezzari-Tahar-Chaouche, “First-principle calculation of MgH2 and LiH for hydrogen storage First-principle calculation of MgH 2 and LiH for hydrogen storage,” 2007. [Online]. Available: https://www.researchgate.net/publication/228959191

[153] J. M. Besson, G. Weill, G. Hamel, R. J. Nelmes, J. S. Loveday, and S. Hull, “Equation of state of lithium deuteride from neutron diffraction under high pressure,” *Phys. Rev. B*, vol. 45, no. 6, pp. 2613–2619, Feb. 1992, doi: 10.1103/PhysRevB.45.2613.

[154] E. Haque and A. K. M. A. Islam, “Hydrides and Deuterides of Lithium and Sodium. I. Model Potentials and Their Use in Perfect Lattice,” *Phys. status solidi*, vol. 158, no. 2, pp. 457–468, Apr. 1990, doi: 10.1002/pssb.2221580206.

[155] R. Pandey and A. M. Stoneham, “Intrinsic defect energies of lithium hydride and lithium deuteride crystals,” *J. Phys. C Solid State Phys.*, vol. 18, no. 27, pp. 5289–5297, Sep. 1985, doi: 10.1088/0022-3719/18/27/015.

[156] W. Dyck, “Lattice dynamics of alkali hydrides and euterides with the NaCl type structure,” *J. Phys. C Solid State Phys.*, vol. 14, no. 29, pp. 4193–4215, Oct. 1981, doi: 10.1088/0022-3719/14/29/008.

[157] Y. Zhao *et al.*, “High thermopower and potential thermoelectric properties of crystalline LiH and NaH,” *Phys. Rev. B*, vol. 95, no. 1, p. 14307, Jan. 2017, doi: 10.1103/PhysRevB.95.014307.

[158] X. Ke and I. Tanaka, “Decomposition Reactions for NaAlH4, Na3AlH6, and NaH: First-Principles Study,” *Phys. Rev. B*, vol. 71, no. 2, p. 24117, Jan. 2005, doi: 10.1103/PhysRevB.71.024117.

[159] X.-W. Sun, L.-C. Cai, Q.-F. Chen, X.-R. Chen, and F.-Q. Jing, “Structural, thermodynamic, electronic, and optical properties of NaH from first-principles calculations,” *Mater. Chem. Phys.*, vol. 133, no. 1, pp. 346–355, Mar. 2012, doi: 10.1016/j.matchemphys.2012.01.036.

[160] T. D. Humphries, D. A. Sheppard, M. R. Rowles, M. V. Sofianos, and C. E. Buckley, “Fluoride substitution in sodium hydride for thermal energy storage applications,” *J. Mater.*

Chem. A, vol. 4, no. 31, pp. 12170–12178, 2016, doi: 10.1039/C6TA03623F.

[161] J. L. Martins, “Equations of state of alkali hydrides at high pressures,” *Phys. Rev. B*, vol. 41, no. 11, pp. 7883–7886, Apr. 1990, doi: 10.1103/PhysRevB.41.7883.

[162] S. Lebègue, B. Arnaud, M. Alouani, and P. E. Bloechl, “Implementation of an all-electron GW approximation based on the projector augmented wave method without plasmon pole approximation: Application to Si, SiC, AlAs, InAs, NaH, and KH,” *Phys. Rev. B*, vol. 67, no. 15, p. 155208, Apr. 2003, doi: 10.1103/PhysRevB.67.155208.

[163] J. E. Bird, T. D. Humphries, M. Paskevicius, L. Poupin, and C. E. Buckley, “Thermal properties of thermochemical heat storage materials,” *Phys. Chem. Chem. Phys.*, vol. 22, no. 8, pp. 4617–4625, 2020, doi: 10.1039/C9CP05940G.

[164] W. M. Haynes *et al.*, “CRC Handbook of Chemistry and Physics Internet Version 2016 Editor-in-Chief Associate Editor.”

[165] D. R. Lide, *CRC Handbook of Chemistry and Physics: A Ready Reference Book of Chemical and Physical Data* . 2004.

[166] C. G. Shull, E. O. Wollan, G. A. Morton, and W. L. Davidson, “Neutron Diffraction Studies of NaH and NaD,” *Phys. Rev.*, vol. 73, no. 8, pp. 842–847, Apr. 1948, doi: 10.1103/PhysRev.73.842.

[167] D. G. Pettifor, M. Aoki, J. N. Murrell, A. Cottrell, and A. M. Stoneham, “Bonding and structure of intermetallics: a new bond order potential,” *Philos. Trans. R. Soc. London. Ser. A Phys. Eng. Sci.*, vol. 334, no. 1635, pp. 439–449, 1991, doi: 10.1098/rsta.1991.0024.

[168] S. F. Pugh, “XCII. Relations between the elastic moduli and the plastic properties of polycrystalline pure metals,” *London, Edinburgh, Dublin Philos. Mag. J. Sci.*, vol. 45, no. 367, pp. 823–843, Aug. 1954, doi: 10.1080/14786440808520496.

[169] M. Chauhan and D. C. Gupta, “Electronic, mechanical, phase transition and thermo-physical properties of TiC, ZrC and HfC: High pressure computational study,” *Diam. Relat. Mater.*, vol. 40, pp. 96–106, Nov. 2013, doi: 10.1016/j.diamond.2013.10.011.

[170] A. N. Cleland, *Foundations of Nanomechanics*. Berlin, Heidelberg: Springer Berlin

Heidelberg, 2003. doi: 10.1007/978-3-662-05287-7.

[171] X.-W. Sun, Q.-F. Chen, X.-R. Chen, L.-C. Cai, and F.-Q. Jing, "Ab initio study of phase transition and bulk modulus of NaH," *J. Solid State Chem.*, vol. 184, no. 2, pp. 427–431, Feb. 2011, doi: 10.1016/j.jssc.2010.12.019.

[172] J. G. O. Ojwang, R. van Santen, G. J. Kramer, A. C. T. van Duin, and W. A. Goddard, "Modeling the sorption dynamics of NaH using a reactive force field," *J. Chem. Phys.*, vol. 128, no. 16, p. 164714, Apr. 2008, doi: 10.1063/1.2908737.

[173] S. J. Duclos, Y. K. Vohra, A. L. Ruoff, S. Filipek, and B. Baranowski, "High-pressure studies of NaH to 54 GPa," *Phys. Rev. B*, vol. 36, no. 14, pp. 7664–7667, Nov. 1987, doi: 10.1103/PhysRevB.36.7664.

[174] H. D. Hochheimer, K. Strössner, W. Hönle, B. Baranowski, and F. Filipek, "High pressure X-ray investigation of the alkali hydrides NaH, KH, RbH and CsH," *J. Less Common Met.*, vol. 107, no. 2, pp. L13–L14, May 1985, doi: 10.1016/0022-5088(85)90097-9.

[175] S. Huberman, C. Zhang, and J. Abou Haibeh, "On the question of second sound in germanium: A theoretical viewpoint," 2022.

[176] C. Xie, C. Mak, X. Tao, and F. Yan, "Photodetectors Based on Two-Dimensional Layered Materials Beyond Graphene," *Adv. Funct. Mater.*, vol. 27, no. 19, p. 1603886, May 2017, doi: 10.1002/adfm.201603886.

[177] J.-B. Wu, M.-L. Lin, X. Cong, H.-N. Liu, and P.-H. Tan, "Raman spectroscopy of graphene-based materials and its applications in related devices," *Chem. Soc. Rev.*, vol. 47, no. 5, pp. 1822–1873, 2018, doi: 10.1039/C6CS00915H.

[178] X. Yu, H. Cheng, M. Zhang, Y. Zhao, L. Qu, and G. Shi, "Graphene-based smart materials," *Nat. Rev. Mater.*, vol. 2, no. 9, p. 17046, Sep. 2017, doi: 10.1038/natrevmats.2017.46.

[179] S. V. Morozov *et al.*, "Giant Intrinsic Carrier Mobilities in Graphene and Its Bilayer," *Phys. Rev. Lett.*, vol. 100, no. 1, p. 16602, Jan. 2008, doi: 10.1103/PhysRevLett.100.016602.

[180] J.-H. Chen, C. Jang, S. Xiao, M. Ishigami, and M. S. Fuhrer, "Intrinsic and extrinsic performance limits of graphene devices on SiO2," *Nat. Nanotechnol.*, vol. 3, no. 4, pp. 206–

209, Apr. 2008, doi: 10.1038/nnano.2008.58.

[181] I. Meric, M. Y. Han, A. F. Young, B. Ozyilmaz, P. Kim, and K. L. Shepard, "Current saturation in zero-bandgap, top-gated graphene field-effect transistors," *Nat. Nanotechnol.*, vol. 3, no. 11, pp. 654–659, Nov. 2008, doi: 10.1038/nnano.2008.268.

[182] E. McCann and M. Koshino, "The electronic properties of bilayer graphene," *Reports Prog. Phys.*, vol. 76, no. 5, p. 56503, May 2013, doi: 10.1088/0034-4885/76/5/056503.

[183] F. Wang *et al.*, "Gate-Variable Optical Transitions in Graphene," *Science (80-.).*, vol. 320, no. 5873, pp. 206–209, Apr. 2008, doi: 10.1126/science.1152793.

[184] K. F. Mak, M. Y. Sfeir, Y. Wu, C. H. Lui, J. A. Misewich, and T. F. Heinz, "Measurement of the Optical Conductivity of Graphene," *Phys. Rev. Lett.*, vol. 101, no. 19, p. 196405, Nov. 2008, doi: 10.1103/PhysRevLett.101.196405.

[185] F. Kadi and E. Malic, "Optical properties of Bernal-stacked bilayer graphene: A theoretical study," *Phys. Rev. B*, vol. 89, no. 4, p. 45419, Jan. 2014, doi: 10.1103/PhysRevB.89.045419.

[186] M. De Corato, C. Cocchi, D. Prezzi, M. J. Caldas, E. Molinari, and A. Ruini, "Optical Properties of Bilayer Graphene Nanoflakes," *J. Phys. Chem. C*, vol. 118, no. 40, pp. 23219–23225, Oct. 2014, doi: 10.1021/jp504222m.

[187] B.-L. Huang, C.-P. Chuu, and M.-F. Lin, "Asymmetry-enriched electronic and optical properties of bilayer graphene," *Sci. Rep.*, vol. 9, no. 1, p. 859, Dec. 2019, doi: 10.1038/s41598-018-37058-9.

[188] I. W. Frank, D. M. Tanenbaum, A. M. van der Zande, and P. L. McEuen, "Mechanical properties of suspended graphene sheets," *J. Vac. Sci. Technol. B Microelectron. Nanom. Struct.*, vol. 25, no. 6, p. 2558, 2007, doi: 10.1116/1.2789446.

[189] C. Lee, X. Wei, J. W. Kysar, and J. Hone, "Measurement of the Elastic Properties and Intrinsic Strength of Monolayer Graphene," *Science (80-.).*, vol. 321, no. 5887, pp. 385–388, Jul. 2008, doi: 10.1126/science.1157996.

[190] Y. Y. Zhang, C. M. Wang, Y. Cheng, and Y. Xiang, "Mechanical properties of bilayer graphene sheets coupled by sp3 bonding," *Carbon N. Y.*, vol. 49, no. 13, pp. 4511–4517,

Nov. 2011, doi: 10.1016/j.carbon.2011.06.058.

[191] A. Liu and Q. Peng, “A Molecular Dynamics Study of the Mechanical Properties of Twisted Bilayer Graphene,” *Micromachines*, vol. 9, no. 9, p. 440, Aug. 2018, doi: 10.3390/mi9090440.

[192] J. B. Oostinga, H. B. Heersche, X. Liu, A. F. Morpurgo, and L. M. K. Vandersypen, “Gate-induced insulating state in bilayer graphene devices,” *Nat. Mater.*, vol. 7, no. 2, pp. 151–157, Feb. 2008, doi: 10.1038/nmat2082.

[193] Y. Cao *et al.*, “Unconventional superconductivity in magic-angle graphene superlattices,” *Nature*, vol. 556, no. 7699, pp. 43–50, Apr. 2018, doi: 10.1038/nature26160.

[194] A. C. Gadelha *et al.*, “Twisted Bilayer Graphene: A Versatile Fabrication Method and the Detection of Variable Nanometric Strain Caused by Twist-Angle Disorder,” *ACS Appl. Nano Mater.*, vol. 4, no. 2, pp. 1858–1866, Feb. 2021, doi: 10.1021/acsanm.0c03230.

[195] S. Lee, D. Broido, K. Esfarjani, and G. Chen, “Hydrodynamic phonon transport in suspended graphene,” *Nat. Commun.*, vol. 6, no. 1, p. 6290, May 2015, doi: 10.1038/ncomms7290.

[196] A. Cepellotti, G. Fugallo, L. Paulatto, M. Lazzeri, F. Mauri, and N. Marzari, “Phonon hydrodynamics in two-dimensional materials,” *Nat. Commun.*, vol. 6, no. 1, p. 6400, May 2015, doi: 10.1038/ncomms7400.

[197] Z. Ding *et al.*, “Phonon Hydrodynamic Heat Conduction and Knudsen Minimum in Graphite,” *Nano Lett.*, vol. 18, no. 1, pp. 638–649, Jan. 2018, doi: 10.1021/acs.nanolett.7b04932.

[198] Y. Kuang, L. Lindsay, S. Shi, X. Wang, and B. Huang, “Thermal conductivity of graphene mediated by strain and size,” *Int. J. Heat Mass Transf.*, vol. 101, pp. 772–778, Oct. 2016, doi: 10.1016/j.ijheatmasstransfer.2016.05.072.

[199] F. Duan, C. Shen, H. Zhang, and G. Qin, “Hydrodynamically enhanced thermal transport due to strong interlayer interactions: A case study of strained bilayer graphene,” *Phys. Rev. B*, vol. 105, no. 12, p. 125406, Mar. 2022, doi: 10.1103/PhysRevB.105.125406.

[200] H. Min, B. Sahu, S. K. Banerjee, and A. H. MacDonald, “Ab initio theory of gate induced gaps in graphene bilayers,” *Phys. Rev. B*, vol. 75, no. 15, p. 155115, Apr. 2007, doi: 10.1103/PhysRevB.75.155115.

[201] A. M. Popov *et al.*, “AA stacking, tribological and electronic properties of double-layer graphene with krypton spacer,” *J. Chem. Phys.*, vol. 139, no. 15, p. 154705, Oct. 2013, doi: 10.1063/1.4824298.

[202] Y. Fukaya, Y. Zhao, H.-W. Kim, J. R. Ahn, H. Fukidome, and I. Matsuda, “Atomic arrangements of quasicrystal bilayer graphene: Interlayer distance expansion,” *Phys. Rev. B*, vol. 104, no. 18, p. L180202, Nov. 2021, doi: 10.1103/PhysRevB.104.L180202.

[203] C. H. Lui *et al.*, “Observation of Layer-Breathing Mode Vibrations in Few-Layer Graphene through Combination Raman Scattering,” *Nano Lett.*, vol. 12, no. 11, pp. 5539–5544, Nov. 2012, doi: 10.1021/nl302450s.

[204] C. H. Lui and T. F. Heinz, “Measurement of layer breathing mode vibrations in few-layer graphene,” *Phys. Rev. B*, vol. 87, no. 12, p. 121404, Mar. 2013, doi: 10.1103/PhysRevB.87.121404.

[205] J. Maultzsch, S. Reich, C. Thomsen, H. Requardt, and P. Ordejón, “Phonon Dispersion in Graphite,” *Phys. Rev. Lett.*, vol. 92, no. 7, p. 75501, Feb. 2004, doi: 10.1103/PhysRevLett.92.075501.

[206] “Phonons in Bilayer Graphene,” 2013. [Online]. Available: http://tkea.com.ua/siet/archive/2013-t2/130.pdf

[207] E. L. Silva *et al.*, “Electronic and Phonon Instabilities in Bilayer Graphene under Applied External Bias,” *Mater. Today Proc.*, vol. 20, pp. 373–382, 2020, doi: 10.1016/j.matpr.2019.10.076.

[208] O. Dubay and G. Kresse, “Accurate density functional calculations for the phonon dispersion relations of graphite layer and carbon nanotubes,” *Phys. Rev. B*, vol. 67, no. 3, p. 35401, Jan. 2003, doi: 10.1103/PhysRevB.67.035401.

[209] L. Wirtz and A. Rubio, “The phonon dispersion of graphite revisited,” *Solid State Commun.*, vol. 131, no. 3–4, pp. 141–152, Jul. 2004, doi: 10.1016/j.ssc.2004.04.042.

[210] N. Mounet and N. Marzari, “First-principles determination of the structural, vibrational and thermodynamic properties of diamond, graphite, and derivatives,” *Phys. Rev. B*, vol. 71, no. 20, p. 205214, May 2005, doi: 10.1103/PhysRevB.71.205214.

[211] K. N. Onaiwu and J. O. A. Idiodi, “Effects of Pseudopotentials on the Phonon Dispersion of Graphene,” *IOSR J. Appl. Phys.*, vol. 6, no. 1, pp. 27–33, 2014, doi: 10.9790/4861-06122733.

[212] R. Nicklow, N. Wakabayashi, and H. G. Smith, “Lattice Dynamics of Pyrolytic Graphite,” *Phys. Rev. B*, vol. 5, no. 12, pp. 4951–4962, Jun. 1972, doi: 10.1103/PhysRevB.5.4951.

[213] C. Oshima, T. Aizawa, R. Souda, Y. Ishizawa, and Y. Sumiyoshi, “Surface phonon dispersion curves of graphite (0001) over the entire energy region,” *Solid State Commun.*, vol. 65, no. 12, pp. 1601–1604, Mar. 1988, doi: 10.1016/0038-1098(88)90660-6.

[214] R. . Nemanich, G. Lucovsky, and S. . Solin, “Optical probes of the lattice dynamics of graphite,” *Mater. Sci. Eng.*, vol. 31, pp. 157–160, Dec. 1977, doi: 10.1016/0025-5416(77)90029-5.

[215] R. A. Friedel and G. L. Carlson, “Infrared spectra of ground graphite,” *J. Phys. Chem.*, vol. 75, no. 8, pp. 1149–1151, Apr. 1971, doi: 10.1021/j100678a021.

[216] F. Tuinstra and J. L. Koenig, “Raman Spectrum of Graphite,” *J. Chem. Phys.*, vol. 53, no. 3, pp. 1126–1130, Aug. 1970, doi: 10.1063/1.1674108.

[217] D. L. Nika and A. A. Balandin, “Phonons and thermal transport in graphene and graphene-based materials,” *Reports Prog. Phys.*, vol. 80, no. 3, p. 36502, Mar. 2017, doi: 10.1088/1361-6633/80/3/036502.

[218] J. Jeong, X. Li, S. Lee, L. Shi, and Y. Wang, “Transient Hydrodynamic Lattice Cooling by Picosecond Laser Irradiation of Graphite,” *Phys. Rev. Lett.*, vol. 127, no. 8, p. 85901, Aug. 2021, doi: 10.1103/PhysRevLett.127.085901.

[219] L. Pitre, “The Comparison between a Second-Sound Thermometer and a Melting-Curve Thermometer from 0.8 K Down to 20 mK,” in *AIP Conference Proceedings*, 2003, vol. 684, pp. 101–106. doi: 10.1063/1.1627108.

[220] R. A. Sherlock and D. O. Edwards, “Oscillating Superleak Second Sound Transducers,” *Rev. Sci. Instrum.*, vol. 41, no. 11, pp. 1603–1609, Nov. 1970, doi: 10.1063/1.1684354.

APPENDICES

Appendix A-1: Convergence tests for Quantum ESPRESSO parameters (AA-bilayer graphene)

A-1.1: Kinetic energy cutoff (ecutwfc)

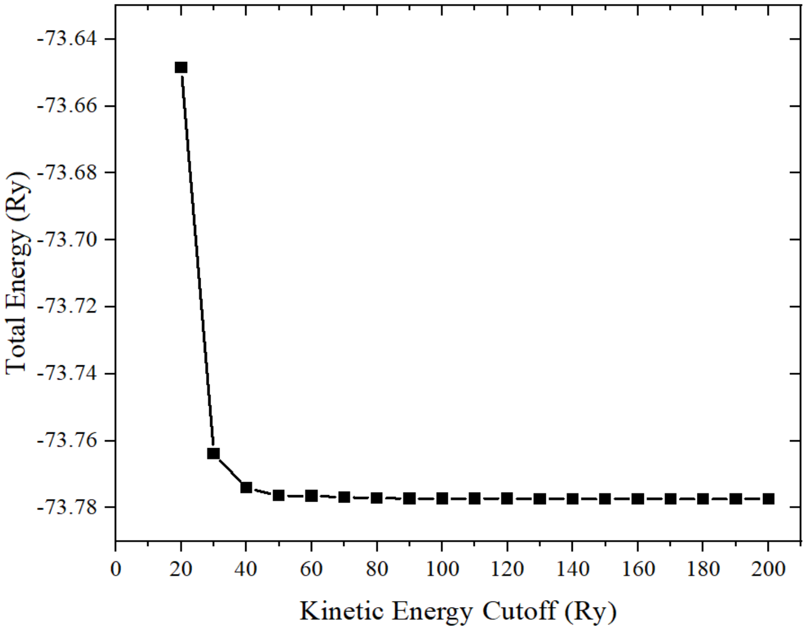

Figure A-1.1.1: Total energy vs kinetic energy cutoff.

A-1.2: K-points

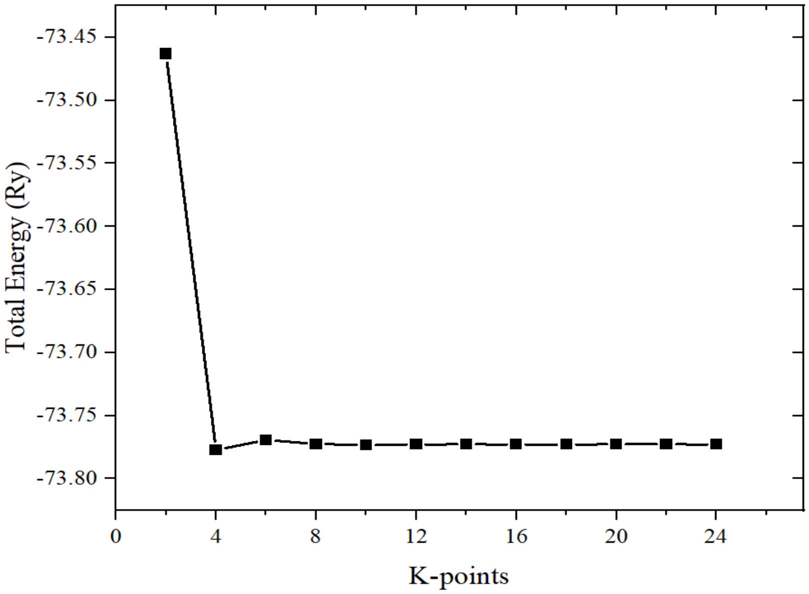

Figure A-1.2.1: Total energy vs κ-points.

Appendix A-2: The effect of selecting second-order supercell, third-order supercell, and cutoff parameter on thermal conductivity

Table A-2: Calculated lattice thermal conductivity at room temperature for NaH with scalebroad = 1.0 and 30x30x30 *q*-points grid at different second and third-order supercells and cutoff parameters. The selected thermal conductivity for each pseudopotential is in red.

Second-order supercell	Third-order supercell	Cutoff	Thermal conductivity (W.m^{-1}.K^{-1}) PBE	PBESOL	LDA
2×2×2	3×3×3	-2	6.18	6.86	10.94
2×2×2	3×3×3	-3	6.30	7.02	11.17
2×2×2	3×3×3	-4	6.22	7.12	11.73
2×2×2	3×3×3	-5	6.12	7.13	11.61
2×2×2	4×4×4	-3	6.48	7.18	11.26
2×2×2	4×4×4	-4	6.75	7.45	11.81
2×2×2	4×4×4	-5	6.96	7.71	12.30
3×3×3	3×3×3	-2	4.74	7.19	10.87
3×3×3	3×3×3	-3	4.82	7.38	11.13
3×3×3	3×3×3	-4	4.76	7.48	11.68
3×3×3	3×3×3	-5	4.66	7.49	11.62
3×3×3	4×4×4	-3	4.78	7.54	11.24
3×3×3	4×4×4	-4	**5.16**	7.83	11.76
3×3×3	4×4×4	-5	5.22	8.02	12.18
4×4×4	3×3×3	-2	4.68	**5.23**	9.12
4×4×4	3×3×3	-3	4.75	5.34	9.30
4×4×4	3×3×3	-4	4.70	5.41	9.74
4×4×4	3×3×3	-5	4.61	5.42	9.65
4×4×4	4×4×4	-3	4.81	5.46	9.38
4×4×4	4×4×4	-4	5.20	5.66	9.81
4×4×4	4×4×4	-5	5.24	5.83	10.14
6×6×6	3×3×3	-2	4.41	3.63	8.01
6×6×6	3×3×3	-3	4.46	3.62	8.11

6×6×6	3×3×3	-4	4.40	3.65	8.50
6×6×6	3×3×3	-5	4.32	3.63	8.43
6×6×6	4×4×4	-3	4.58	3.68	8.18
6×6×6	4×4×4	-4	4.76	3.79	8.56
6×6×6	4×4×4	-5	4.85	3.94	8.86
8×8×8	3×3×3	-2	4.77	2.75	**7.30**
8×8×8	3×3×3	-3	4.87	2.67	7.37
8×8×8	3×3×3	-4	4.82	2.68	7.72
8×8×8	3×3×3	-5	4.73	2.66	7.70
8×8×8	4×4×4	-3	4.88	2.71	7.42
8×8×8	4×4×4	-4	5.19	2.78	7.76
8×8×8	4×4×4	-5	5.30	2.89	8.05

Appendix A-3: Convergence for average scattering rate (Normal + Umklapp) and lattice thermal conductivity values

A-3.1: NaF

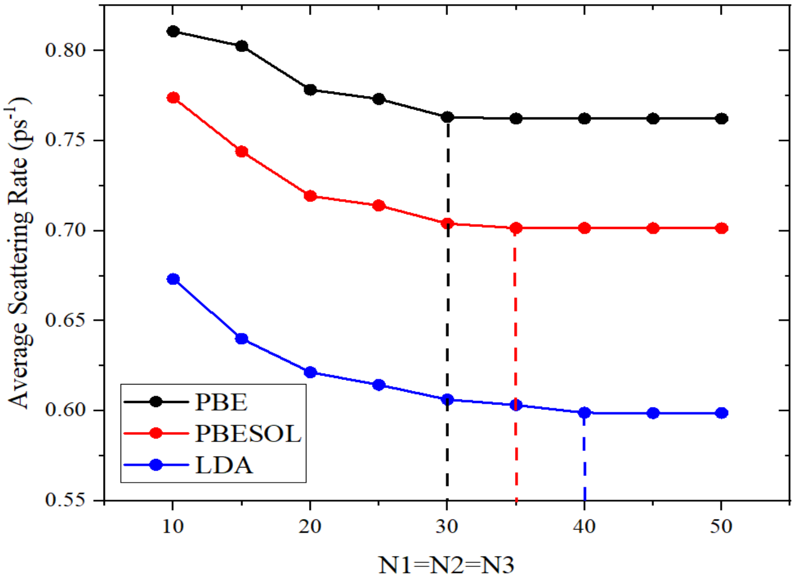

Figure A-3.1.1: Average scattering rate for different *q*-points numbers at *T* = 50 K for NaF. The selected grid for each pseudopotential is shown as a dashed vertical line.

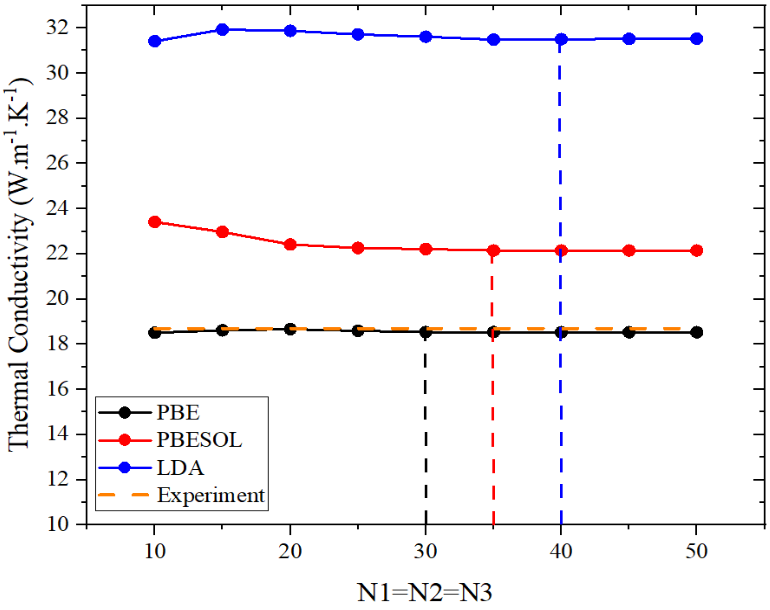

Figure A-3.1.2: Lattice thermal conductivity for different *q*-points numbers at *T* = 300 K for NaF. The experimental value [97] is shown as a dashed horizontal orange line. The selected grid for each pseudopotential is shown as a dashed vertical line.

A-3.2: LiF

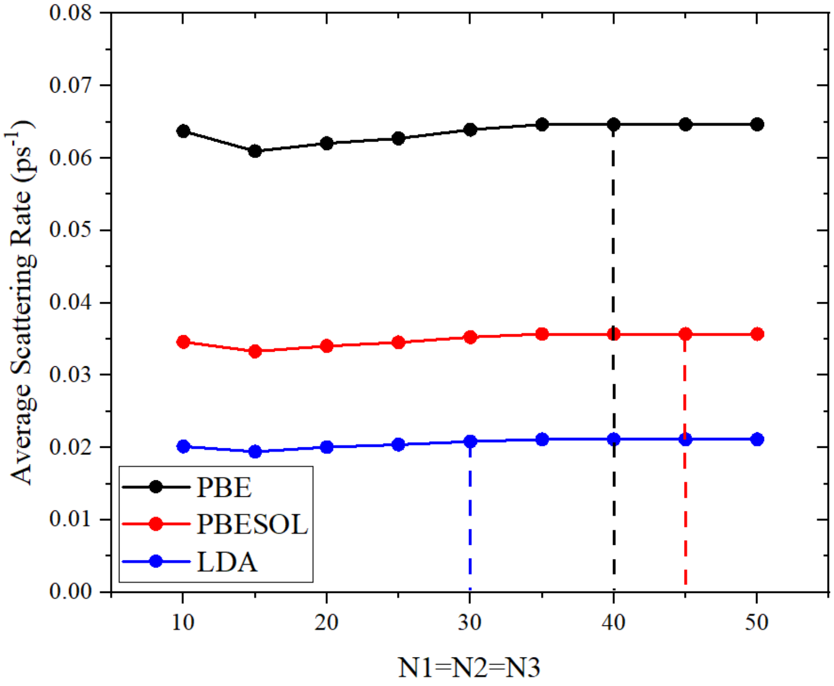

Figure A-3.2.1: Average scattering rate for different *q*-points numbers at *T* = 50 K for LiF. The selected grid for each pseudopotential is shown as a dashed vertical line.

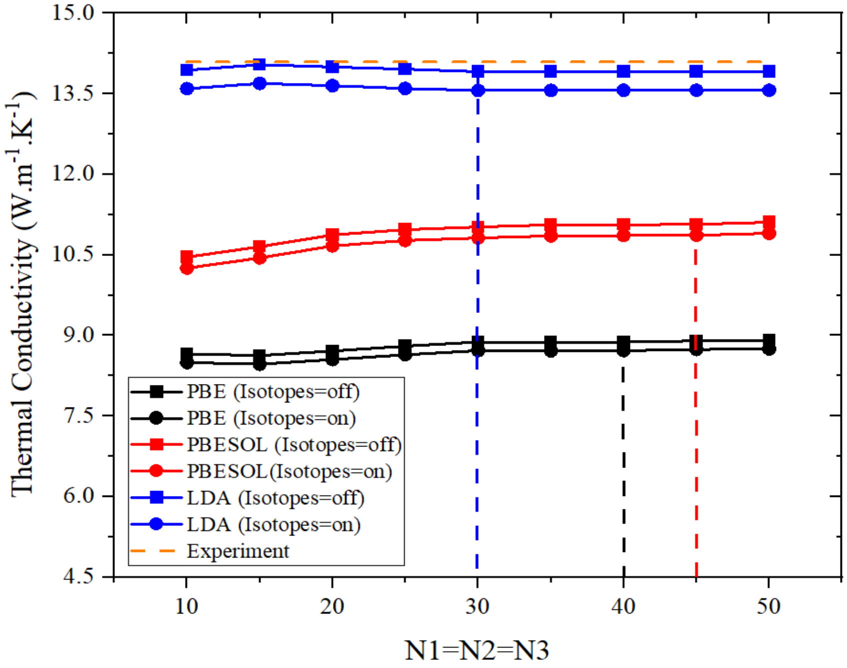

Figure A-3.2.2: Lattice thermal conductivity for different *q*-points numbers at *T* = 300 K for LiF. The experimental value [120] is shown as a dashed horizontal orange line. The selected grid for each pseudopotential is shown as a dashed vertical line.

A-3.3: LiH

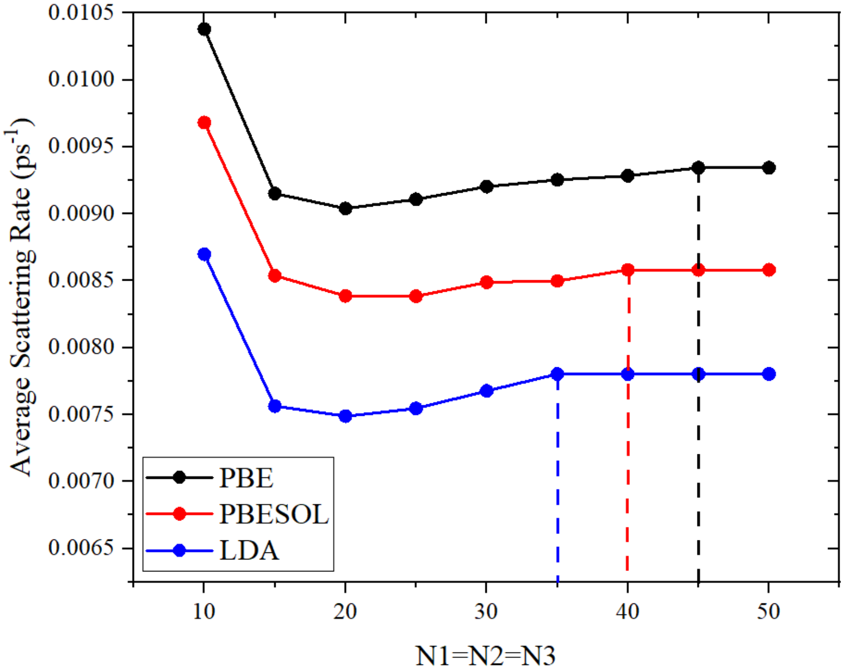

Figure A-3.3.1: Average scattering rate for different *q*-points numbers at *T* = 50 K for LiH. The selected grid for each pseudopotential is shown as a dashed vertical line.

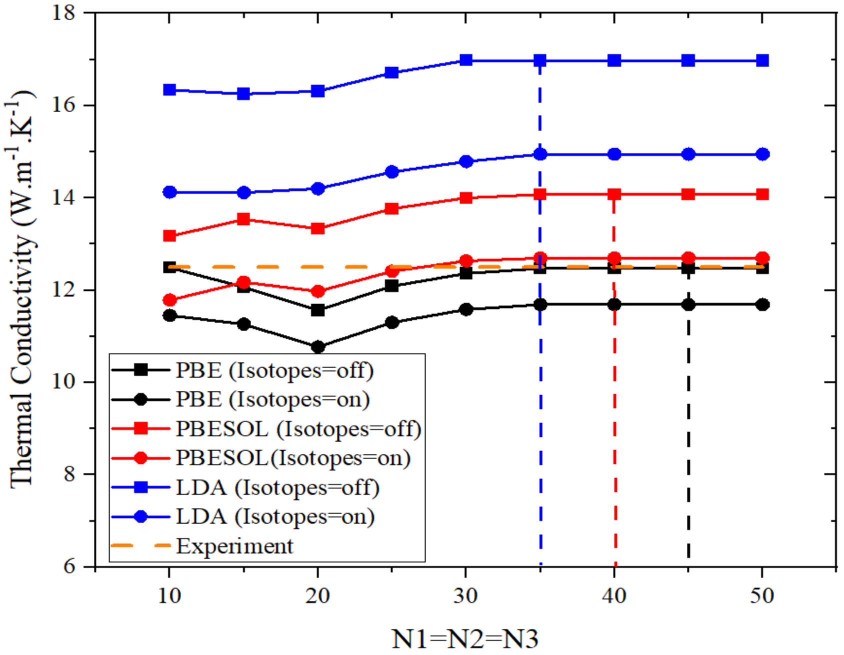

Figure A-3.3.2: Lattice thermal conductivity for different *q*-points numbers at *T* = 327 K for LiH. The experimental value [141] is shown as a dashed horizontal orange line. The selected grid for each pseudopotential is shown as a dashed vertical line.

A-3.4: NaH

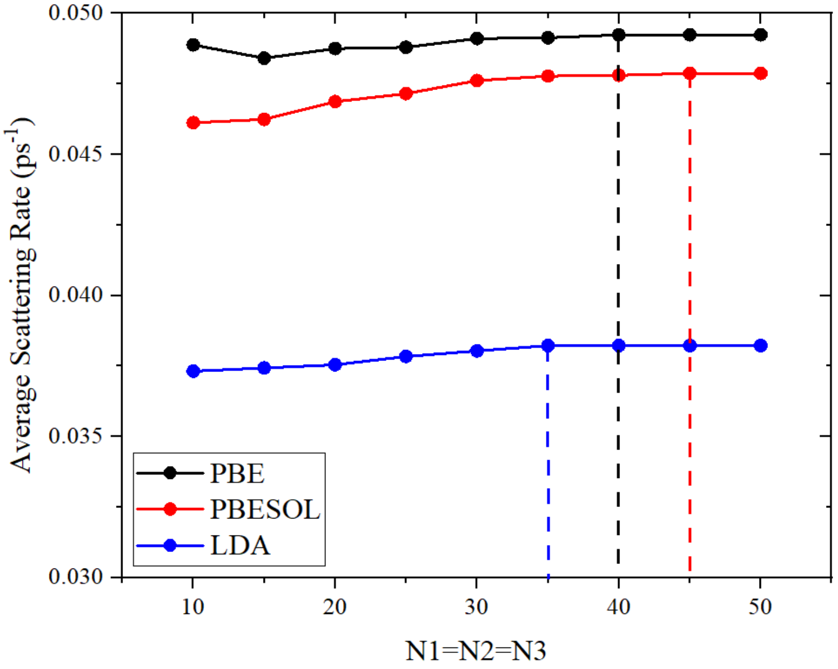

Figure A-3.4.1: Average scattering rate for different *q*-points numbers at *T* = 50 K for NaH. The selected grid for each pseudopotential is shown as a dashed vertical line.

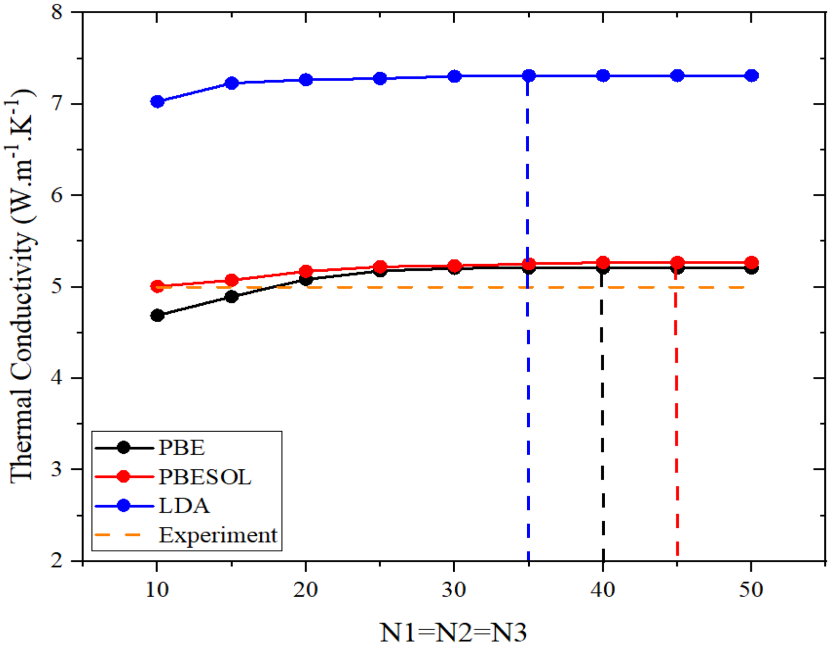

Figure A-3.4.2: Lattice thermal conductivity for different *q*-points numbers at *T* = 300 K for NaH. The experimental value [163] is shown as a dashed horizontal orange line. The selected grid for each pseudopotential is shown as a dashed vertical line.

Appendix A-4: Band structures

A-4.1: NaF

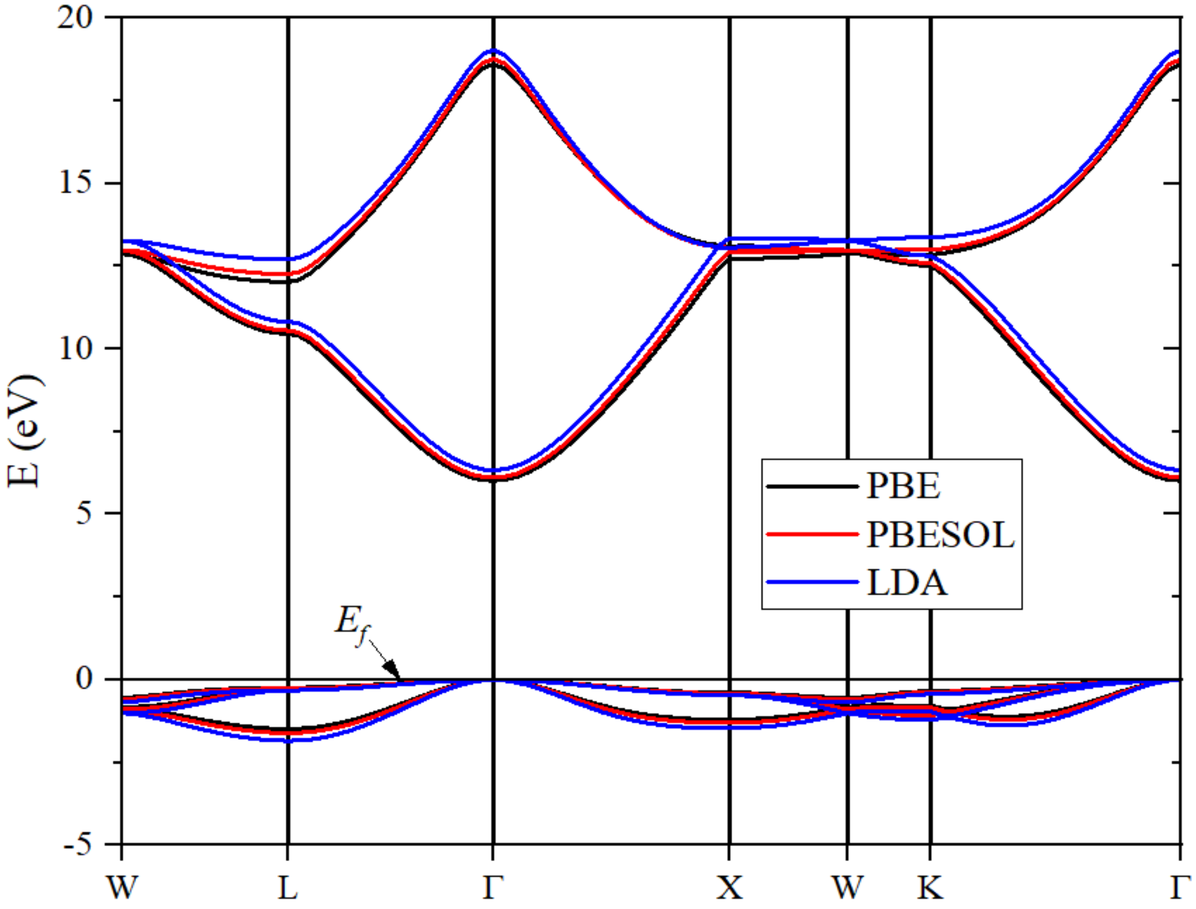

Figure A-4.1.1: Band structure of NaF.

A-4.2: LiF

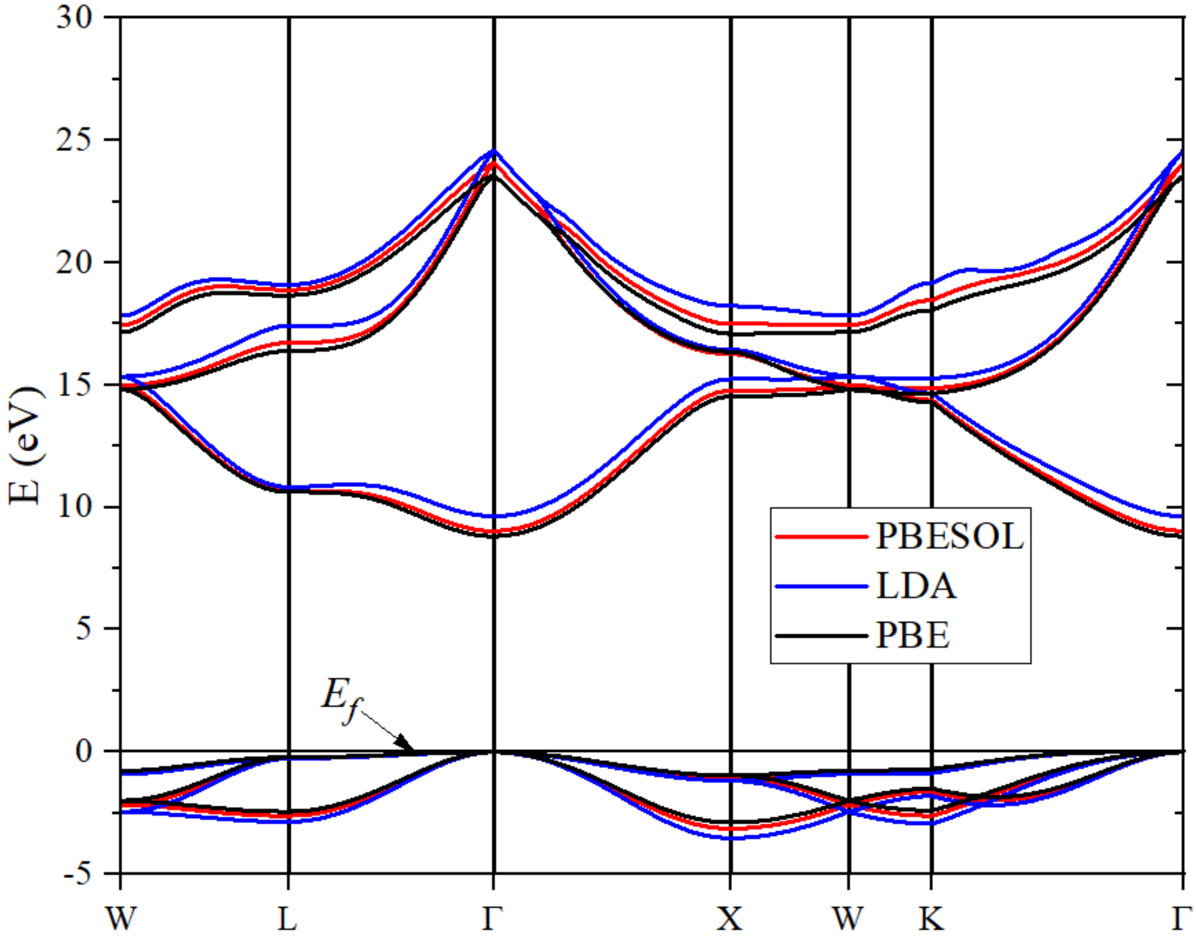

Figure A-4.2.1: Band structure of LiF.

A-4.3: LiH

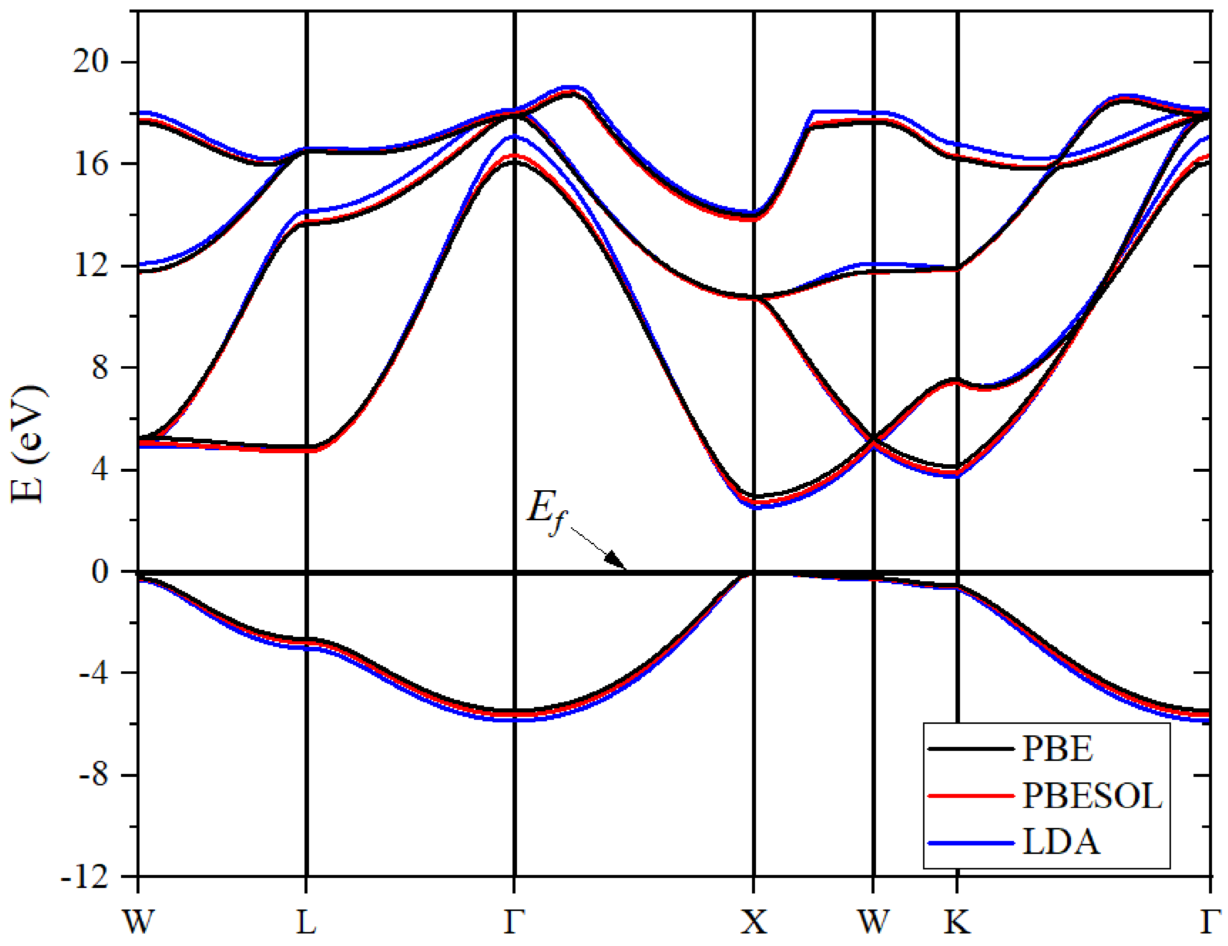

Figure A-4.3.1: Band structure of LiH.

A-4.4: NaH

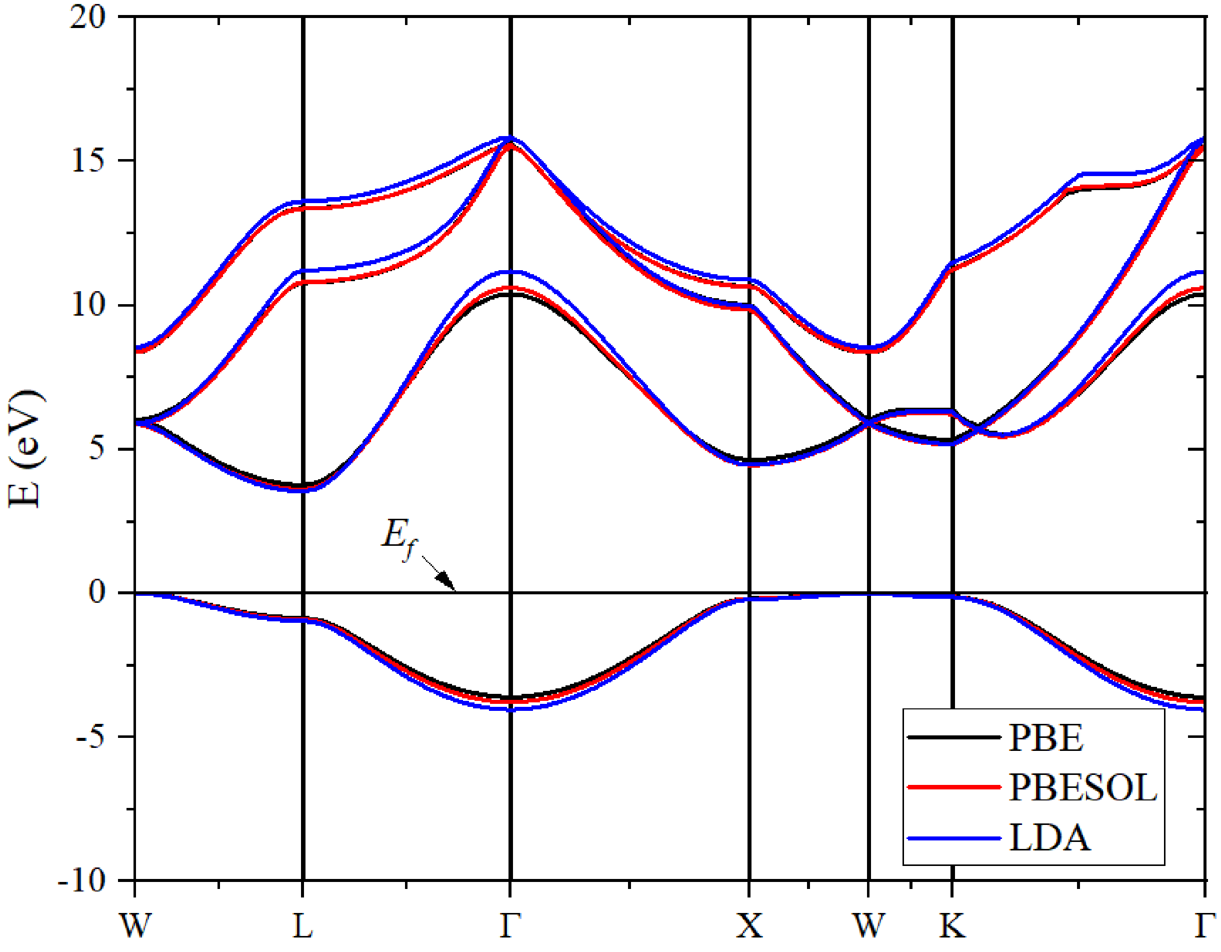

Figure A-4.4.1: Band structure of NaH.

Appendix A-5: Phonon hydrodynamics (Python code)

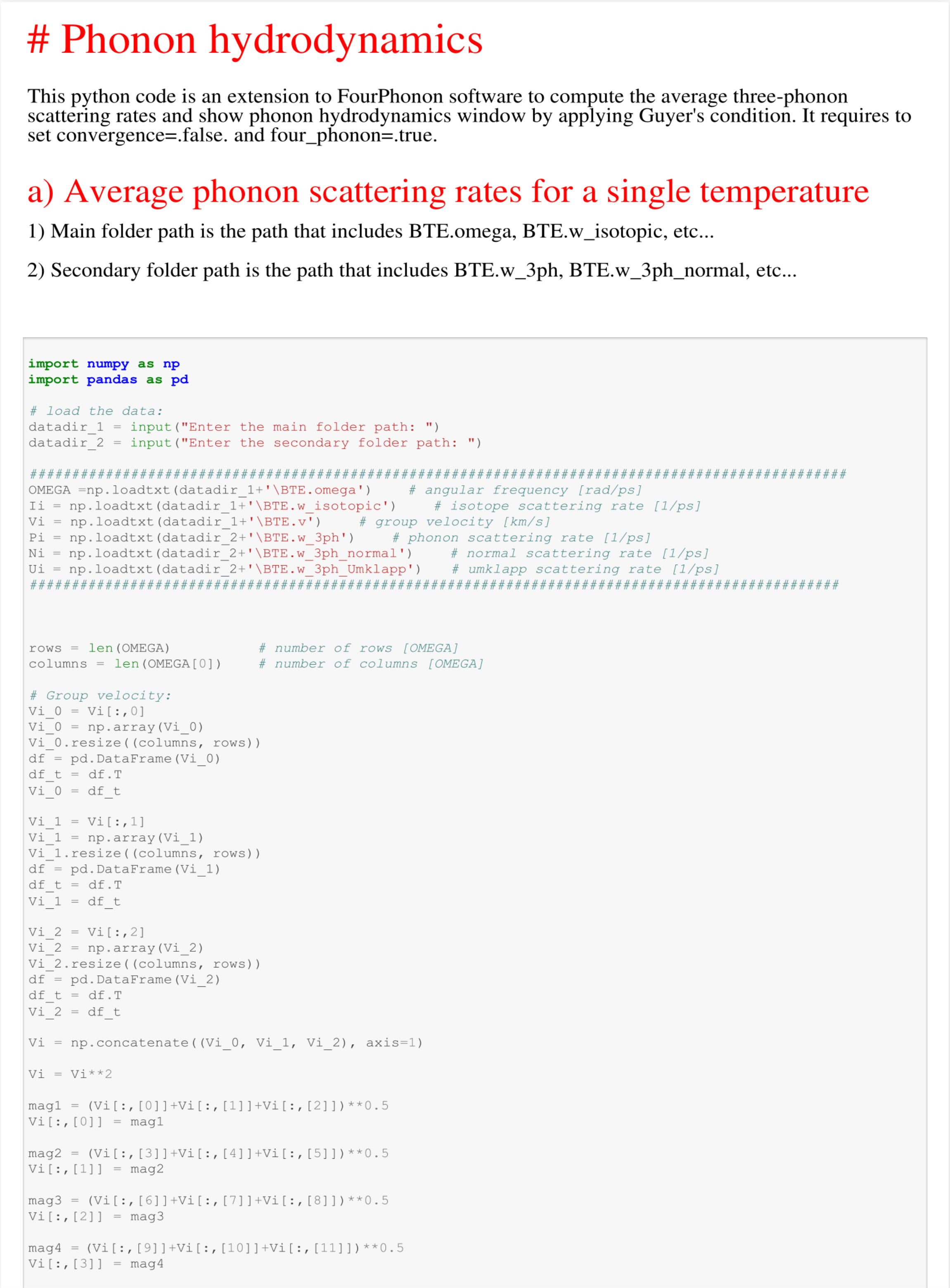

Phonon hydrodynamics

This python code is an extension to FourPhonon software to compute the average three-phonon scattering rates and show phonon hydrodynamics window by applying Guyer's condition. It requires to set convergence=.false. and four_phonon=.true.

a) Average phonon scattering rates for a single temperature

1) Main folder path is the path that includes BTE.omega, BTE.w_isotopic, etc...

2) Secondary folder path is the path that includes BTE.w_3ph, BTE.w_3ph_normal, etc...

```python
import numpy as np
import pandas as pd

# load the data:
datadir_1 = input("Enter the main folder path: ")
datadir_2 = input("Enter the secondary folder path: ")

#################################################################################################
OMEGA =np.loadtxt(datadir_1+'\BTE.omega')    # angular frequency [rad/ps]
Ii = np.loadtxt(datadir_1+'\BTE.w_isotopic')    # isotope scattering rate [1/ps]
Vi = np.loadtxt(datadir_1+'\BTE.v')    # group velocity [km/s]
Pi = np.loadtxt(datadir_2+'\BTE.w_3ph')     # phonon scattering rate [1/ps]
Ni = np.loadtxt(datadir_2+'\BTE.w_3ph_normal')     # normal scattering rate [1/ps]
Ui = np.loadtxt(datadir_2+'\BTE.w_3ph_Umklapp')    # umklapp scattering rate [1/ps]
################################################################################################



rows = len(OMEGA)           # number of rows [OMEGA]
columns = len(OMEGA[0])     # number of columns [OMEGA]

# Group velocity:
Vi_0 = Vi[:,0]
Vi_0 = np.array(Vi_0)
Vi_0.resize((columns, rows))
df = pd.DataFrame(Vi_0)
df_t = df.T
Vi_0 = df_t

Vi_1 = Vi[:,1]
Vi_1 = np.array(Vi_1)
Vi_1.resize((columns, rows))
df = pd.DataFrame(Vi_1)
df_t = df.T
Vi_1 = df_t

Vi_2 = Vi[:,2]
Vi_2 = np.array(Vi_2)
Vi_2.resize((columns, rows))
df = pd.DataFrame(Vi_2)
df_t = df.T
Vi_2 = df_t

Vi = np.concatenate((Vi_0, Vi_1, Vi_2), axis=1)

Vi = Vi**2

mag1 = (Vi[:,[0]]+Vi[:,[1]]+Vi[:,[2]])**0.5
Vi[:,[0]] = mag1

mag2 = (Vi[:,[3]]+Vi[:,[4]]+Vi[:,[5]])**0.5
Vi[:,[1]] = mag2

mag3 = (Vi[:,[6]]+Vi[:,[7]]+Vi[:,[8]])**0.5
Vi[:,[2]] = mag3

mag4 = (Vi[:,[9]]+Vi[:,[10]]+Vi[:,[11]])**0.5
Vi[:,[3]] = mag4
```

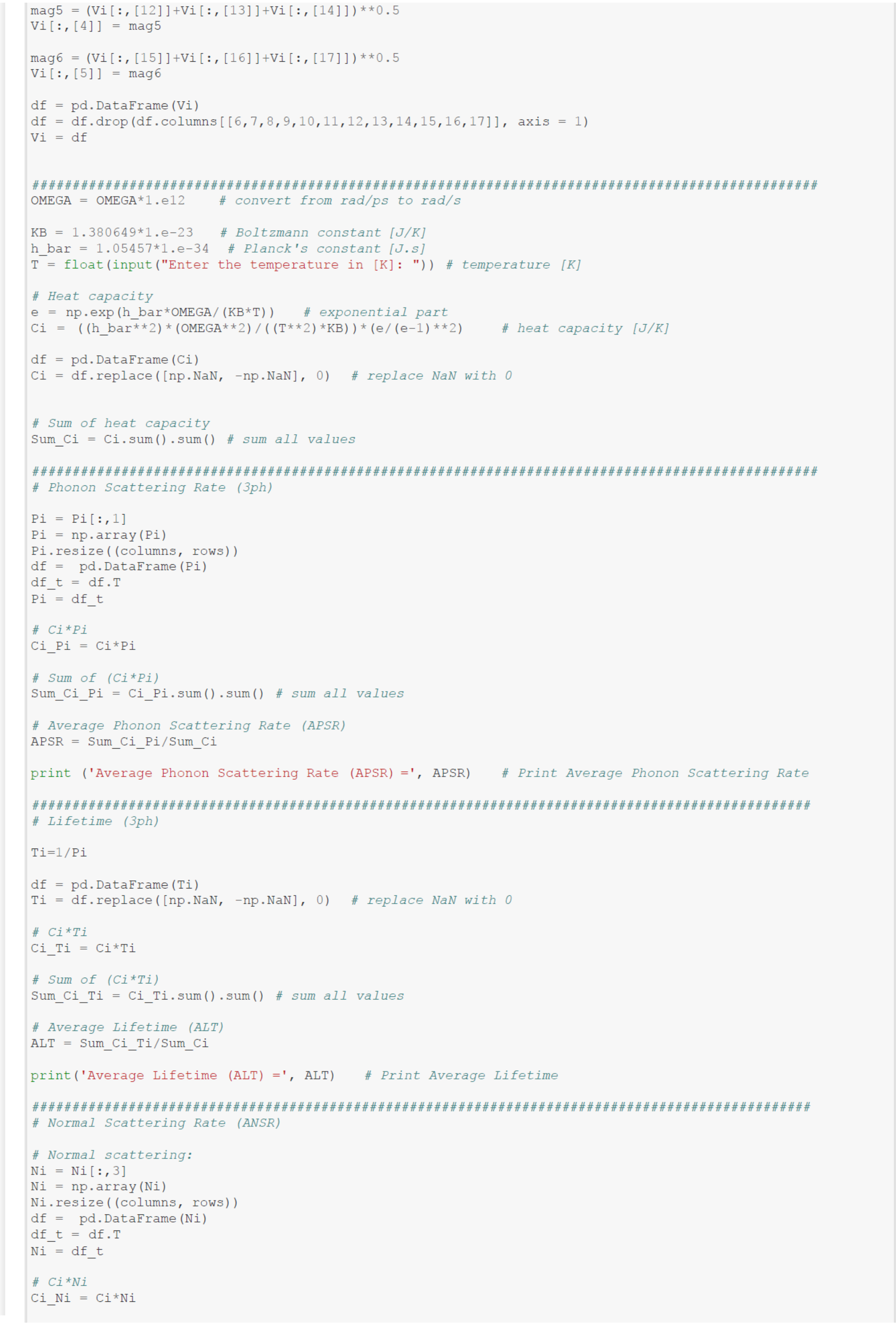

```
mag5 = (Vi[:,[12]]+Vi[:,[13]]+Vi[:,[14]])**0.5
Vi[:,[4]] = mag5

mag6 = (Vi[:,[15]]+Vi[:,[16]]+Vi[:,[17]])**0.5
Vi[:,[5]] = mag6

df = pd.DataFrame(Vi)
df = df.drop(df.columns[[6,7,8,9,10,11,12,13,14,15,16,17]], axis = 1)
Vi = df


###################################################################################################
OMEGA = OMEGA*1.e12    # convert from rad/ps to rad/s

KB = 1.380649*1.e-23   # Boltzmann constant [J/K]
h_bar = 1.05457*1.e-34  # Planck's constant [J.s]
T = float(input("Enter the temperature in [K]: ")) # temperature [K]

# Heat capacity
e = np.exp(h_bar*OMEGA/(KB*T))    # exponential part
Ci =  ((h_bar**2)*(OMEGA**2)/((T**2)*KB))*(e/(e-1)**2)     # heat capacity [J/K]

df = pd.DataFrame(Ci)
Ci = df.replace([np.NaN, -np.NaN], 0)  # replace NaN with 0


# Sum of heat capacity
Sum_Ci = Ci.sum().sum() # sum all values

###################################################################################################
# Phonon Scattering Rate (3ph)

Pi = Pi[:,1]
Pi = np.array(Pi)
Pi.resize((columns, rows))
df =  pd.DataFrame(Pi)
df_t = df.T
Pi = df_t

# Ci*Pi
Ci_Pi = Ci*Pi

# Sum of (Ci*Pi)
Sum_Ci_Pi = Ci_Pi.sum().sum() # sum all values

# Average Phonon Scattering Rate (APSR)
APSR = Sum_Ci_Pi/Sum_Ci

print ('Average Phonon Scattering Rate (APSR) =', APSR)    # Print Average Phonon Scattering Rate

##################################################################################################
# Lifetime (3ph)

Ti=1/Pi

df = pd.DataFrame(Ti)
Ti = df.replace([np.NaN, -np.NaN], 0)  # replace NaN with 0

# Ci*Ti
Ci_Ti = Ci*Ti

# Sum of (Ci*Ti)
Sum_Ci_Ti = Ci_Ti.sum().sum() # sum all values

# Average Lifetime (ALT)
ALT = Sum_Ci_Ti/Sum_Ci

print('Average Lifetime (ALT) =', ALT)    # Print Average Lifetime

##################################################################################################
# Normal Scattering Rate (ANSR)

# Normal scattering:
Ni = Ni[:,3]
Ni = np.array(Ni)
Ni.resize((columns, rows))
df =  pd.DataFrame(Ni)
df_t = df.T
Ni = df_t

# Ci*Ni
Ci_Ni = Ci*Ni
```

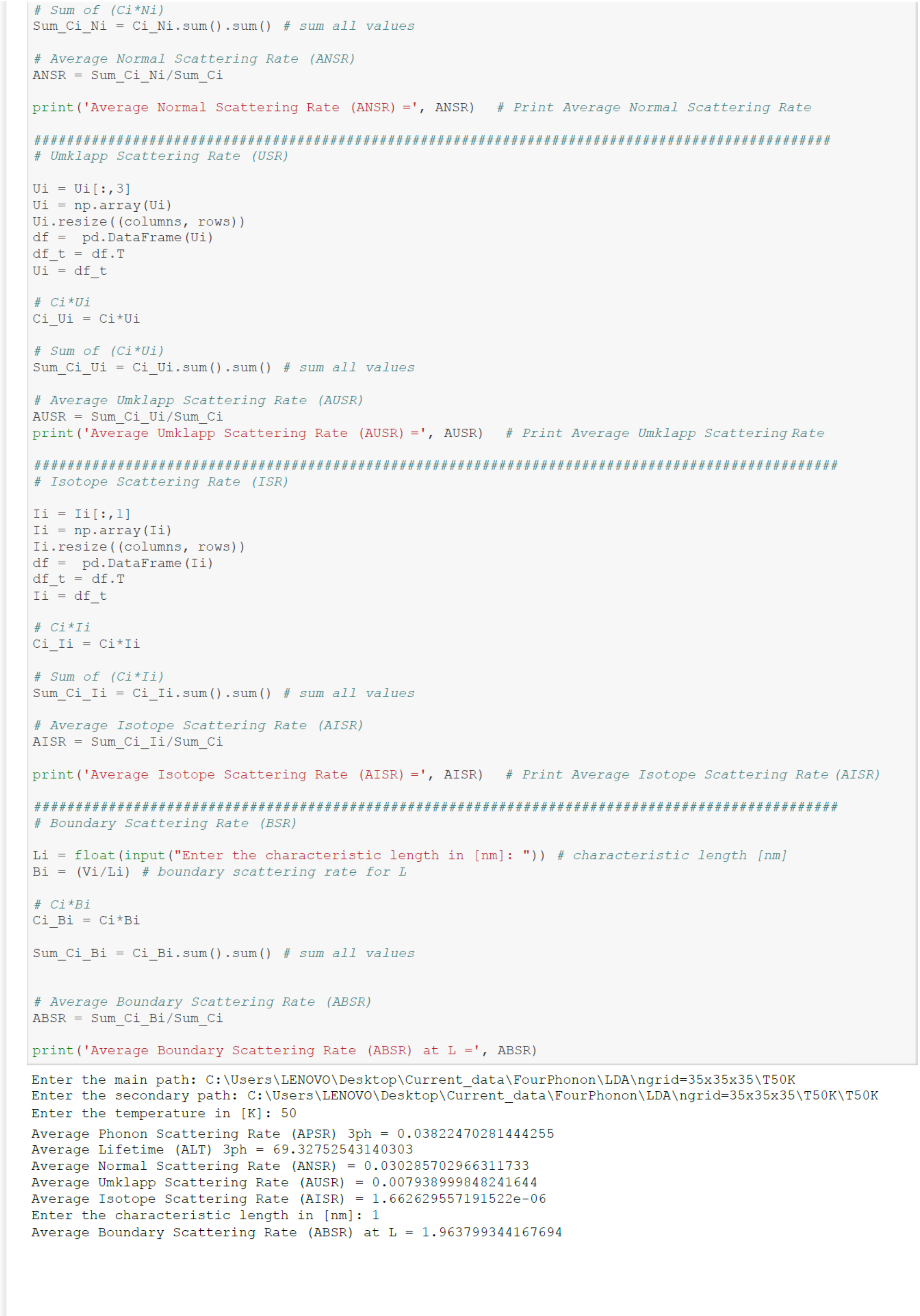

```python
# Sum of (Ci*Ni)
Sum_Ci_Ni = Ci_Ni.sum().sum() # sum all values

# Average Normal Scattering Rate (ANSR)
ANSR = Sum_Ci_Ni/Sum_Ci

print('Average Normal Scattering Rate (ANSR) =', ANSR)   # Print Average Normal Scattering Rate

##################################################################################################
# Umklapp Scattering Rate (USR)

Ui = Ui[:,3]
Ui = np.array(Ui)
Ui.resize((columns, rows))
df =  pd.DataFrame(Ui)
df_t = df.T
Ui = df_t

# Ci*Ui
Ci_Ui = Ci*Ui

# Sum of (Ci*Ui)
Sum_Ci_Ui = Ci_Ui.sum().sum() # sum all values

# Average Umklapp Scattering Rate (AUSR)
AUSR = Sum_Ci_Ui/Sum_Ci
print('Average Umklapp Scattering Rate (AUSR) =', AUSR)   # Print Average Umklapp Scattering Rate

###################################################################################################
# Isotope Scattering Rate (ISR)

Ii = Ii[:,1]
Ii = np.array(Ii)
Ii.resize((columns, rows))
df =  pd.DataFrame(Ii)
df_t = df.T
Ii = df_t

# Ci*Ii
Ci_Ii = Ci*Ii

# Sum of (Ci*Ii)
Sum_Ci_Ii = Ci_Ii.sum().sum() # sum all values

# Average Isotope Scattering Rate (AISR)
AISR = Sum_Ci_Ii/Sum_Ci

print('Average Isotope Scattering Rate (AISR) =', AISR)   # Print Average Isotope Scattering Rate (AISR)

###################################################################################################
# Boundary Scattering Rate (BSR)

Li = float(input("Enter the characteristic length in [nm]: ")) # characteristic length [nm]
Bi = (Vi/Li) # boundary scattering rate for L

# Ci*Bi
Ci_Bi = Ci*Bi

Sum_Ci_Bi = Ci_Bi.sum().sum() # sum all values


# Average Boundary Scattering Rate (ABSR)
ABSR = Sum_Ci_Bi/Sum_Ci

print('Average Boundary Scattering Rate (ABSR) at L =', ABSR)
```

```
Enter the main path: C:\Users\LENOVO\Desktop\Current_data\FourPhonon\LDA\ngrid=35x35x35\T50K
Enter the secondary path: C:\Users\LENOVO\Desktop\Current_data\FourPhonon\LDA\ngrid=35x35x35\T50K\T50K
Enter the temperature in [K]: 50
Average Phonon Scattering Rate (APSR) 3ph = 0.03822470281444255
Average Lifetime (ALT) 3ph = 69.32752543140303
Average Normal Scattering Rate (ANSR) = 0.030285702966311733
Average Umklapp Scattering Rate (AUSR) = 0.007938999848241644
Average Isotope Scattering Rate (AISR) = 1.662629557191522e-06
Enter the characteristic length in [nm]: 1
Average Boundary Scattering Rate (ABSR) at L = 1.963799344167694
```

b) Average phonon scattering rates for multiple temperatures

1) Comprehensive folder path is the path that includes both main folders and secondary folders for different temperatures.

2) Main folder must be named in the same way as the secondary folder (i.e, main folder name: T70K, secondary folder name: T70K).

3) The characteristic length is by default = 500 nm; it can be changed from the same code.

4) Temperature range is set up to 2000 K; it can be changed from the same code.

```
from numpy import array, concatenate , atleast_1d
import numpy as np
import pandas  as pd
from pathlib import Path
import os
from pylab import *
import pickle
import sys
import itertools
from colorama import init
from termcolor import cprint
from pyfiglet import figlet_format
from PIL import Image, ImageFont, ImageDraw


##################################################################################################
# main folder
datadir =  input("Enter the comprehensive folder path: ")
results = []
##################################################################################################

for i in range(1,2000):
    # load the data
    files_1 = Path(datadir+'\T'+str(i)+'K')
    files_2 = Path(datadir+'\T'+str(i)+'K'+'\T'+str(i)+'K')

    if os.path.exists(files_1):
        a_0 = i
        a_0 = np.array([a_0])

        files_1= str(Path(files_1))
        files_2= str(Path(files_2))

        ##################################################################################################
        # Required files:
        OMEGA = np.loadtxt(files_1+'\BTE.omega')    # angular frequency [rad/ps]
        Pi = np.loadtxt(files_2+'\BTE.w_3ph')  # phonon scattering rate [1/ps]
        Ni = np.loadtxt(files_2+'\BTE.w_3ph_normal')    # normal scattering rate [1/ps]
        Ui = np.loadtxt(files_2+'\BTE.w_3ph_Umklapp')   # umklapp scattering rate [1/ps]
        Ii = np.loadtxt(files_1+'\BTE.w_isotopic')    # isotope scattering rate [1/ps]
        Vi = np.loadtxt(files_1+'\BTE.v')   # group velocity [km/s]

        ##################################################################################################
        rows = len(OMEGA)          # number of rows [OMEGA]
        columns = len(OMEGA[0])    # number of columns [OMEGA]

        # Group velocity:
        Vi_0 = Vi[:,0]
        Vi_0 = np.array(Vi_0)
        Vi_0.resize((columns, rows))
        df = pd.DataFrame(Vi_0)
        df_t = df.T
        Vi_0 = df_t

        Vi_1 = Vi[:,1]
        Vi_1 = np.array(Vi_1)
        Vi_1.resize((columns, rows))
        df = pd.DataFrame(Vi_1)
        df_t = df.T
        Vi_1 = df_t

        Vi_2 = Vi[:,2]
        Vi_2 = np.array(Vi_2)
```

```
        Vi_2.resize((columns, rows))
        df = pd.DataFrame(Vi_2)
        df_t = df.T
        Vi_2 = df_t

        Vi = np.concatenate((Vi_0, Vi_1, Vi_2), axis=1)

        Vi = Vi**2

        mag1 = (Vi[:,[0]]+Vi[:,[1]]+Vi[:,[2]])**0.5
        Vi[:,[0]] = mag1

        mag2 = (Vi[:,[3]]+Vi[:,[4]]+Vi[:,[5]])**0.5
        Vi[:,[1]] = mag2

        mag3 = (Vi[:,[6]]+Vi[:,[7]]+Vi[:,[8]])**0.5
        Vi[:,[2]] = mag3

        mag4 = (Vi[:,[9]]+Vi[:,[10]]+Vi[:,[11]])**0.5
        Vi[:,[3]] = mag4

        mag5 = (Vi[:,[12]]+Vi[:,[13]]+Vi[:,[14]])**0.5
        Vi[:,[4]] = mag5

        mag6 = (Vi[:,[15]]+Vi[:,[16]]+Vi[:,[17]])**0.5
        Vi[:,[5]] = mag6

        df = pd.DataFrame(Vi)
        df = df.drop(df.columns[[6,7,8,9,10,11,12,13,14,15,16,17]], axis = 1)
        Vi = df

        #################################################################################################
        OMEGA = OMEGA*1.e12    # convert from rad/ps to rad/s

        KB  = 1.380649*1.e-23 # Boltzmann  constant  [J/K]
        h_bar = 1.05457*1.e-34 # Planck's constant  [J.s]
        T = int(i) # temperature  [K]

        # Heat capacity
        e = np.exp(h_bar*OMEGA/(KB*T))    # exponential part
        Ci  =  ((h_bar**2)*(OMEGA**2)/((T**2)*KB))*(e/(e-1)**2)     # heat capacity [J/K]

        df = pd.DataFrame(Ci)
        Ci = df.replace([np.NaN, -np.NaN], 0)   # replace NaN with 0


        # Sum of heat capacity
        Sum_Ci = Ci.sum().sum() # sum all values

        #################################################################################################
        # Phonon Scattering Rate (3ph)

        Pi = Pi[:,1]
        Pi = np.array(Pi)
        Pi.resize((columns, rows))
        df = pd.DataFrame(Pi)
        df_t = df.T
        Pi = df_t

        # Ci*Pi
        Ci_Pi = Ci*Pi

        # Sum of (Ci*Pi)
        Sum_Ci_Pi = Ci_Pi.sum().sum() # sum all values

        # Average Phonon Scattering Rate (APSR)
        APSR = Sum_Ci_Pi/Sum_Ci

        a_1 = APSR
        a_1 = np.array([a_1])


        #################################################################################################
        # Lifetime (3ph)

        Ti=1/Pi

        df = pd.DataFrame(Ti)
        Ti = df.replace([np.NaN, -np.NaN], 0)   # replace NaN with 0

        # Ci*Ti
        Ci_Ti = Ci*Ti
```

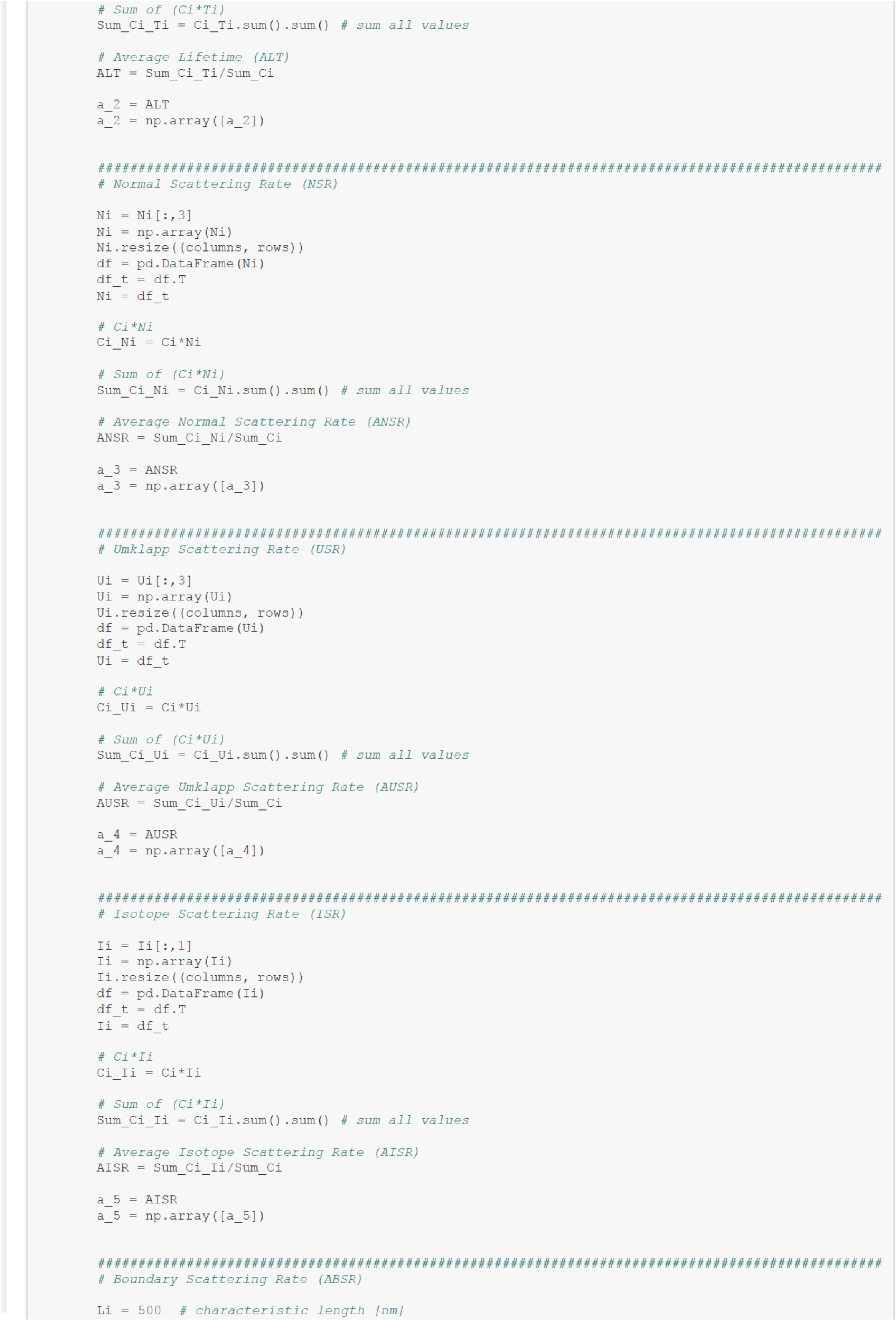

```
        # Sum of (Ci*Ti)
        Sum_Ci_Ti = Ci_Ti.sum().sum() # sum all values

        # Average Lifetime (ALT)
        ALT = Sum_Ci_Ti/Sum_Ci

        a_2 = ALT
        a_2 = np.array([a_2])


        #################################################################################################
        # Normal Scattering Rate (NSR)

        Ni = Ni[:,3]
        Ni = np.array(Ni)
        Ni.resize((columns, rows))
        df = pd.DataFrame(Ni)
        df_t = df.T
        Ni = df_t

        # Ci*Ni
        Ci_Ni = Ci*Ni

        # Sum of (Ci*Ni)
        Sum_Ci_Ni = Ci_Ni.sum().sum() # sum all values

        # Average Normal Scattering Rate (ANSR)
        ANSR = Sum_Ci_Ni/Sum_Ci

        a_3 = ANSR
        a_3 = np.array([a_3])


        #################################################################################################
        # Umklapp Scattering Rate (USR)

        Ui = Ui[:,3]
        Ui = np.array(Ui)
        Ui.resize((columns, rows))
        df = pd.DataFrame(Ui)
        df_t = df.T
        Ui = df_t

        # Ci*Ui
        Ci_Ui = Ci*Ui

        # Sum of (Ci*Ui)
        Sum_Ci_Ui = Ci_Ui.sum().sum() # sum all values

        # Average Umklapp Scattering Rate (AUSR)
        AUSR = Sum_Ci_Ui/Sum_Ci

        a_4 = AUSR
        a_4 = np.array([a_4])


        #################################################################################################
        # Isotope Scattering Rate (ISR)

        Ii = Ii[:,1]
        Ii = np.array(Ii)
        Ii.resize((columns, rows))
        df = pd.DataFrame(Ii)
        df_t = df.T
        Ii = df_t

        # Ci*Ii
        Ci_Ii = Ci*Ii

        # Sum of (Ci*Ii)
        Sum_Ci_Ii = Ci_Ii.sum().sum() # sum all values

        # Average Isotope Scattering Rate (AISR)
        AISR = Sum_Ci_Ii/Sum_Ci

        a_5 = AISR
        a_5 = np.array([a_5])


        #################################################################################################
        # Boundary Scattering Rate (ABSR)

        Li = 500  # characteristic length [nm]
```

```
        Bi = (Vi/Li) # boundary scattering rate

        # Ci*Bi
        Ci_Bi = Ci*Bi

        Sum_Ci_Bi = Ci_Bi.sum().sum() # sum all values


        # Average Boundary Scattering Rate (ABSR)
        ABSR = Sum_Ci_Bi/Sum_Ci

        a_6 = ABSR
        a_6 = np.array([a_6])

        ###################################################################################################
        file = []
        df = pd.DataFrame(file)
        file = [a_0, a_1, a_2, a_3, a_4, a_5, a_6]
        file = np.array(file)
        file = concatenate([atleast_1d(a) for a in [file]])
        df = pd.DataFrame(file)
        file = df
        rows_2 = len(file)
        columns_2 = len(file[0])
        file = np.array(file)
        file.resize((1, rows_2))
        df = pd.DataFrame(file)
        file =np.array(file)
        results.append(file)

    else:
        i=i

results=np.concatenate((results))
df = pd.DataFrame(results)
results = df
df.columns =['T(K)', 'APSR_3p (1/ps)', 'ALT_3p (ps)', 'ANSR (1/ps)','AUSR(1/ps) ',  'AISR (1/ps)', 'ABSR
(1/ps)']
df.to_excel(input("Enter the path where you would like to save the results in an excel file")+'/results_5
00nm.xlsx')

ShowText = 'DONE!'

font = ImageFont.truetype('arialbd.ttf', 15)
size = font.getsize(ShowText)
image = Image.new('1', size, 1)
draw = ImageDraw.Draw(image)
draw.text((0, 0), ShowText, font=font)
for rownum in range(size[1]):
    line = []
    for colnum in range(size[0]):
        if image.getpixel((colnum, rownum)): line.append(' '),
        else: line.append('#'),
    print (''.join(line))
```

```
Enter the comprehensive folder path: C:\Users\LENOVO\Desktop\LiF_2\LiF\LiF\LiH\third\new\AB-bilayer\AB\Fou
rPhonon_8x8x1\FourPhonon_4x4x1 -5\isotopes=.true\ngrid=150 150 1
Enter the path where you would like to save the results in an excel fileC:\Users\LENOVO\Desktop\LiF_2\LiF\
LiF\LiH\third\new\AB-bilayer\AB\FourPhonon_8x8x1\FourPhonon_4x4x1 -5\isotopes=.true\ngrid=150 150 1



 ######        ####     ##     ##  ########  ##
 ########    ########   ###    ##  ########  ##
 ##    ##    ##    ##   ####   ##  ##        ##
 ##     ##  ##      ##  ####   ##  ##        ##
 ##     ##  ##      ##  ## ##  ##  ########  ##
 ##     ##  ##      ##  ## ##  ##  ########  ##
 ##     ##  ##      ##  ##  ## ##  ##        ##
 ##     ##  ##      ##  ##   ####  ##        ##
 ##    ##    ##    ##   ##   ####  ##
 ########    ########   ##    ###  ########  ##
 ######        ####     ##     ##  ########  ##
```

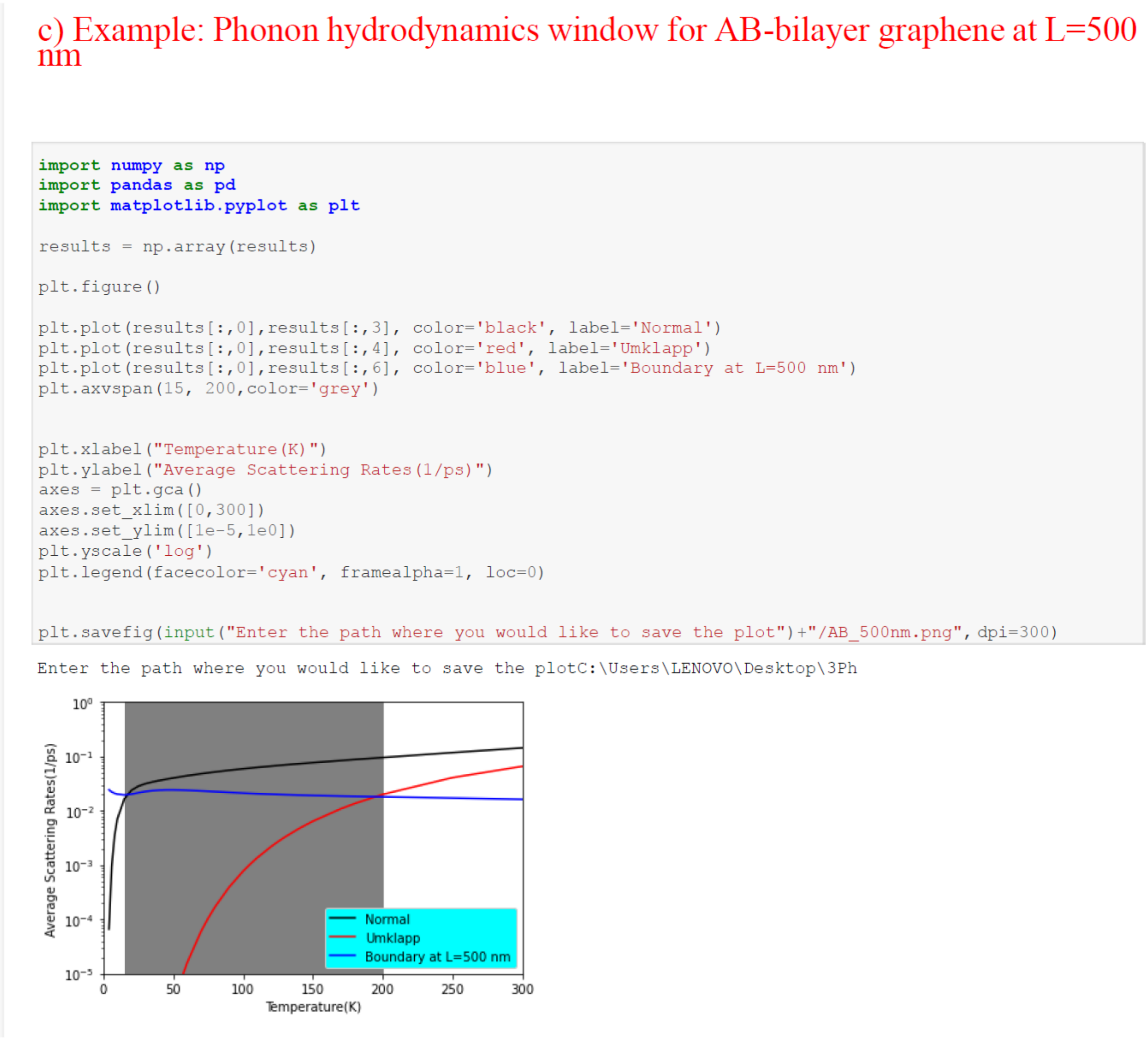

c) Example: Phonon hydrodynamics window for AB-bilayer graphene at L=500 nm

```
import numpy as np
import pandas as pd
import matplotlib.pyplot as plt

results = np.array(results)

plt.figure()

plt.plot(results[:,0],results[:,3], color='black', label='Normal')
plt.plot(results[:,0],results[:,4], color='red', label='Umklapp')
plt.plot(results[:,0],results[:,6], color='blue', label='Boundary at L=500 nm')
plt.axvspan(15, 200,color='grey')


plt.xlabel("Temperature(K)")
plt.ylabel("Average Scattering Rates(1/ps)")
axes = plt.gca()
axes.set_xlim([0,300])
axes.set_ylim([1e-5,1e0])
plt.yscale('log')
plt.legend(facecolor='cyan', framealpha=1, loc=0)


plt.savefig(input("Enter the path where you would like to save the plot")+"/AB_500nm.png", dpi=300)
```

```
Enter the path where you would like to save the plotC:\Users\LENOVO\Desktop\3Ph
```